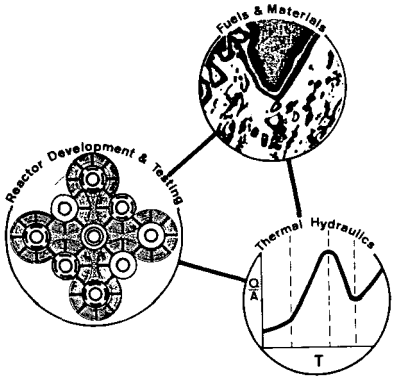

IN-1335
Issued: November 1969
Metals, Ceramics, and Materials
TID-4500

REACTOR ENGINEERING BRANCH ANNUAL REPORT FISCAL YEAR 1969

D. R. deBoisblanc

MANAGER

NUCLEAR AND CHEMICAL TECHNOLOGY DIVISION

W. C. Francis

MANAGER

REACTOR ENGINEERING

E. D. Covington

EDITOR

IDAHO NUCLEAR CORPORATION
A Jointly Owned Subsidiary of
AEROJET GENERAL CORPORATION
ALLIED CHEMICAL CORPORATION
PHILLIPS PETROLEUM COMPANY

U. S. Atomic Energy Commission Research and Development Report
Issued Under Contract AT(10-1)-1230
Idaho Operations Office

DISCLAIMER

INTRODUCTION

This represents the second annual report compiled by the Reactor Engineering Branch; the previous report being IN-1228.

The Reactor Engineering Branch represents one of the technical organizations of the Nuclear and Chemical Technology Division of the Idaho Nuclear Corporation. Branch personnel perform development work in the areas of materials science, nuclear fuels, and engineering. It operates two low power critical facilities in support of the test reactors, two reactivity measurement facilities for physics research, and conducts a school for training engineering and science graduates in test reactor operation.

In addition, the Fuel Project Engineering office was established in May 1968, as a part of the Branch to provide technical support to fuel procurement activities.

Highlights of the FY-1969 activities of the six groups comprising the Branch are presented in the following pages. The Branch organization as it existed at the end of FY-1969 is shown at the end of the report.

SUMMARY

I. MATERIALS RESEARCH

An investigation was concluded to determine the influence of hydrogen on the ductile and static load properties of several irradiated intermediate strength low alloy steels. The degree to which these properties were affected was generally found to be dependent on strength level. Increasing the strength level as a result of heat treatment, cold work, or irradiation increased the extent to which those parameters were reduced per given hydrogen content.

Physical property changes due to irradiation of beryllium are continuing to be monitored through the ATR Materials Surveillance Program. Hafnium has been added to the program to monitor changes of the ATR absorber sections.

Over 400 hourglass-shaped specimens of cladding and pressure vessel materials have been or are presently being irradiated for postirradiation elevated temperature fatigue testing. Specimens of type 304 stainless steel which were irradiated in argon at 750°C have been push-pull fatigue tested at 500°C in an argon environment. Within the scatter of the data, little difference is noted between fatigue properties of the irradiated 304 stainless and the unirradiated material.

II. FUELS DEVELOPMENT

The destructive examination of five ETR boron-foil fuel elements indicates that this type of fuel element can safely be used in low and medium power positions (less than 2.0% of reactor power) of the ETR. Testing is continuing in high power positions.

Three full-sized 2219 aluminum alloy clad fuel elements have been successfully tested in the Engineering Test Reactor.

Progress on sample plate irradiations in the G-12 pressurized water loop of the ETR, capsule irradiations in the MTR and ETR, and postirradiation examinations are discussed.

Irradiation testing of sample fuel plates fabricated by experimental rolling procedures has shown it is possible to produce plates containing semibonded regions which will pass nondestructive testing, but which do not have the required bond integrity for reactor use. This suggests that it is necessary to qualify fabrication procedures by destructive as well as nondestructive means, and that the reliability of the fuel plates depends on the fabricator's ability to repeat qualification procedures consistently.

The good blister resistance of the uranium aluminides, whether dispersed in aluminum or stainless steel, is attributed to the good fission gas retention capability of this material and the almost negligible tendency for gas bubble agglomeration in the UAl_3.

Blister mechanism observations of UAl_x-Al dispersions show that the aluminum matrix reaches its limit to retain fission recoil gas before any indication of gas retention problems appear in the UAl_x.

Pure UAl_3 has shown gas retention capabilities up to 1250°C or just below the melting point. Under similar irradiation conditions (heat generation rate and surface temperature), the fission gas retention in UAl_3 is considerably better than UO_2.

Gamma scanning of prototype reactor fuel plates in which Co-60 tagged boron glass was incorporated indicates that this is a satisfactory means of assaying for boron and that the gamma activity from the Co-60 does not interfere with the assay for U-235. Improved procedures were developed for the preparation of the Co-60 tagged boron glass to ensure that the Co-60 - boron ratio is uniform throughout the glass and that the proper particle sizes of glass powder can be prepared.

A prototype radiograph densitometer was constructed to measure fuel density on sample fuel plate radiographs and a computer program was written to treat the output data. Radiograph standards were designed to calibrate the system according to present ATR fuel loading specifications.

The postirradiation examination of 55 wt% UAl alloy powder fuel cores shows that these core types compare favorably with UAl_x + Al fuel dispersions from both a swelling and a blister standpoint and may offer an acceptable fabrication procedure.

Zircaloy-2 alloy exposed to emergency core cooling conditions becomes embrittled as a result of an oxygen saturated α phase layer which forms on the surface.

A comparison of the compressive yield strengths of irradiated and unirradiated standard ETR fuel plates at various temperatures has been made. Preliminary results show that the ETR composition fuel plates have a loss in strength at the end of a normal operating cycle.

III. ENGINEERING EXPERIMENTS

Limiting heat transfer capability in natural convection and in emergency and operational flow regimes has been determined in the ATR startup program by means of specially designed and instrumented experimental fuel elements.

Hydraulic tests on ATR fuel elements to determine the cause of observed flow reduction in Channel 20 have resulted in modifications to the venting arrangement in the fuel element side plates.

IV. CRITICAL FACILITIES

A Coupled Fast Reactivity Measurement Facility has been installed in ARMF-II for measurement of fast neutron integral cross sections.

Fission rate studies in ATRC have shown good correlation between experiment fluxes and lobe power.

A new set of weighting factors has been obtained in ATRC to aid in calculations of power generated in fuel elements.

Significant progress is reported toward flux stabilization in ETR.

V. REACTOR TRAINING

A Reactor Simulation Laboratory was constructed during the year and the ATR simulator transferred to the new building. By the end of the fiscal year, the ETR simulator was 90% completed and the MTR simulator 75% completed.

VI. FUEL PROJECT ENGINEERING OFFICE

During the year, technical assistance was provided in the administration of fuel procurement for the test reactors operated by Idaho Nuclear Corporation. This assistance has been concentrated in the areas of fuel specification preparation and development and liaison with commercial vendors supplying test reactor fuel elements.

CONTENTS

FIGURES

TABLES

1. EFFECTS OF IRRADIATION ON THE SUSCEPTIBILITY TO HYDROGEN EMBRITTLEMENT OF PRESSURE VESSEL STEELS

(C. R. Brinkman, J. M. Beeston)

The presence of hydrogen in other than austenitic steels can lead to several deleterious effects. These include blistering as a result of methane formation, loss of strength and ductility, cracking and time-dependent failure at stress levels less than yield. Blistering subsequent to methane formation in a reactor vessel steel is not considered to be a problem because of the high hydrogen pressures and temperatures required. Loss of ductility, strength, and delayed failure at hydrogen concentrations likely to arise from water-vessel reactions [up to 2 ppm (wt)] also seem unlikely due to the inherent toughness and ductility of vessel steels presently in use or under consideration. However, irradiation decreases the ductility of these steels and the question arose whether several of the intermediate strength vessel steels in the irradiated condition would be subject to appreciable loss of strength, ductility, or possible delayed (time dependent) failure due to the presence of small amounts of hydrogen. An appreciable loss of ductility in the irradiated material as a result of the presence of hydrogen would be undesirable from a design point of view; ductility serves to reduce stress concentrations resulting from design or flaw discontinuities. Therefore, adequate ductility, usually considered to be roughly 10 to 15% as measured on a two-inch gage-length specimen, is considered to be a desirable, if not a required, characteristic of the steel.

To ascertain the influence of hydrogen on these steels in the irradiated condition two simple tests are accepted. First, low strain rate tensile tests were used to determine ductility and strength changes as a function of hydrogen content. Second, stress-rupture or constant load tests were employed to determine the extent of any delayed failure possible at several hydrogen concentrations. Accoustic emission measurements were also made where extensive amounts of delayed failure occurred. The results of this experimentation is reported in the following sections.

1.1 Tensile Testing of Irradiated Hydrogen Charged Steels

Tensile tests have been completed using unnotched and hydrogenated (1 to 9 ppm by weight) specimens that had been irradiated to three fluence levels, ranging from approximately 7×10^{18} to 4×10^{20} n/cm^2 E > 1 MeV. Whereas the normal quenched and tempered condition was used for most of the tests, some specimens were included that had been machined from blanks heat-treated to different strength levels or cold-worked various amounts by rolling. Results from these experiments show that the ductility and true fracture stress decrease with increasing hydrogen content. The degree to which these properties were reduced was generally found to be dependent on strength level with microstructure and material chemistry of secondary importance. Increasing the strength level as a result of heat treatment, cold working, or irradiation increased the extent to which these parameters were reduced per given hydrogen content. Figures I-1 through -4 are plots of true fracture strength

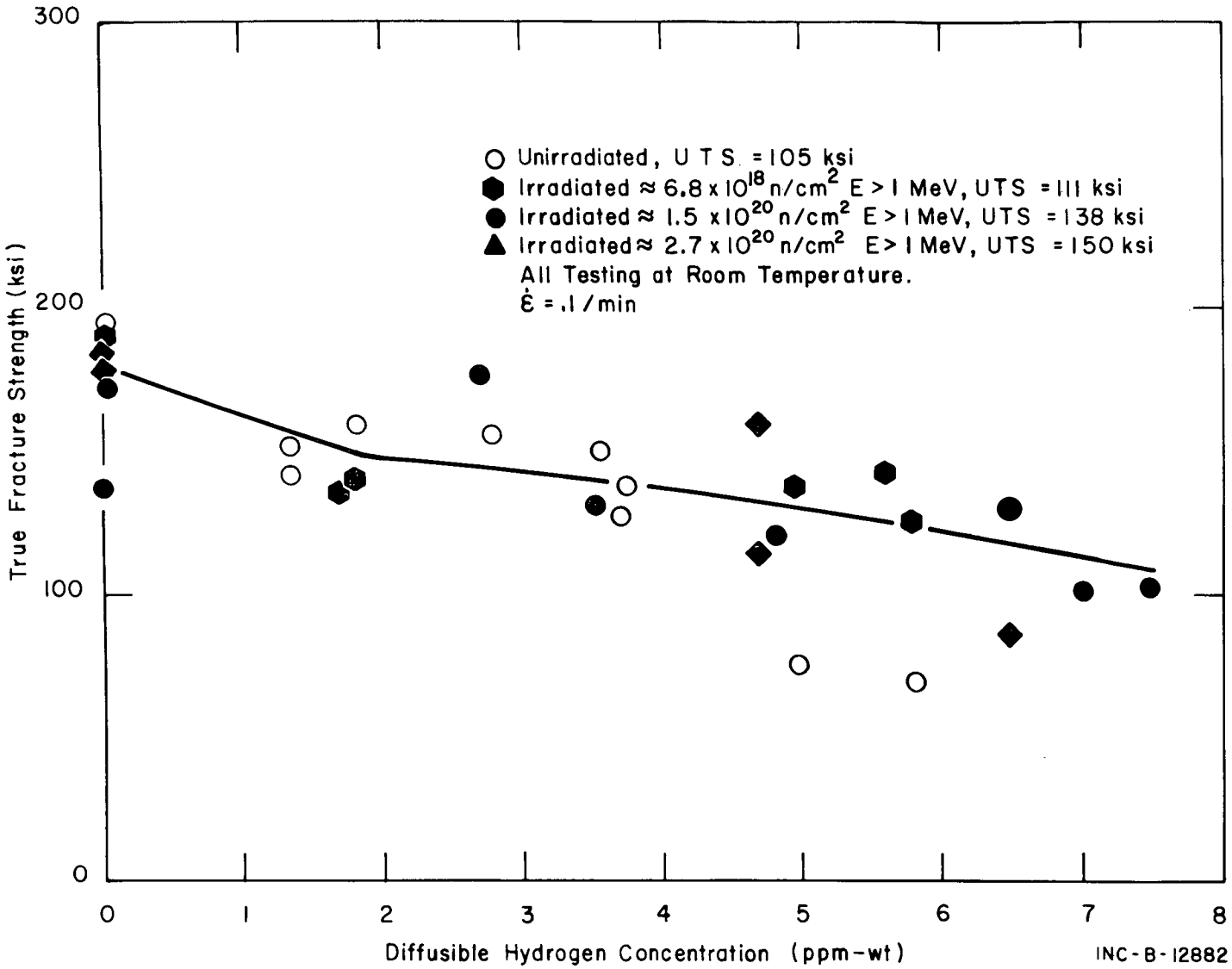

Fig. I-1 True fracture strength as a function of hydrogen content for A302B steel irradiated to several fluences.

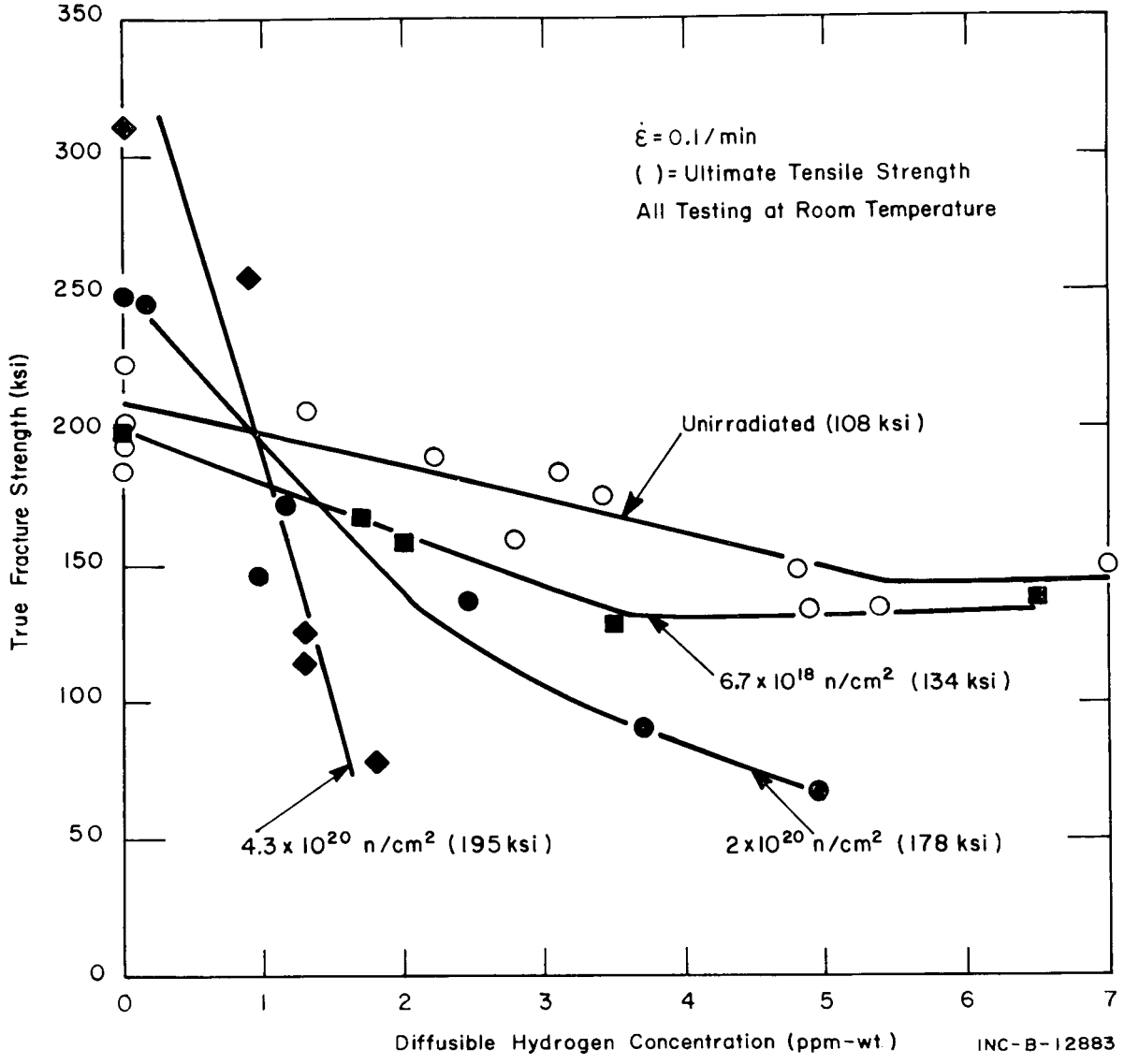

Fig. I-2 True fracture strength as a function of hydrogen content for HY-80 steel irradiated to several fluences (E > 1 MeV).

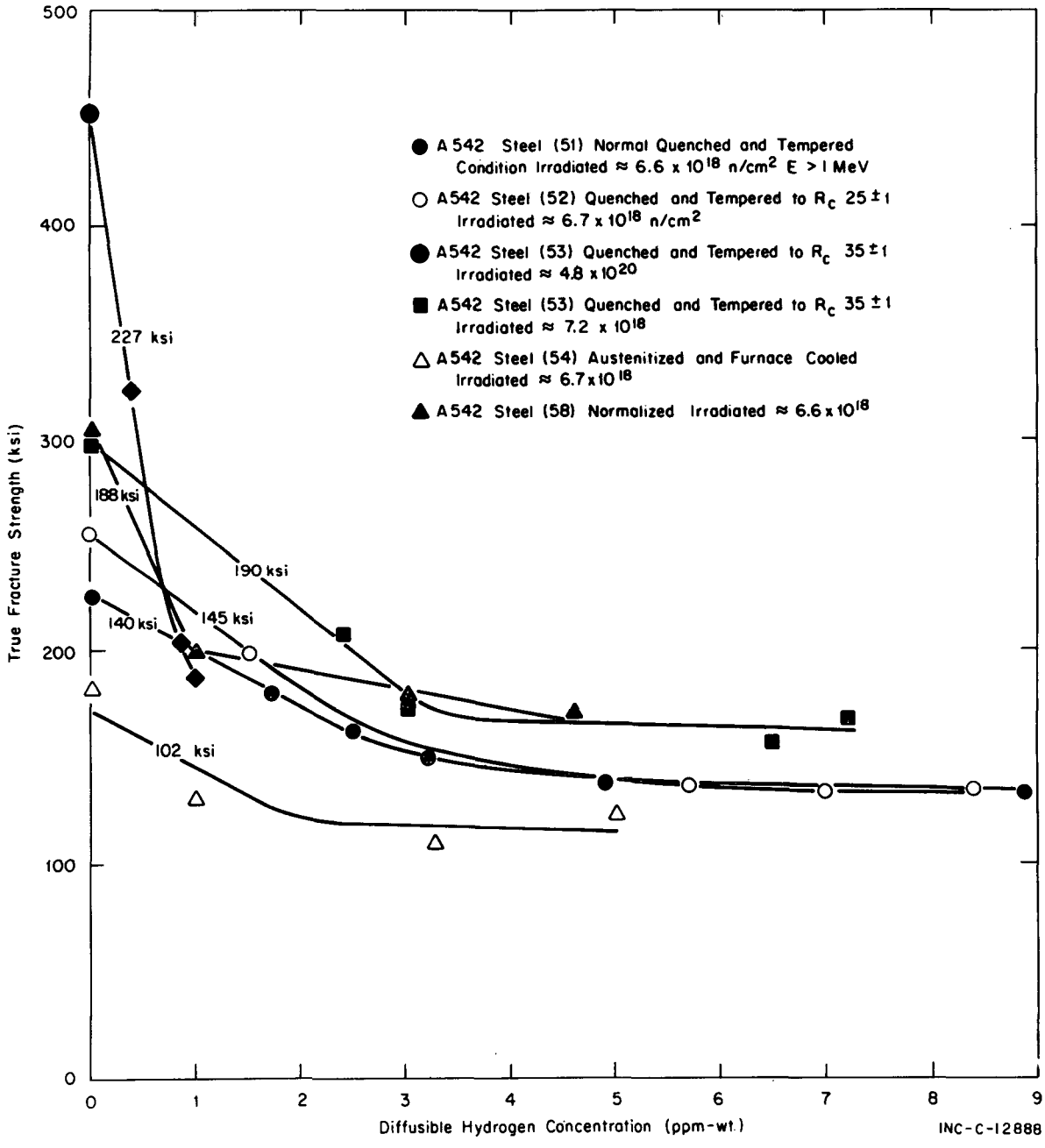

Fig. I-3 True fracture strength as a function of diffusible hydrogen concentration for A542 steel heat-treated to various strength levels and irradiated to several fluences.

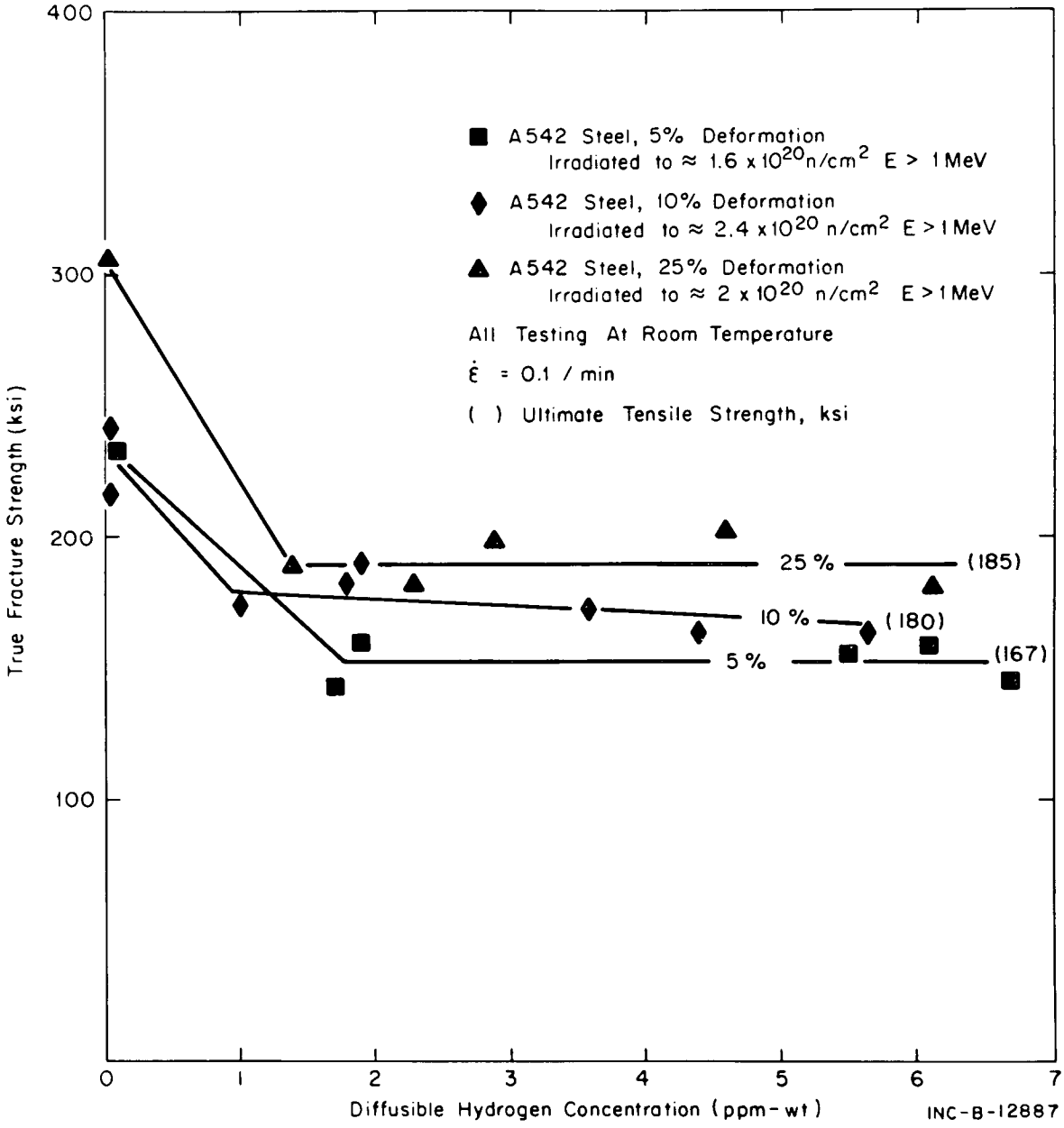

Fig. I-4 True fracture strength as a function of hydrogen content for A542 steel that had been cold-rolled prior to irradiation.

as a function of hydrogen content for the three steels under consideration. To a first approximation these figures exhibit a linear decrease in fracture strength with increasing hydrogen content up to approximately 2 ppm (wt). Figure I-1 shows that the fracture strength of A302B steel is reduced slightly with hydrogen content. However, over the strength level considered (105 to 150 ksi) within the scatter of the data, the amount of reduction is nearly insensitive to irradiation-induced increases in strength level up to concentrations of 3 to 4 ppm. The fracture strength of HY-80 steel, Figure I-2, however, is more adversely affected by the presence of hydrogen as indicated by slope increases, ie, negative slope ($-d\sigma_f/dH_2$) with increasing stress level. It appears this difference is due to the initial strength differences and to irradiation-induced hardening of HY-80. Figure I-3 illustrates the changes in fracture strength due to the presence of hydrogen in irradiated A542 steel heat-treated to various strength levels. Again, it is evident that changes in fracture strength with hydrogen content ($-d\sigma_f/dH_2$) over the concentration range 0 to 2 ppm by weight are responsive to strength level, increasing slightly over the range 102 to 190 ksi. In Figure I-4 the fracture strength data are plotted for cold-worked (5 to 25%) and irradiated A542 steel. Again, there is an initial rapid decrease in the true fracture strength, the slope of the curves depending upon the strength level.

Plots of negative slope $-d\sigma f/dH_2$ of these curves as a function of ultimate and fracture strength are shown in Figures I-5 and -6, respectively. The utility of these curves lies in the fact that although there is considerable inherent scatter in the data, the ultimate and fracture stress regions at which hydrogen-induced ductile-to-brittle transition occurs are defined for these low alloy steels at concentrations $\leq$ 2 ppm (wt).

It is the current belief of many workers in the field that the principal source of diffusible hydrogen in a pressurized water reactor pressure vessel in service will be from water-vessel corrosion reactions. The maximum concentration is expected to be from 1 to 2 ppm. Further, a peak fluence of 3×10^{19} for the vessel wall is anticipated. From Figure I-5, the conclusions to be drawn from these tensile tests are the following:

(1) The ductility of A302B after irradiation to 3×10^{19} n/cm^2 E >1 MeV will not be significantly affected by the presence of hydrogen, ie, concentrations of less than or equal to 2 ppm (wt). Further, irradiation to as high a fluence as 2.7×10^{20} would not harden this steel to the point where marked changes in the ductility could result upon introduction of hydrogen to this concentration level.

(2) HY-80 and A542 steel in the normal quenched and tempered condition would be sufficiently hardened by irradiation to a fluence of 3×10^{19} to put their strength levels in the knee or transition region of the curve. Any additional hardening as a result of plastic deformation, heat treatment, or irradiation could lead to a condition where brittle fracture would be possible.

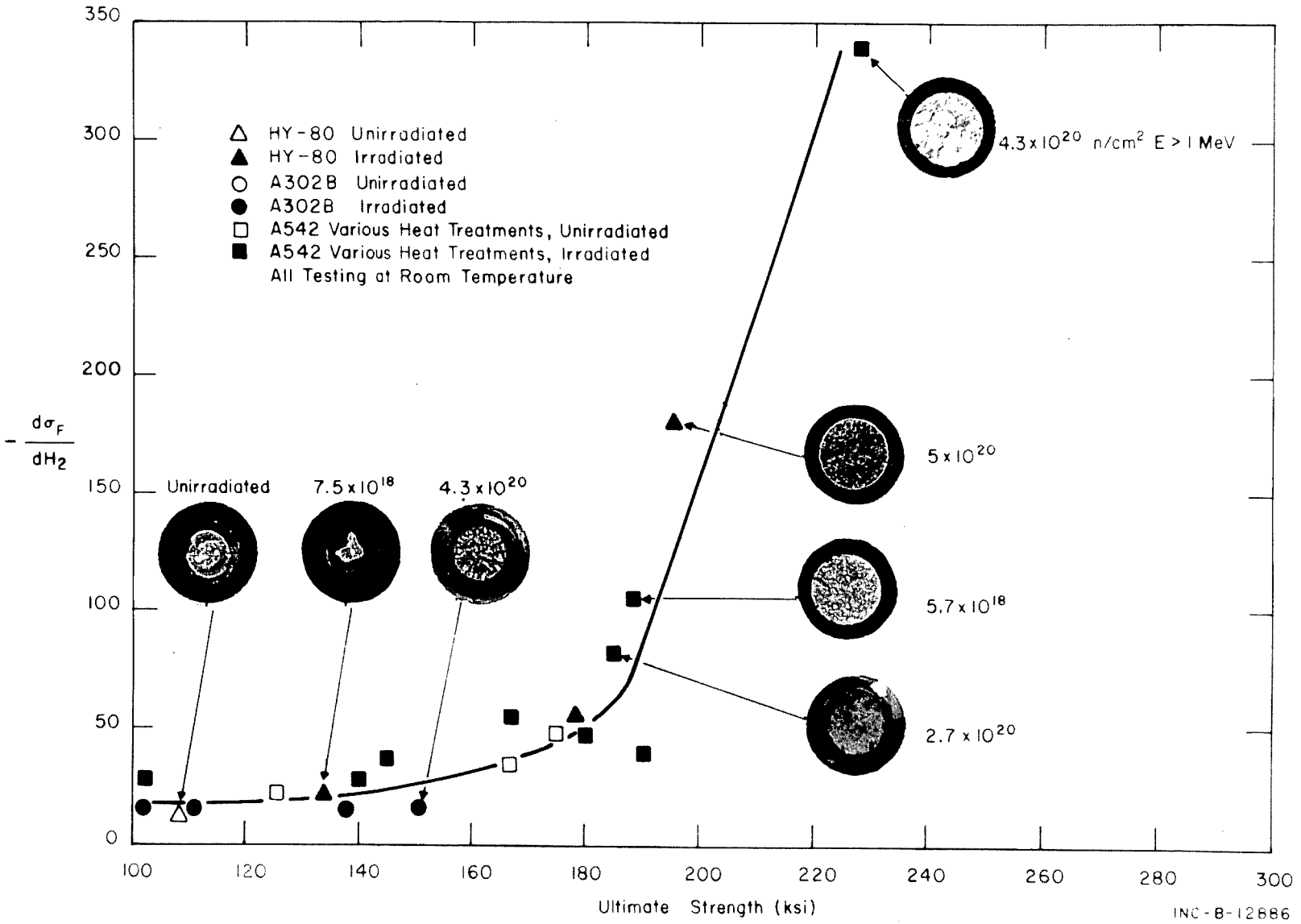

Fig. I-5 Susceptibility to hydrogen embrittlement as a function of ultimate strength for A302B, HY-80, and A542 steel containing diffusible hydrogen concentrations $\leq$ 2 ppm (wt).

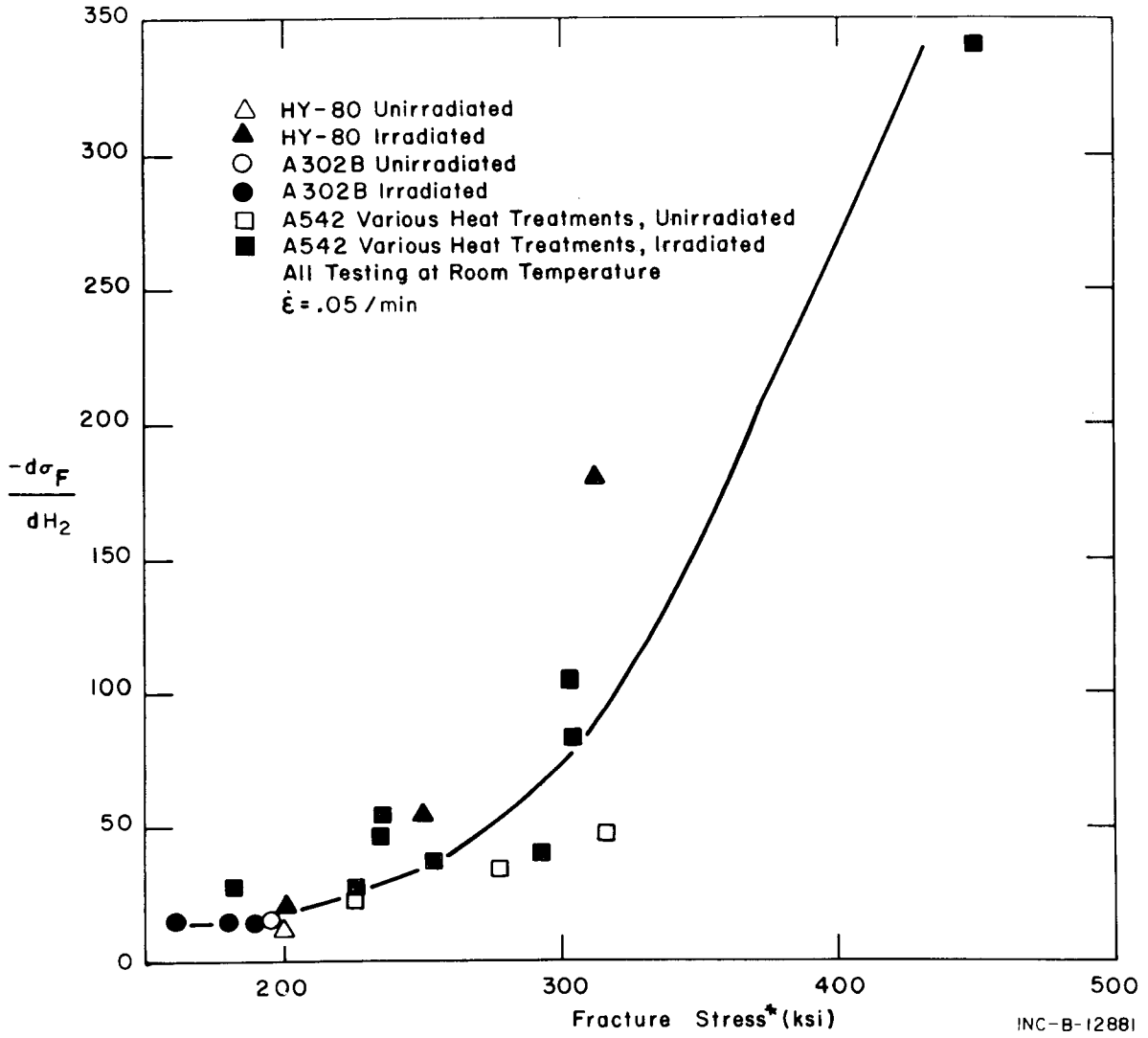

Fig. 1-6 Susceptibility to hydrogen embrittlement as a function of uncharged fracture stress for A302B, HY-80, and A542 steel containing diffusible hydrogen concentrations $\leq$ 2 ppm (wt).

* Fracture stress is the load at failure divided by cross-sectional area at failure.

1.2 Stress Rupture Testing of Irradiated Hydrogen Charged Steels

Specimens were prepared containing a 60-degree notch with a notch sharpness greater than 50 and a notch depth of 0.5 (ie, $1-d^2/D^2$) and irradiated to the fluences reported in the previous section. In Figure I-7 are plotted the results of stress rupture tests conducted on hydrogenated HY-80 steel that had been irradiated to fluence in excess of 10^{20} n/cm^2 E > 1 MeV. These curves are typical of the data recorded for all of the steels tested in the normal quenched and tempered condition. Results from these tests support several conclusions:

(1) Hydrogen-induced delayed failure does not occur to any large extent in the three steels investigated even after irradiating to fluences in excess of 10^{20} n/cm^2 and charging to a concentration level of up to 4 ppm.

(2) Irradiation hardening increased the magnitude of the decrease in notched strength resulting from a given hydrogen concentration; however, even at fluences in excess of 10^{20} n/cm^2, the lower critical stress to failure did not drop below the unirradiated notched strength with specimens containing up to 2 ppm hydrogen.

Specimens that had been specially heat-treated to hardness levels of approximately R_C36 prior to irradiation, however, were particularly prone to delayed failure. Typical results are shown in Figure I-8. Figure I-9 shows the effects of cold-working on the susceptibility to hydrogen embrittlement of irradiated A542 steel. Substantial amounts of cold-work render a material more susceptible to hydrogen embrittlement.

Lower critical stresses to failure as a function of unnotched ultimate strength for several hydrogen concentrations are summarized in Figures I-10 and -11. Figure I-10 shows that for steels in the normal quenched and tempered condition, increasing the strength level by irradiation hardening increases the degree to which these steels are susceptible to hydrogen embrittlement; but at the 2 ppm level, lower critical stress levels are still higher than unirradiated notched strengths. Figure I-11 summarizes the notched specimen test data for specially heat-treated or cold-worked specimens of A542 steel and shows a similar trend. However, specimens that had been heat-treated to a hardness of approximately R_C36 prior to irradiation were rendered notch sensitive after irradiation to a high fluence, ie, 4 to 5 x 10^{20} n/cm^2 E > 1 MeV. This condition was found to be particularly sensitive to hydrogen embrittlement as is indicated in Figure I-11.

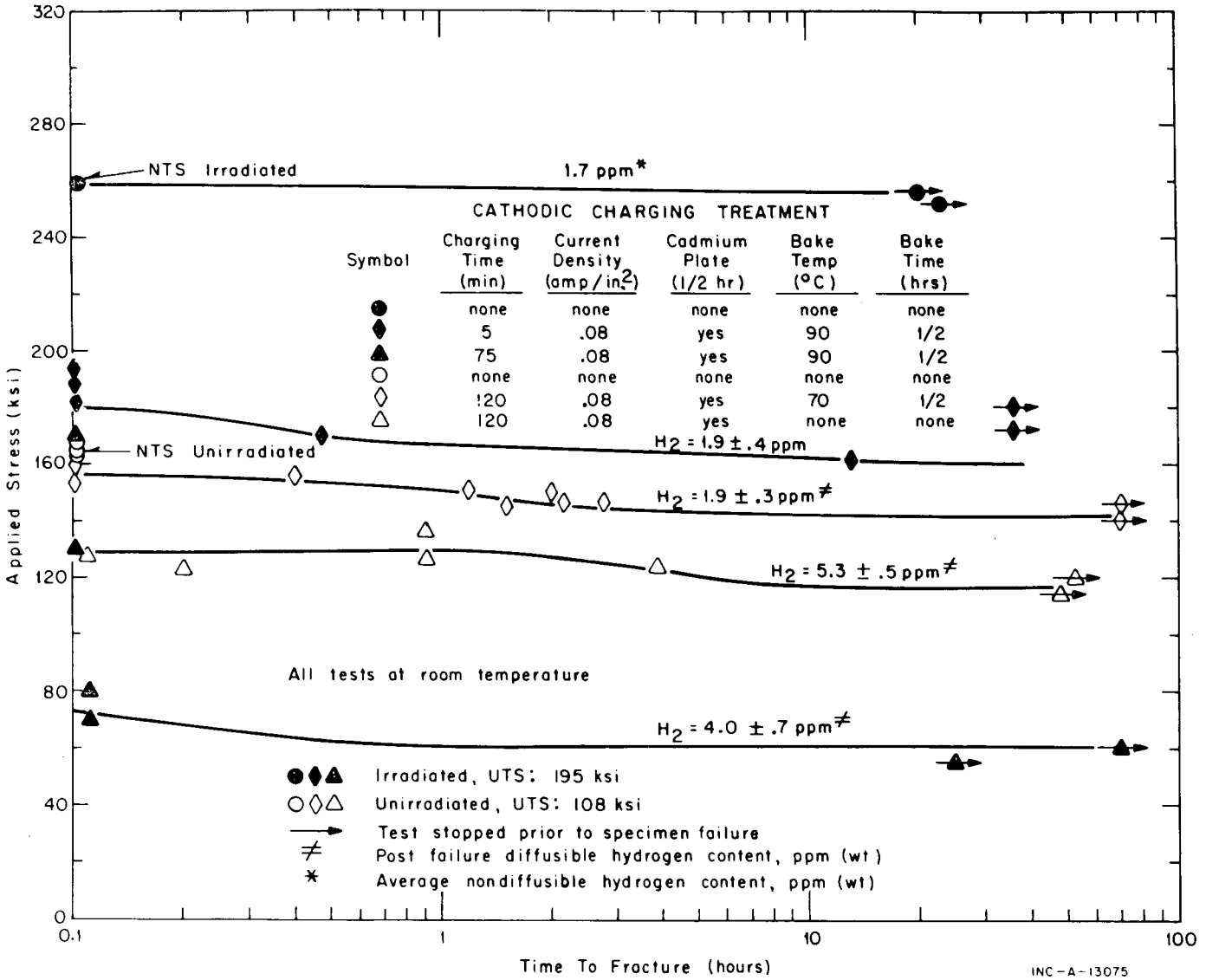

Fig. I-7 Constant load rupture curves compared for hydrogenated specimens of unirradiated and irradiated (to 2.2 x 10^{20} n/cm^2 E > 1 MeV) HY-80 (H.T. 81).

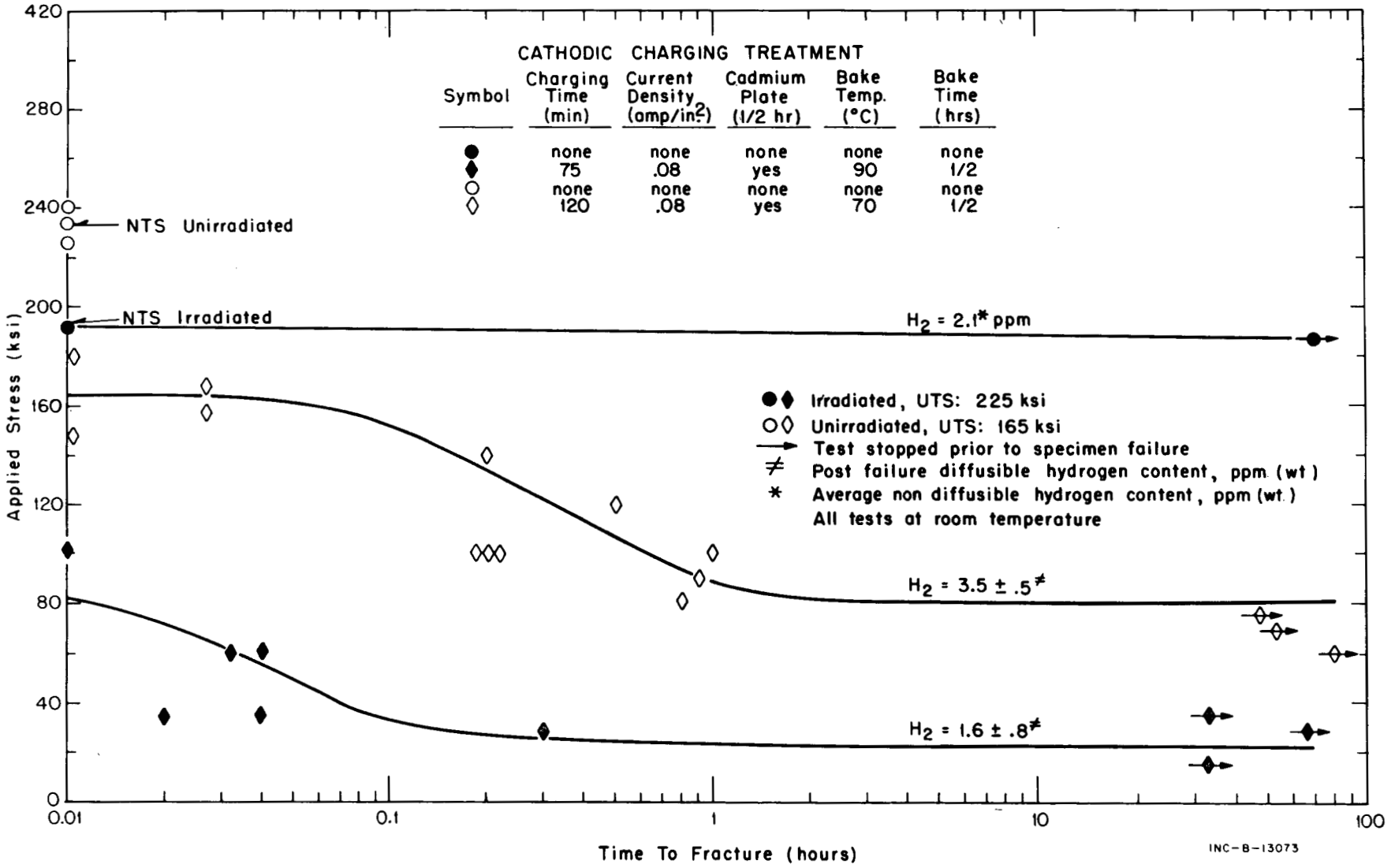

Fig. I-8 Constant load rupture curves compared for hydrogenated specimens of unirradiated and irradiated (to 4.2×10^{20} n/cm^2 E > 1 MeV) A542 steel that had been quenched and tempered to R_C 36 (H.T. 53).

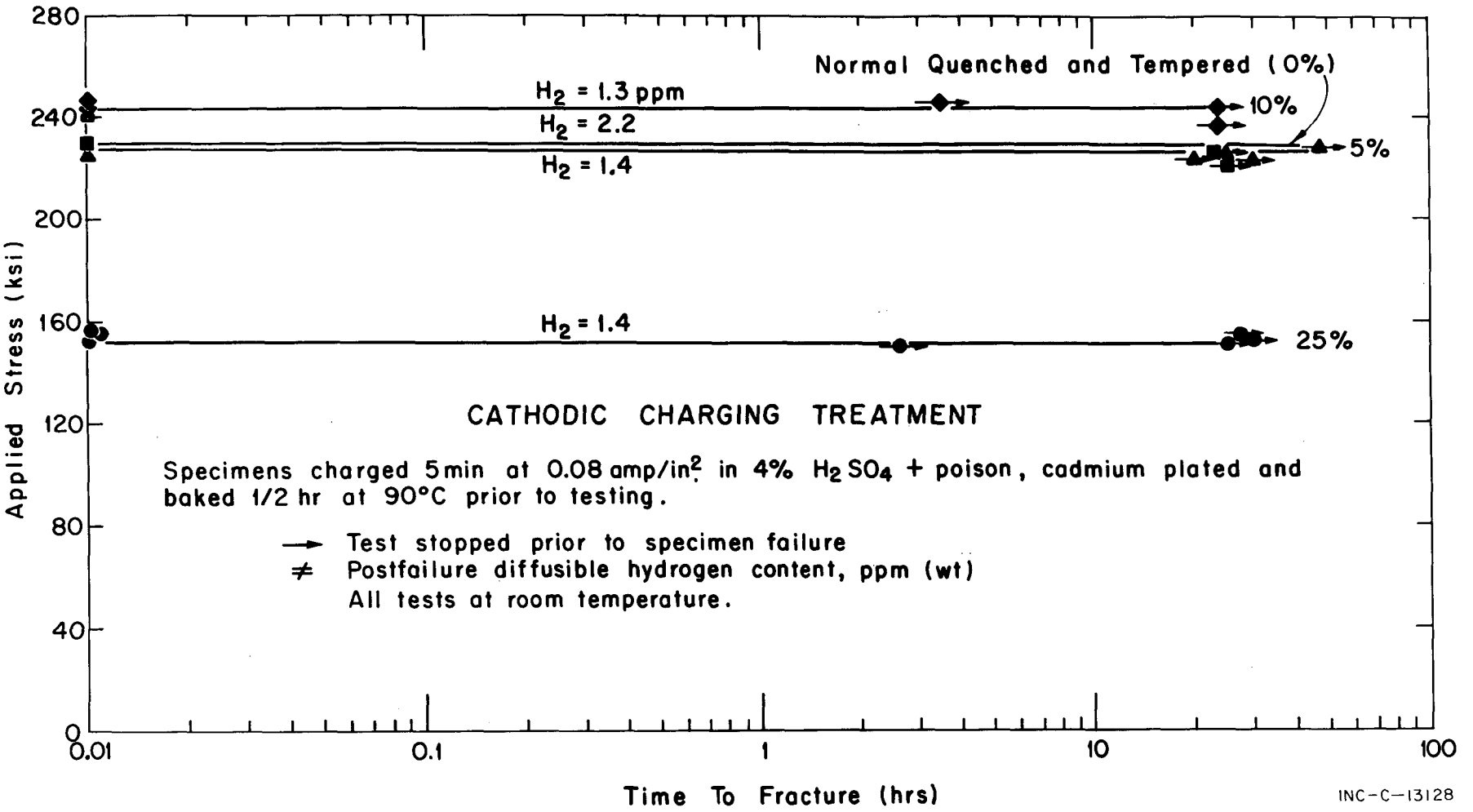

Fig. I-9 Constant load rupture curves compared for hydrogenated specimens of irradiated (1.6 - 2.4 x 10^{20} n/cm^2 E > MeV) A542 steel that had been cold-rolled 5 to 25% prior to specimen fabrication.

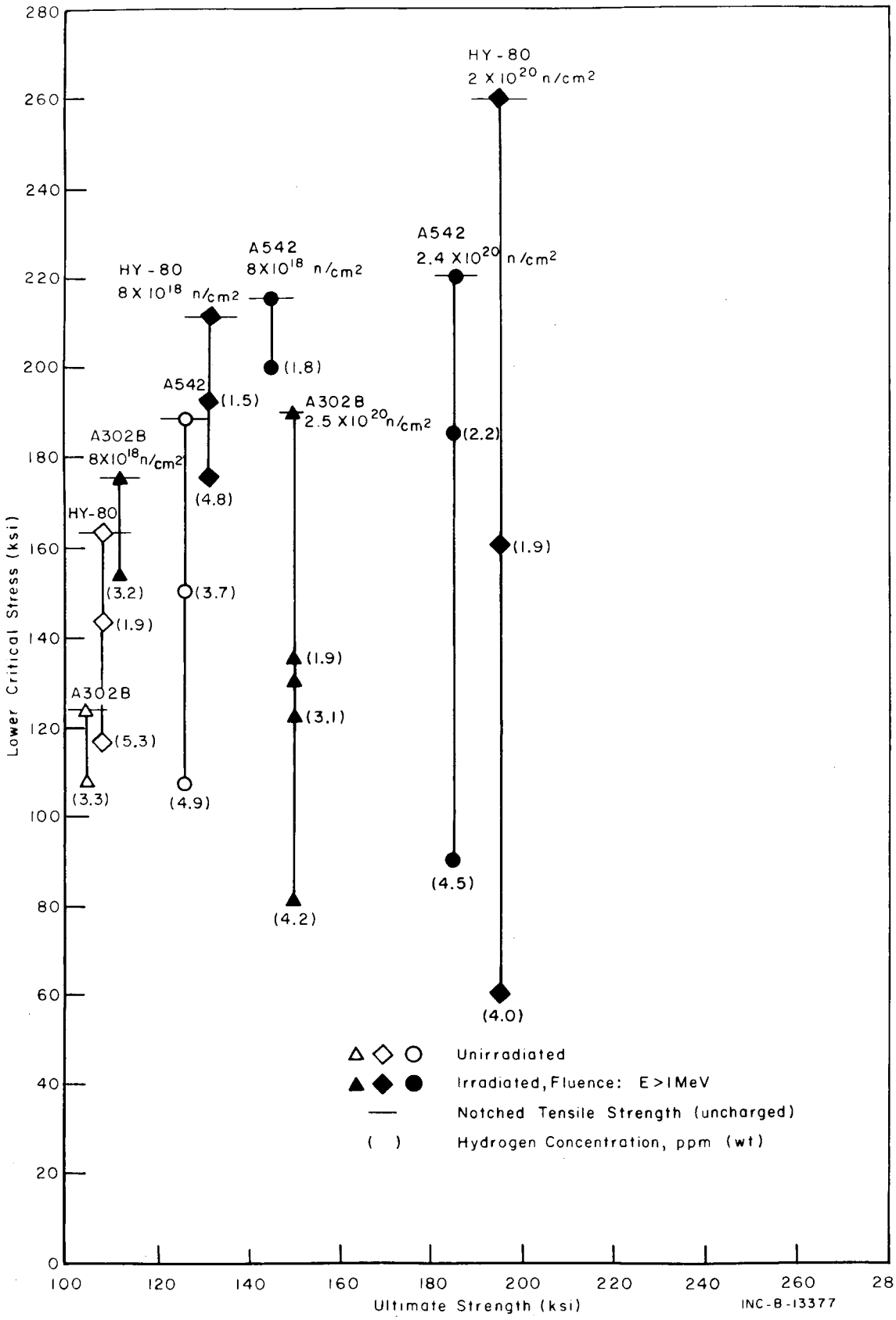

Fig. I-10 Lower critical stress levels for failure as a function of ultimate strength at various hydrogen concentrations for steels in normal quenched and tempered condition.

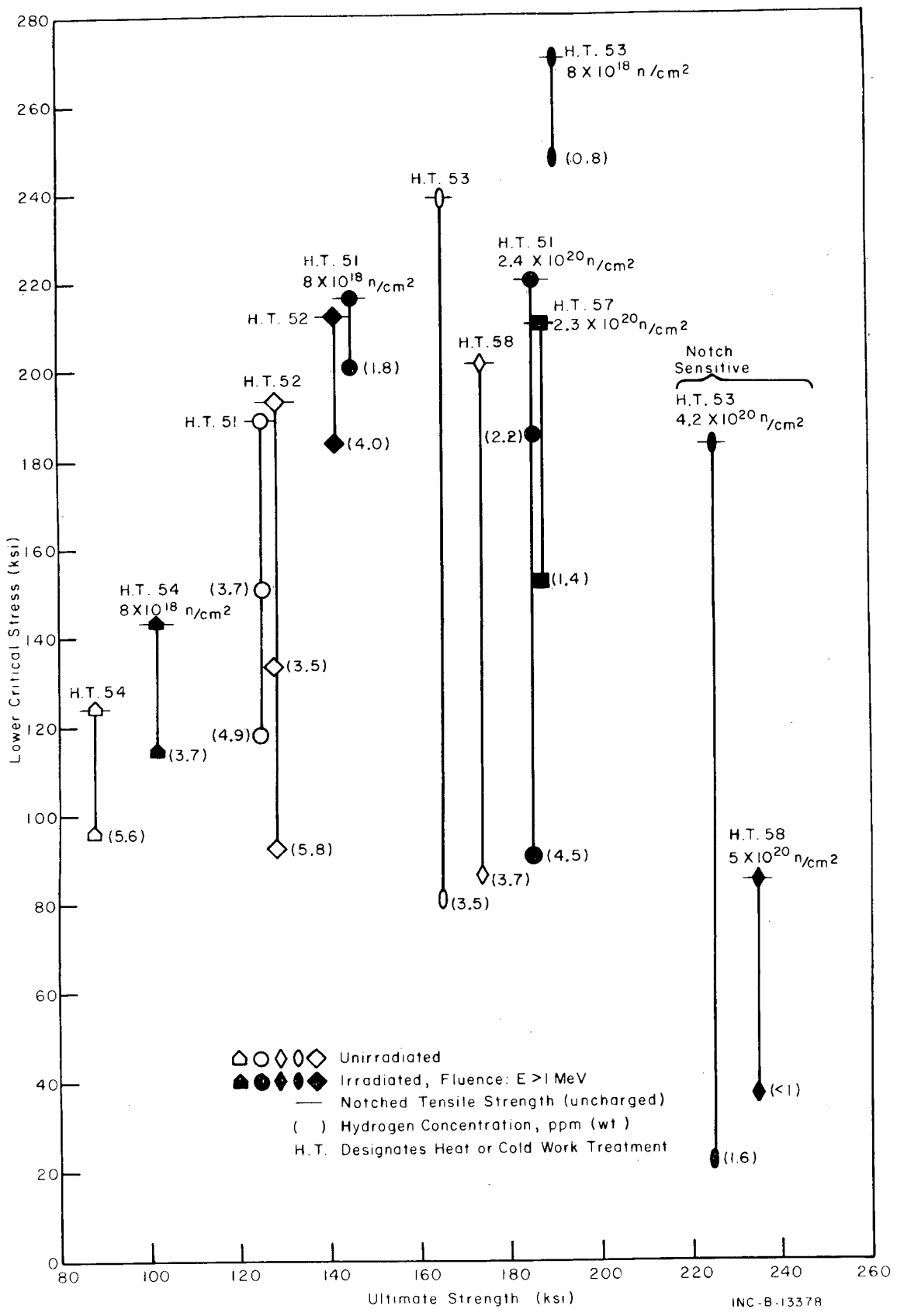

Fig. I-11 Lower critical stress levels for failure as a function of ultimate strength at various hydrogen concentrations for A542 steel heat-treated to several strength levels or cold-worked prior to irradiation.

1.3 Stress Wave Emission Monitoring of Hydrogen Induced Cracking

An acoustic emission is defined as an elastic or pressure stress wave that is generated within a metal during metal deformation, eg, the unpinning of dislocation pileups, failure of grains by shear or metal fracture. These waves travel to the metal surface where they can be picked up by a suitable accelerometer, amplified, and used to study microdeformation processes and crack propagation phenomena. Emissions produced have generally been defined as two types: (a) a continuous or low amplitude signal associated with microdeformation and (b) a high amplitude or burst type signal associated with such phenomena as crack growth or twinning.

As was discussed in the previous section, most of the material investigated in this program did not show extensive amounts of hydrogen-induced delayed failure leading to slow crack growth. However, specimens fabricated from material that had been specially heat-treated to R_C 35 were prone to delayed failure and therefore afforded the opportunity of studying crack growth by the acoustic emisssion or stress wave emission (S.W.E.) technique. A technique for remote mounting of an accelerometer and an extensometer to a specimen prior to loading was developed. Band pass filters were adjusted such that signals recorded would have a frequency content in the 45 to 65 KH_Z range. The S.W.E. pattern of the last seven minutes of a test lasting 45 minutes is shown in Figure I-12, where plots of cummulative bursts, bursts per second, and relative amplitudes of the bursts as a function of time are shown. Figure I-13 shows the S.W.E. pattern of another specimen test that was interrupted prior to specimen failure. The specimen was heat-tinted to delineate cracked area and then broken. From these tests it was possible to make the following conclusions:

(1) S.W.E. monitoring of constant load tests gives what appears to be evidence of discontinuous crack growth as seen by time intervals occurring between bursts or burst groups which decrease with increasing test time.

(2) Energy released by crack growth is proportional to the signal amplitude and increases with time until complete specimen failure.

(3) Progress of hydrogen-induced cracking may be estimated from S.W.E. patterns as evidenced visually on specimens taken from tests interrupted prior to failure and heat-tinted to show the position of the crack front, Figure I-13.

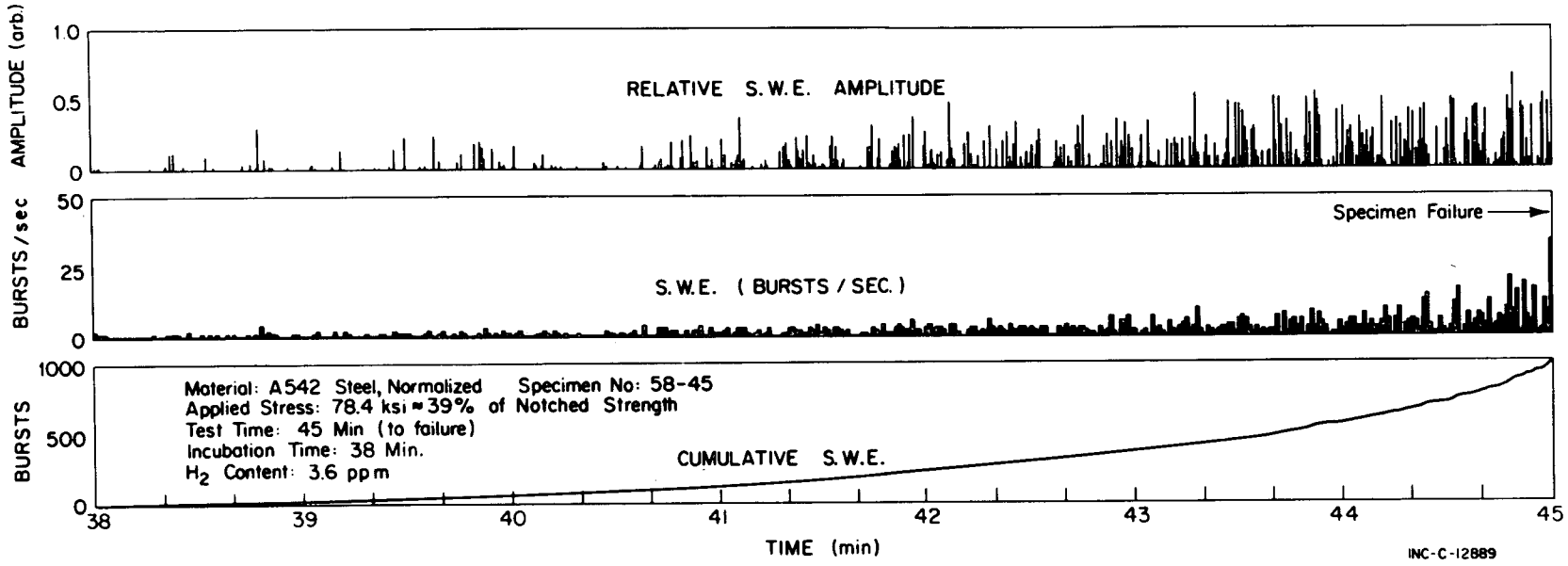

Fig. I-12 Sustained load test of hydrogenated A542 steel.

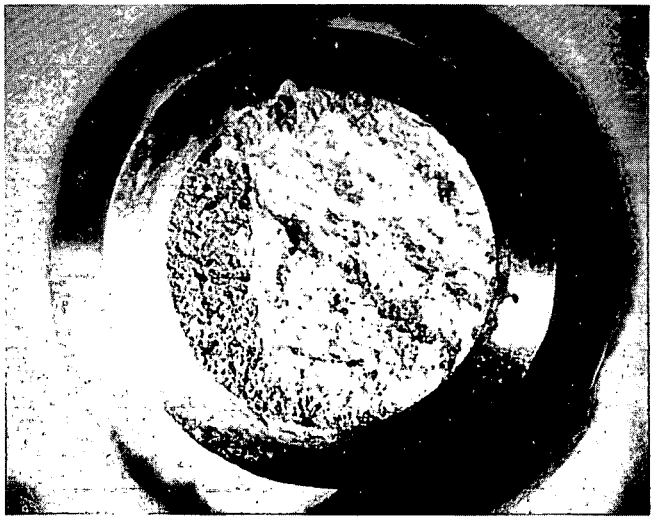

A. MATERIAL: A542 STEEL, NORMALIZED

SPECIMEN NO: 58-43

APPLIED STRESS: 85 ksi ≈ 42% OF NOTCHED STRENGTH

TEST TIME: 5.37 MIN. TEST INTERRUPTED PRIOR TO FAILURE

H_2 CONTENT: 3.5 ppm wt

*FRACTURE SURFACE -- HEAT-TINTED REGION DELINEATES CRACK AREA.

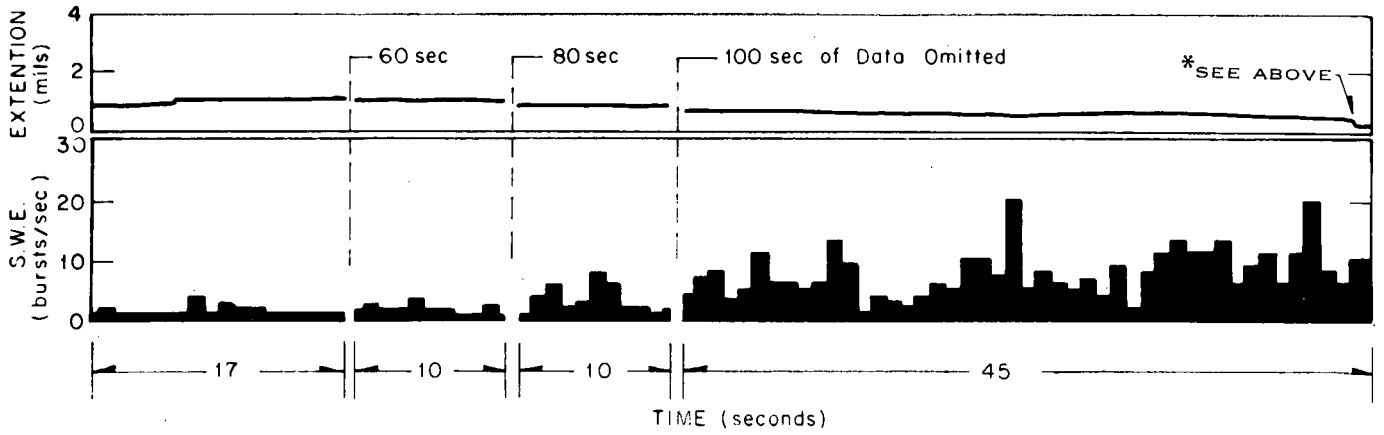

CORRESPONDING S.W.E. PATTERN.

Fig. I-13 Correlation between heat-tinted fracture surface and S.W.E. pattern.

2. SURVEILLANCE OF TEST REACTOR BERYLLIUM AND HAFNIUM

(G. E. Korth, J. M. Beeston)

The ATR surveillance program for monitoring the beryllium reflector continued during the year. Hafnium specimens are also added to the surveillance program to assist in monitoring changes of the ATR absorber sections.

Beryllium specimens in capsules were irradiated in the ETR K-6 and G-6 positions throughout the year. The samples had received fluences of 4.2 to 11.2 x 10^{21} n/cm^2 (E > 1 MeV) at the end of ETR Cycle 101. When the ATR startup runs are completed and the reactor begins cycle 1 (early fall, 1969), 50 capsules containing five beryllium specimens each will be transferred from the ETR to the ATR core where the specimens will continue to log fast fluences up to 7 x 10^{22} n/cm^2. Periodic removal and subsequent testing of the specimens will yield irradiation damage behavior of five types of beryllium (hot-pressed 2.0% BeO; hot-pressed 1.5% BeO; hot-pressed, hot-extruded 1.2% BeO; vacuum cast 1% BeO; and zone-refined single crystals with known orientations). From this data the service life of the ATR reflector and the best grade of beryllium to replace it can be predicted.

Eight capsules have been removed from the surveillance program, samples from three of which are currently being measured and tested. A summary of the tests completed to date is shown in Table I-1.

As can be seen from Table I-1 both fluence and fabrication history are variables in the irradiated behavior of beryllium. Metallography also supported the fact that fabrication history was a variable, ie, the mechanical twinning of compressive impact tested samples was seen in the extruded beryllium but not in the hot-pressed material. Compression tests revealed a similar effect with respect to twinning of both the extruded and hot-pressed grades.

Fractography and transmission electron microscopy were used in an attempt to detect helium bubble agglomerations. No helium bubbles were definitely identified in the as-irradiated material (using an electron microscope with a resolving power of 25 to 30A°). However, after annealing at 600°C or higher, both fractography and transmission microscopy revealed helium bubble agglomerates.

The hafnium neck shim rods in the ATR have been selected for surveillance since these particular rods will accrue fluence faster than any other hafnium poison inserts. Physical properties to be monitored are dimensional stability, strength, ductility, and microstructure. One shim rod will be removed, inspected, and a destruct test performed at intervals of about one year. Each rod replaced will be dimensioned to measure growth rates and then destructively tested to determine mechanical property changes. In addition to the shim rods, nine hafnium specimens machined from the same stock as the shim rods were encapsulated and will be inserted in the ATR core at the beginning of Cycle 1. Also, small hafnium plates that meet the ATR hafnium specification were metallurgically characterized and are currently being irradiated in the ETR. All preirradiation measurements and tests of hafnium surveillance specimens have been completed.

TABLE I-1

SUMMARY OF PARAMETERS MEASURED ON BERYLLIUM SURVEILLANCE SPECIMENS IRRADIATED IN THE ETR AT <150°C

Type Beryllium	Fluence (E > 1 MeV) x 10^{-21}	$\%\frac{\Delta L}{L}$[a] per 10^{21} n/cm^2	$\%-\frac{\Delta \rho}{\rho}$[b] per 10^{21} n/cm^2	%Δys[c]	%Δus[d]	%Δpd[e]	Impact Energy Absorbed for Failure, kg-M	%Total He Released to Capsule Annulus
Extruded	2.2	0.017	0.046	173	-29	-80	464	0.010
(1.2% BeO)	4.2	0.020	0.060	266	-16	-100	170	0.028
Hot-Pressed	2.3	0.029	0.074	247	12	-64	4822	--
(2.0% BeO)	4.8	0.024	0.065	347	-4	-100	4349	0.018
Hot-Pressed (1.5% BeO)	1.5	0.045	0.077	221	15	-61	2759	0.017
Vacuum Cast[f] (1% BeO)								

[a] Length change (growth).

[b] Density change.

[c] Compressive yield strength change as compared to unirradiated specimens.

[d] Compressive ultimate strength change as compared to unirradiated specimens.

[e] Change as compared to unirradiated specimens of plastic deformation -- strain at failure indicated by longitudinal cracking of the specimen minus strain at yield point. Note: -100%Δpd indicates that ultimate strength and yield strength were identical.

[f] No vacuum cast specimens have been tested as yet.

3. FATIGUE OF CLADDING AND STRUCTURAL MATERIALS

(J. M. Beeston, C. R. Brinkman)

Four MARK B-7 subassemblies containing 410 hourglass-shaped fatigue specimens have been prepared and loaded into EBR-II for irradiation. These subassemblies contain: specimens of stainless steel -- 110 type 304, 100 type 316, 10 type 304 Ti modified; 45 specimens of Incoloy 800; 15 of vanadium alloys; and 140 specimens of carbon steel. One of these subassemblies, X037, reached its design fluence and has been removed from the reactor. The irradiation temperature of the specimens was determined from sentinel wire [melting monitors and crusilite (SiC) slugs]. The specimen irradiation environment was one of three types: argon, purified sodium, or reactor sodium. The specimens in the sodium attained a temperature of 380 to 400°C while those in the argon reached a temperature of ~750°C. The reactor operated at 50 MW full power for approximately 29% of the time.

After letting the radioactivity decay for several months, the type 304 stainless steel specimens which were irradiated in argon at 750°C maximum temperature were tested in push-pull (axial) fatigue at 500°C in an argon environment; the specimens gave fatigue lives (N_{20}) approximately the same as the nonirradiated (as-received) material except at the low strain range (0.6% axial strain range) where the fatigue life of the nonirradiated material is greater, Table I-2. Additional irradiation and test conditions are given in the table footnotes. Control specimens, which are being heated for equivalent time at temperature are not ready for testing so that comparison of the fatigue properties is made with the as-received material (see footnote No. 3).

The irradiated and nonirradiated data tested at 500°C in argon is presented in Figures I-14 and -15 with nonirradiated data from Berling and Slot. Although there are differences in temperature and strain rate in the two curves of Berling and Slot[1], the current data does appear to be consistent with their temperatures and strain rates. The exception is at the high strain rate and low strain range where the two points for 500°C fall above the extension of their curve for 430°C at a comparable strain rate of 5×10^{-3}. It also should be noted that the fatigue life of N_{20} will be greater than N_5 which is the value selected by Berling and Slot (where N_{20} and N_5 refer to the number of cycles when the stress has dropped to 80 and 95% of the steady state value, respectively). It was desired to get as close to the fatigue life at failure (N_f) without damage to the extensometer or tester as possible, so that crack propagation data might be available; hence, N_{20} was selected, rather than N_5, for representing the fatigue life.

TABLE I-2

FATIGUE PROPERTIES[a] OF IRRADIATED[b] TYPE 304 STAINLESS STEEL[c]

Specimen No.	Fluence E > 1 MeV	Fatigue Life (N_{20})	Axial Strain Range (Percent)	Elastic Strain Range (in./in.)	Plastic Strain Range (in./in.)	Stress[d] Range (ksi)	Specimen No.	Diametral Strain Range (in./in.)	Elastic Strain Range (in./in.)	Plastic Strain Range (in./in.)	Width[f] Hysteresis Loop (in./in.)	Slope[g] E/ν ($lb/in.^2$)
I-D-7-65	2.87×10^{20}	2,069[e]	1.01	0.0036	0.0065	81	I-D-7-65	0.0043	0.0011	0.0029	0.0029	68×10^6
-66	4.00	3,912	1.02	0.0034	0.0068	78	-66	0.0044	0.0014	0.0030	0.0032	69
-67	5.15	3,162	1.00	0.0035	0.0065	79	-67	0.0043	0.0010	0.0033	0.0030	65
-68	4.16	14,025	0.58	0.0026	0.0032	59	-68	0.0023	0.0008	0.0015	0.0012	60
I-D-2-70	6.07	12,196	0.60	0.0031	0.0029	70	I-D-2-70	0.0023	0.0009	0.0014	0.0011	63
-74	4.92	490	1.96	0.0043	0.0153	98	-74	0.0089	0.0013	0.0076	0.0089	68

[a] Test conditions: Atmosphere-argon with <1 ppm O_2, gauge temperature 500°C, axial strain rate 4×10^{-4} in./in. sec, push-pull with $R \cong -1$ and $A \cong \infty$.

[b] Irradiation conditions: Atmosphere-argon, temperature ~750°C, reactor position-7C3 in EBR-II.

[c] Stainless steel type 304; heat No. 55697; composition (%) 0.053C, 0.87Mn, 0.018P, 0.012S, C.49Si, 18.41Cr, 9.71Ni; heat treatment, hot-rolled at 1175°C to 5/8-inch diameter rod and coiled. The coils were annealed at 1070°C for one hour, WQ. To eliminate straightening effects the rods were annealed at 1010°C for 1/2 hour and WQ.

[d] Stress range at fatigue life of $\sim N_{20}/2$, where N_{20} is the number of cycles when the stress has dropped to 80% of the steady state value.

[e] A power outage fractured this specimen prematurely.

[f] The width of the hysteresis loop is the measured diametral plastic strain range.

[g] The slope of the unloading part of the hysteresis loop. In calculation of the strain values E at 500°C was taken as 22.6×10^6, and ν was taken as 0.296 which gives a value of 76.4×10^6.

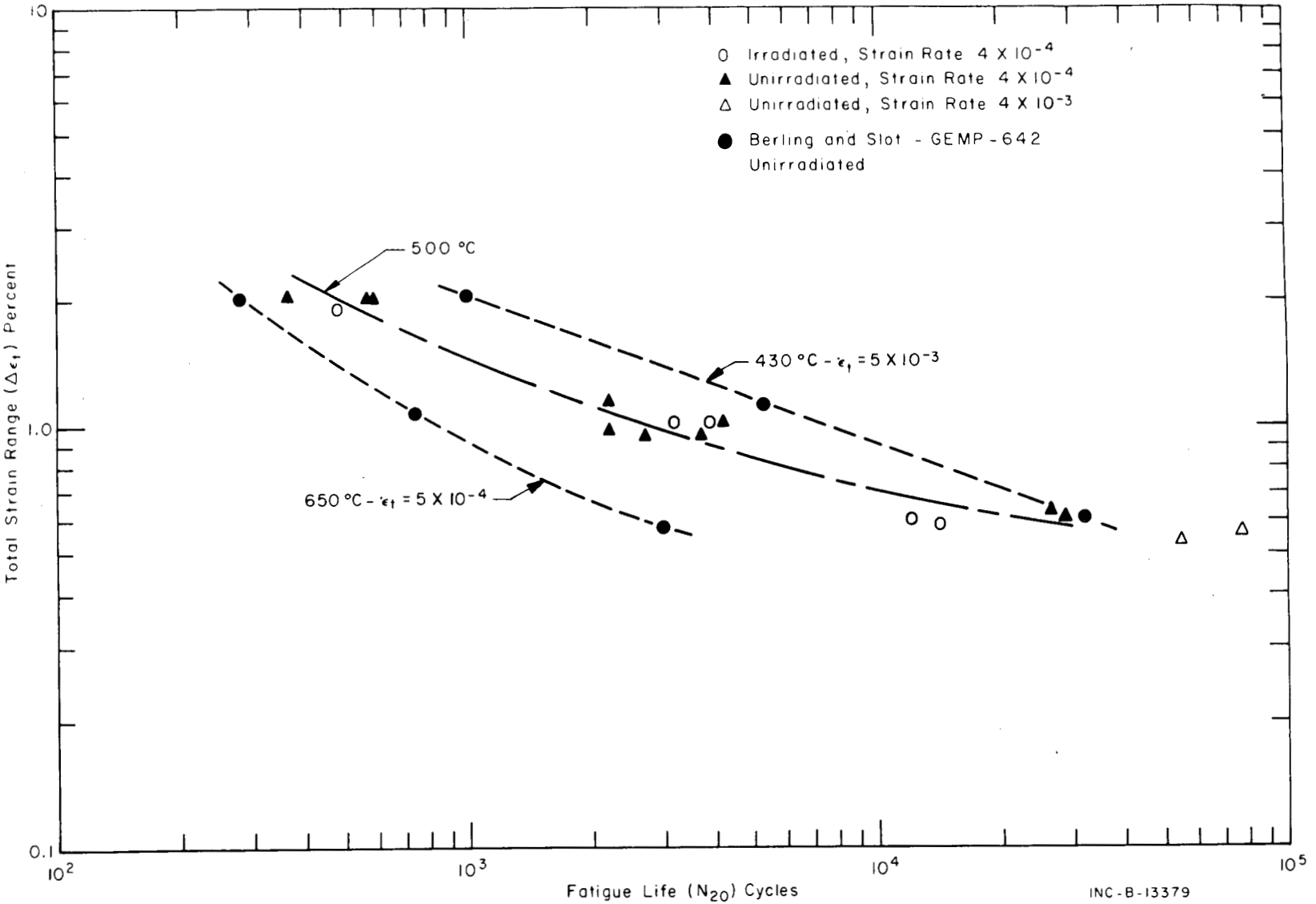

Fig. I-14 Fatigue life versus total strain range of type 304 stainless steel.

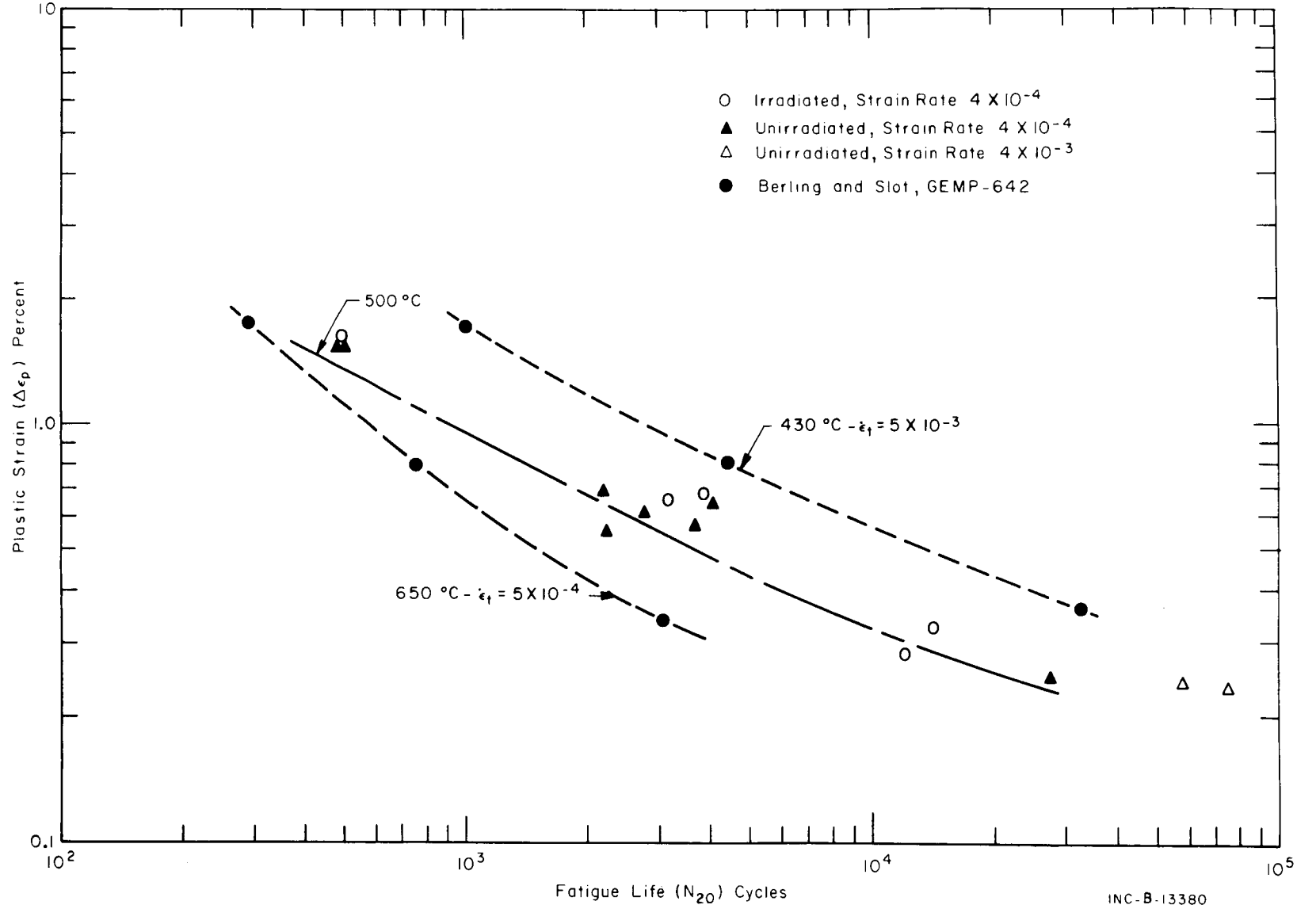

Fig. I-15 Fatigue life versus plastic strain of type 304 stainless steel.

4. REFERENCE

1. J. T. Berling and T. Slot, Effective Temperatures and Strain Rate on Low-Cycle Fatigue Resistance of AISI 304, 316, and 348 Stainless Steels, GEMP-642, June 24, 1968.

II. REACTOR FUELS AND MATERIALS DEVELOPMENT

1. PROTOTYPE ELEMENTS

1.1 The Testing of B_4C Impregnated Aluminum Foils as Controllable Neutron Absorbers for Nuclear Reactor Fuel Elements (G. O. Hayner, G. W. Gibson, B. G. Carlson, R. J. Pollard)

In a previous annual report[1], the development and preliminary testing results of boron-aluminum foil fuel plates was given. During FY-1969, two unirradiated ETR B_4C foil fuel elements and three irradiated ETR B_4C foil elements were destructively examined and evaluated. Table II-1 shows the number of foil elements that have been used in the ETR through Cycle 103.

TABLE II-1

UNITED NUCLEAR BORON FOIL-TYPE FUEL ELEMENTS USED IN THE ETR

ETR Cycle Number	Number of Foil Elements in the ETR	Core Power Designation[a]
97	3	Medium
99	17	Low
101	17	Low
102	14	Low
103	14	Low
103	3	High

[a] Low power position designates less than 1.6% core power.
Medium power position designates between 1.6 and 2.0% core power.
High power position is greater than 2.0% core power.

The results of the examinations conducted on the unirradiated fuel elements (except the melting point study) were evaluated to the requirements of Idaho Nuclear Corporation specification PPCS-250, Revision 3, and Addendum No. 1 (Subcontract S-292 and -294) to this specification. The following summarizes the results of the examination of the above fuel elements:

1.11 Destructive Examination of Unirradiated ETR B_4C Foil Element XE-19-G. Element XE-19-G was randomly chosen for examination after the first 20 elements were received by Idaho Nuclear (July 1, 1968) and had successfully passed receiving inspection.

The examination that was carried out was designed to evaluate:

(1) Boron homogeneity within an element

(2) Uranium control as an alloy at the 500 g load level

(3) Bonding of the B_4C + Al foil to the fuel halves; bonding of the fuel halves to the cladding material

(4) Effect of the foil on ultrasonic scans

(5) Deviations from specified clad-core-clad dimensions.

The results of the examination determined that the boron and silicon variation from plate to plate within the element was within specifications. The uranium content in plate KRB-35 was found to be high. The analysis for these elements was made by dissolution of one plate (KRB-35) and selective punchings taken from two other plates (KRB-36 and KRA-49) within the element. Results on plate KRB-35, which was totally dissolved, can be seen in Table II-2.

TABLE II-2

ANALYSIS OF ETR FUEL PLATE KRB-35[a]

Total[b] Boron mg	B-10 wt%	B-11 wt%	Total[c] Uranium, g	U-234 wt%	U-235 wt%	U-236 wt%	U-238 wt%
210 ± 2	18.34	81.66	29.45 ± .06	0.63	93.14	0.29	5.95

[a] The plate weighed 254.2 g.

[b] The specified boron content per plate was 200 ± 40 mg.

[c] The specified uranium content per plate was 28.2 ± 0.8 g.

Results from plate KRB-36, from which boron and uranium punchings were taken, are given in Tables II-3 and -4. Plate KRA-49 was also destructively

TABLE II-3

URANIUM IN ETR FUEL PLATE PUNCHINGS TAKEN FROM KRB-36

Sample Code	Sample wt(mg)	Uranium[a] mg/sample	U-234 wt%	U-235 wt%	U-236 wt%	U-238 wt%
KRB-36 U1	12.852	1.699	0.62	93.15	0.28	5.95
U2	12.847	1.866	0.63	93.16	0.28	5.92
U3	12.882	1.731	0.64	93.13	0.29	5.95
U4	12.859	1.858	0.63	93.13	0.29	5.95
U5	12.641	1.657	0.64	93.13	0.29	5.94
U6	12.830	1.778	0.64	93.12	0.29	5.95

Average 1.765 ± 0.104 (5.9%)

[a] The specified uranium content per punching was 1.65 ± 0.33 mg.

TABLE II-4

BORON AND SILICON IN ETR FUEL PLATE PUNCHINGS TAKEN FROM KRB-36

Sample Code	Boron[b] µg/g Sample	Silicon wt%[a]	Sample wt, g
KRB-36 B1	412		0.4980
B2	389	0.75	0.5037
B3	378		0.4970
B4	355		0.5015
B5	438	0.75	0.4963
B6	391		0.5026

Average 394 ± 40 (10.2%)

[a] Three samples were combined for one silicon analysis.

[b] No specification is given in S-292 for boron content per punching, however, in S-294-IN-F-7, ± 30% of the nominal boron content per punching is specified.

examined with similar results as shown for KRB-36. The sectioning procedure for each plate, with the uranium and boron sampling plan, is shown in Figure II-1.

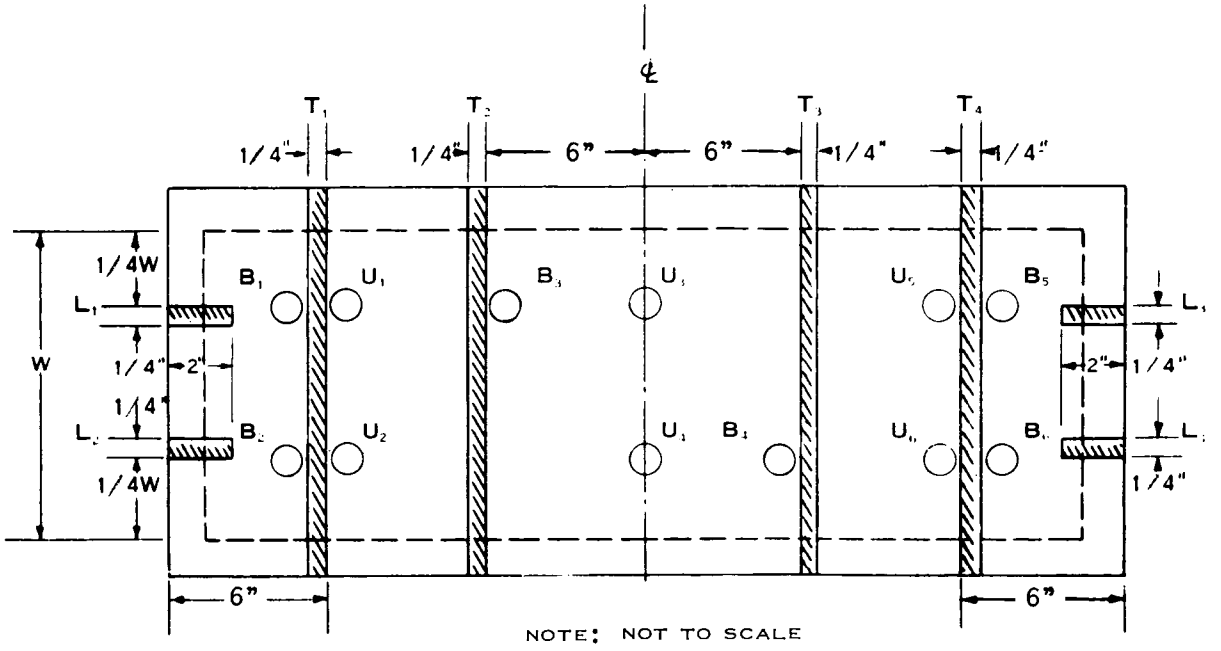

Fig. II-1 Fuel plate sampling procedures used for the destructive tests. The "L" and "T" samples were prepared for metallographic examination. The "U" samples were 0.080-inch diameter punchings used for uranium analysis. The "B" samples were 1/2-inch diameter punchings used for boron analysis.

The relative strength of the foil bond to the fuel halves was determined by a 180-degree bend test to destruction. The strength of the fuel bond to the cladding material was determined by the above bend test, metallographic

examination, and subsequent estimation of percent grain growth across the interface region. Bonding for all 19 plates examined was found to be acceptable, grain growth across bond interfaces varied between 75 and 95%, and bend tests showed no noticeable tearing at bond regions.

There were no detectable nonbonds in any of the 19 plates examined by ultrasonic scanning techniques. Macroscopic "boron clumping" in the B_4C + Al foil was not detected in any of the scans. However, in microscopic examinations, as seen in Figure II-2, some clumping of the B_4C in the foil was noted.

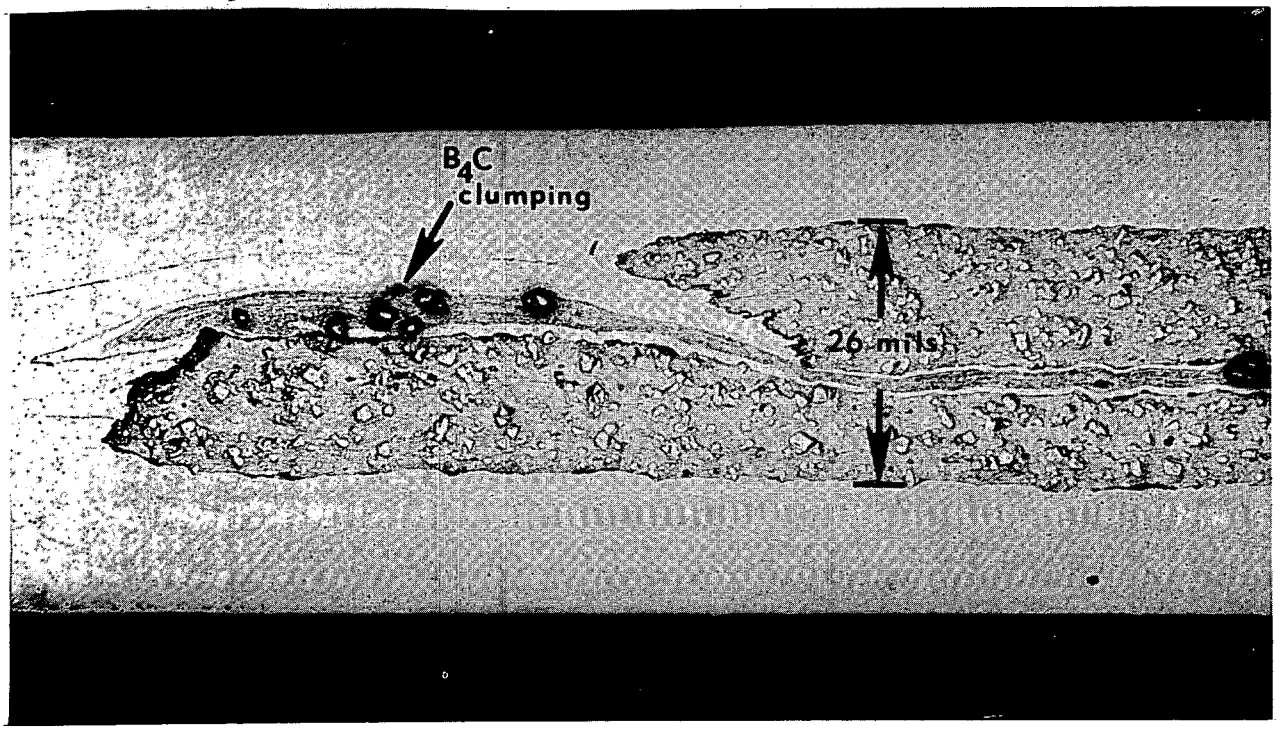

As-polished 50X

Fig. II-2 Typically shaped "dogbone" area. The B_4C "clumping" noted at center generally did not appear in most "dogbone" regions. Measurement of greatest core thickness is shown.

Therefore, this "clumping" would seem to be undetectable by ultrasonic scanning techniques calibrated for detection of macroscopic nonbonds.

Clad-core-clad dimensions and overall thickness of the fuel plates were within specifications. All measurements were within 20 +0 to -2 mil core thickness and 50 ± 1 mil total plate thickness. Some "dogboning" of the core was noted, however, this also was within specifications and did not exceed 26 mils core thickness at any high "dogbone" area. A typically shaped core "end" area is seen in Figure II-2.

1.12 Destructive Examination of Unirradiated ETR B_4C Foil Element XE-28-G. Element XE-28-G was randomly chosen for examination after all 40 elements had successfully passed receiving inspection. The examination of this fuel element was the same as that conducted for XE-19-G except that a study of the melting points of the core constituents also was made. This latter study was made on samples removed from fuel plate KRE-92 and designed to evaluate the behavior of the core materials during a meltdown situation.

The results of the examination determined that the uranium, boron content, and distribution from plate to plate within the element were within specifications. The analysis for this element was made by dissolution of one plate (KRE-14) and selective punchings taken from two other plates (KRG-16 and KRA-85) within the element. Results of plate KRE-14 can be seen in Table II-5. Results

TABLE II-5

ANALYSIS OF ETR FUEL PLATE KRE-14

Total[d] Boron, mg	B-10 wt%	B-11 wt%	Total Uranium, g	Total[c] U-235, g	Isotopic Distribution, wt% U-234	U-235	U-236	U-238
205.9 ± 0.4[a]	19.82	80.18	29.23 ± 0.07[b]	27.23 ± 0.08	0.63	93.16 ± 0.06	0.29	5.92

[a] The average of seven analyses.

[b] The average of duplicate analyses.

[c] Specification for U-235 in this plate is 26.5 ± 0.8 g.

[d] Specification for boron in this plate is 184 ± 40 mg.

from plate KRG-16, from which boron and uranium punchings were taken, are given in Tables II-6 and -7. Plate KRA-85 also was destructively examined

TABLE II-6

BORON IN ETR FUEL PLATE PUNCHINGS

Sample Code	Sample wt (g)	Boron[a] µg/sample	Boron µg/g
KRG-16 B-1	0.4990	435	871
B-2	0.4959	490	989
B-3	0.4986	480	963
B-4	0.4940	469	949
B-5	0.4966	497	1000
B-6	0.4944	506	1023

Average 479 ± 25.4 (5.3%)

[a] No specification is given for boron content per punching in S-292; however, in S-294-IN-F-7, ± 30% of the nominal boron content per punching is specified.

TABLE II-7

URANIUM IN ETR FUEL PLATE PUNCHINGS

Sample Code	Sample wt (mg)	Total Uranium, %	Isotopic Distribution, wt% U-234	U-235[a]	U-236	U-238	U-235[b] mg/sample
KRG-16 U-1	12.89	14.52	0.61	93.14	0.30	5.95	1.744
U-2	12.74	13.00	0.60	93.16	0.30	5.94	1.543
U-3	12.80	13.32	0.61	93.15	0.29	5.94	1.588
U-4	12.81	13.12	0.61	93.14	0.31	5.95	1.566
U-5	12.80	13.96	0.61	93.16	0.29	5.94	1.665
U-6	12.60	12.54	0.60	93.19	0.29	5.92	1.472

Average 1.596 ± 0.095 (5.6%)

[a] The standard deviation to be associated with this value is ± 0.06.

[b] Specification for U-235 is 1.54 ± 0.31 mg/sample (range).

with similar results. The sectioning procedure for each plate, with the uranium and boron sampling plan, is seen in Figure II-1.

Bonding for all 19 plates examined was found to be acceptable, grain growth across bond interfaces varied between 60 and 90%, and bend tests showed no noticeable tearing at bond regions.

There were no detectable nonbonds in any of the 19 plates examined by ultrasonic scanning techniques. Macroscopic or microscopic "boron clumping" in the B4C + Al foil was not seen in any of the scans or microscopic examinations.

Clad-core-clad dimensions were found to be outside specifications. The overall thickness of the plates was within specifications. However, in many plates examined the core thickness (in both "nondogbone" and "dogbone" areas) was found to be greater than that specified. Plates KRA-85 and KRF-22 had maximum core "dogbone" areas of 30 mils. All of the plates examined except six (18 plates were examined) had "dogbone" areas in excess of 26 mils. Core thicknesses obtained in the transverse sections were quite uniform although many 22 mil sections were observed.

The melting point test samples removed from fuel plate KRE-92 were examined in a hot stage metallograph to compare the melting temperatures of the core constituents. This was done to evaluate the possibility of the UAl alloy core "slumping" away from the B4C poison foil layer during a fuel plate meltdown situation. Figure II-3 shows an as-received section from plate KRE-92. The two black areas in the center of the photomicrograph represent B4C particles in the center-line foil layer. The fuel particles are a nominal 30 wt% uranium-UAl alloy. The clad, matrix, and foil layers are composed of 1100 aluminum.

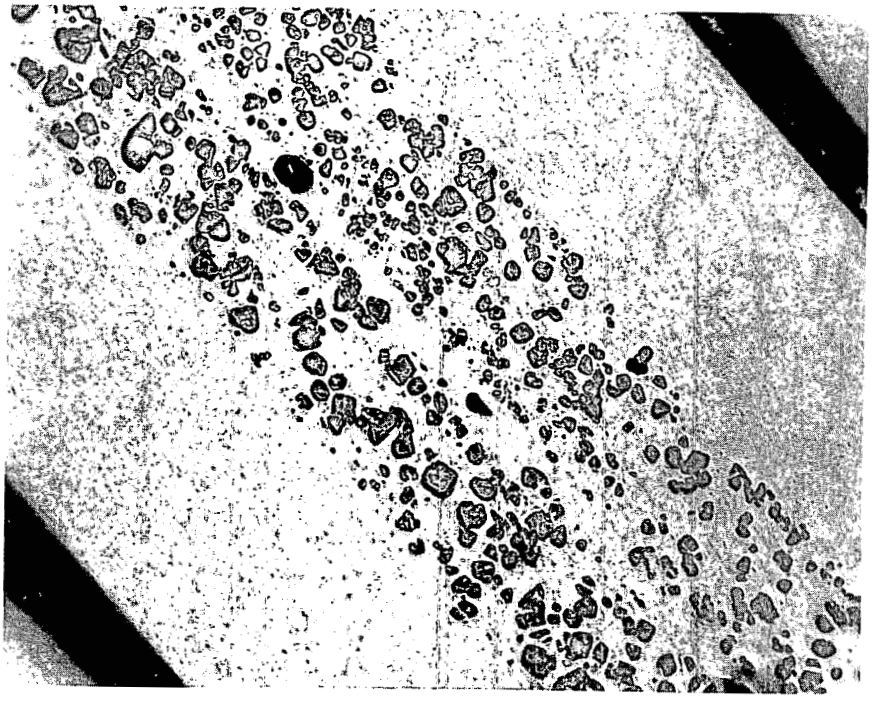

As-polished

Fig. II-3 As-received section of plate KRE-92, element XE-28-G.

This section was then heated slowly in a hot stage metallograph until some melting of the core was initially detected at 635°C. Heating was continued, and at 640°C, some intergranular penetration of the B_4C foil layer (Figure II-4)

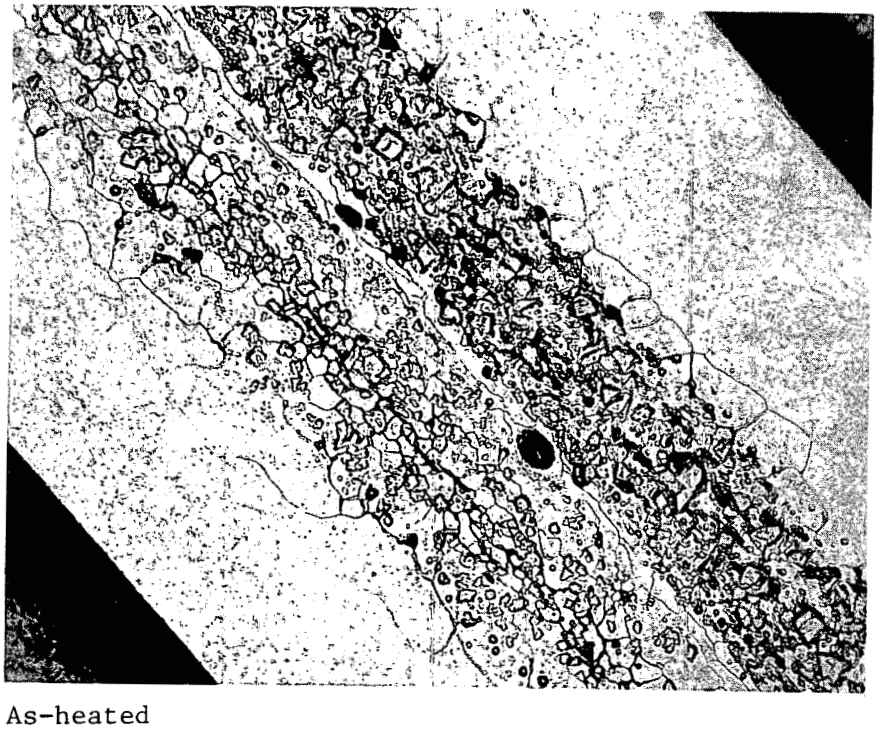

As-heated

Fig. II-4 Same section (as shown in Fig. II-3) at about 640°C. Melting of the core matrix is well along in the bottom section of fuel.

was noted. Figure II-5 shows this same area at 645°C. Here the UAl_4 particles are in a molten eutectic and the B_4C foil layer is partially melted and alloyed with the fuel matrix. Penetration of the cladding is also noted in the grain boundaries near the core. Still further heating indicated that melting of both clad and core was complete at 660°C.

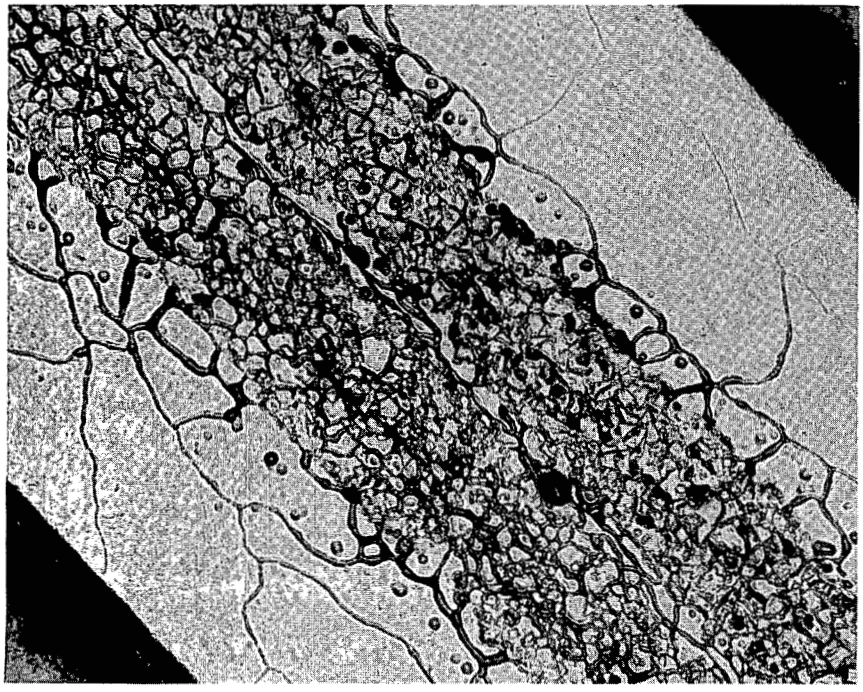

As-polished

Fig. II-5 Same section (as shown in Fig. II-3) at about 645°C. UAl_4 particles are in molten eutectic. Cladding has been penetrated in the grain boundaries near core.

1.13 Postirradiation Examination of ETR "Boron Foil" Elements XE-2-G, XE-3-G, and XE-4-G. ETR "boron foil" elements XE-2-G, XE-3-G, and XE-4-G were from the first 20 "boron foil" elements produced by the vendor and received at Idaho Nuclear Corporation by July 1, 1968. The elements were operated in a medium power position in Cycle 97 of the ETR. The burnup data for these three elements is given in Table II-8.

A careful visual examination of the flow channels and fuel plate surfaces of all 19 plates in the three elements disclosed no indication of any lack of soundness in the elements nor any sign of notable blistering or swelling.

A complete thickness survey was made on the two hottest plates in elements XE-2-G and XE-3-G. The survey was made on all of the plates in XE-4-G. After chemical stripping of the oxide coating on the plates, the range of the thickness readings was two mils with an average total plate thickness of approximately 51 mils. This would indicate good uniformity and only a small increase in plate thickness.

A Dermitron thickness measurement of the Al_2O_3 coating that formed on the surface of the plate during irradiation was made on those plates measured for total thickness. The range of oxide thickness for each side of the plates was 0.30 mil (0.59 to 0.89 mil). The average reading was 0.70 mil. These thicknesses are typical for 1100 aluminum in the ETR for one cycle (six weeks).

TABLE II-8

REACTOR CONDITIONS FOR FUEL ELEMENTS XE-2-G, XE-3-G, AND XE-4-G

Serial Number	XE-2-G	XE-3-G	XE-4-G
Core position	F12	G14	H14
Initial fuel content (g)	507.5	507.2	507.7
Percent of total core power	2.02	2.03	2.05
Total core MWd	5310	5310	5310
Total fuel burnup in elements (g)	134.1	134.7	136.1
Ratio of peak axial flux to average axial flux	1.31	1.31	1.31
Ratio of peak midplane flux to average midplane flux	1.86	1.56	1.50
Fractional Fuel Burnup			
Overall average	0.26	0.27	0.27
Average in hot spot plane	0.33	0.33	0.34
Hot spot in element	0.53	0.47	0.46

Figure II-6 shows the blister temperature of samples from "boron foil" elements XE-2-G and XE-4-G compared with the established failure-no-failure line for sample fuel plates with UAl + B_4C dispersed in aluminum. It can be seen from Figure II-6 that the "boron foil" samples irradiated to a maximum of 8 x 10^{20} fissions/cc compare reasonably well with powder metallurgy type fuel plates in respect to blister resistance. This would imply that the B_4C distribution was uniform in these B_4C plates because clumping of the B_4C has caused blistering at a lower temperature and thus failure of the fuel plate.

Metallography performed on the blister annealed samples revealed that the blisters originated within the "boron foil" and in some cases (the larger blisters) extended from there into the fuel core areas or the fuel core to cladding interface. All of the blisters observed were associated with the particles of B_4C within the foils. It can be seen from a blister resistance standpoint that the B_4C impregnated aluminum foil is the weak point in the fuel plate. However, the plates still show a high blister resistance threshold (as seen in Figure II-6). A typical blister microstructure for the "boron foil" plates is shown in Figure II-7.

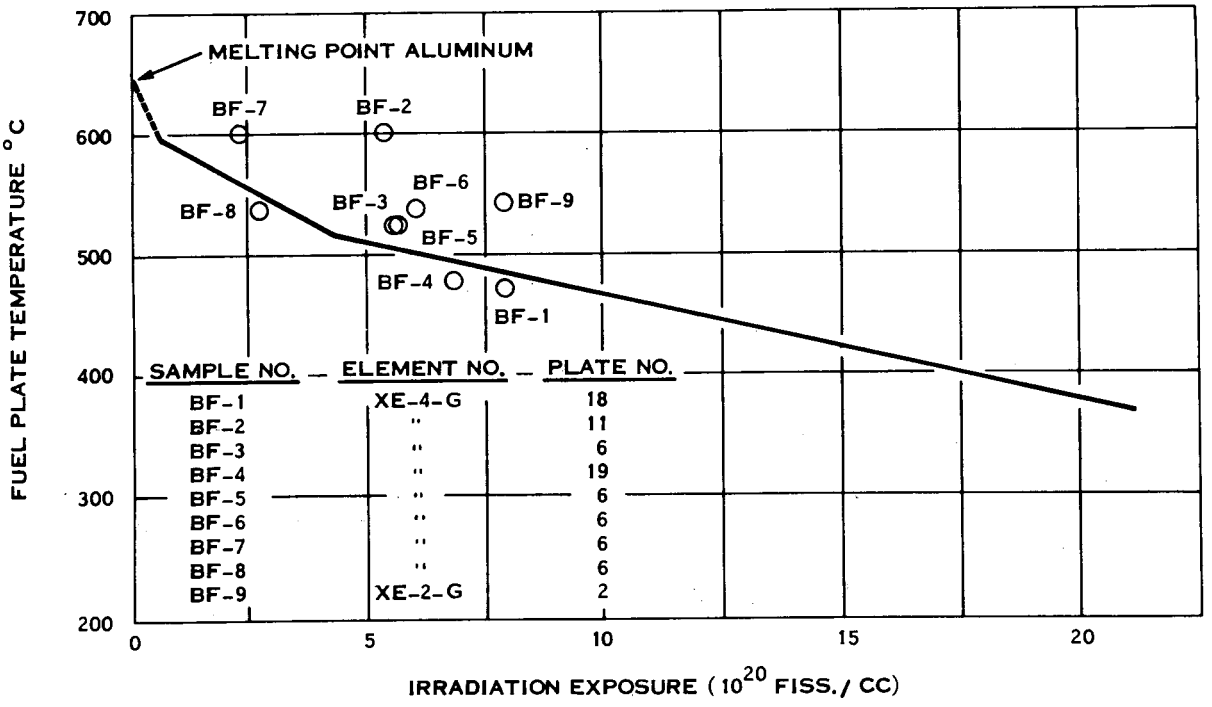

Fig. II-6 Blister temperatures of samples from boron foil fuel elements XE-2-G and XE-4-G compared with the established failure-no-failure line for sample fuel plates with $UAl_x + B_4C$ dispersed in aluminum.

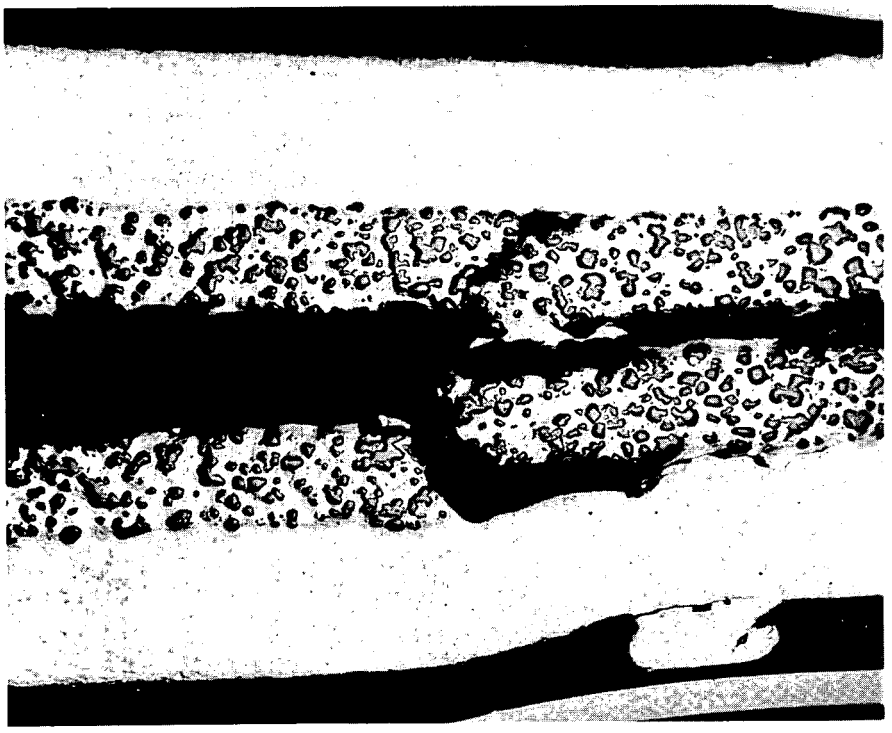

As-polished 50X

Fig. II-7 Typical blister microstructure from element XE-4-G, plate 19, showing the origin of the blister in the foil area with blisters extending into the core-cladding interface. The blister temperature for this sample was 482°C. The average fission density for this sample was 6.88 x 10^{20} fissions/cc.

The following conclusions were made from the examination of five ETR B_4C foil fuel elements (XE-19-G, XE-28-G, XE-2-G, XE-3-G, and XE-4-G):

(1) The uranium and boron loading within each plate examined was generally quite uniform, comparable in this respect to standard elements used in the ETR. However, the U-235 content in one plate examined (KRB-35) was determined to be high by approximately 0.4 g over the specified content. This would imply that better control of this parameter should be maintained.

(2) A considerable number of the fuel plates examined in both XE-19-G and XE-28-G were not within specifications for either core thickness or "dogbone" thickness (20 +0 to -2 and 26 mils maximum, respectively).

(3) The results of all other tests performed on XE-19-G and XE-28-G indicate that these elements were generally within all other specifications evaluated.

(4) The melting point examination of the core constituents from samples removed from fuel plate KRE-92 (element XE-28-G) would seem to indicate a desirable condition if a meltdown accident occurred.

If the heat source was the fuel core and the clad was partially cooled (the case occurring during fuel plate meltdown), the over heating would cause subsequent melting of the core fuel material which would penetrate the 1100 aluminum B_4C impregnated foil layer. It is, therefore, very likely that a foil element would have the B_4C flowing with the molten fuel.

(5) The postirradiation examination performed on XE-2-G, XE-3-G, and XE-4-G showed no sign of excessive plate swelling or corrosion buildup. The gamma scans of the plates within these elements were uniform with no peaks or breaks in the general activity pattern. The plates performed well during blister testing. However, metallography showed that the foil area of the plates examined is the weak point in relation to blister resistance.

(6) This type of fuel element can safely be used in low and medium power positions (less than 2.0% of reactor power) of the ETR and should be tested in high power positions.

1.2 2219 Clad ETR Fuel Elements (R. R. Hobbins, M. F. Marchbanks, M. J. Graber)

The investigation of 2219 aluminum alloy for use as a fuel cladding material continues. This alloy was originally developed for elevated temperature applications and possesses a higher yield strength than any other commercially available aluminum alloy in the temperature range 250 to 350°C.

Three full-sized fuel elements clad with 2219 alloy have been irradiated in the ETR. No unusual problems were encountered in the operation of the reactor which could be attributed to these elements. During Cycle 97, elements E-623-E and E-625-E were located in core positions M10 and K7 corresponding to 2.08 and 1.86% total core power, respectively. Using the simplifying assumption that the neutron flux distribution does not vary with time, the average burnups were calculated to be 28% for E-623-E and 25% for E-625-E. In Cycle 99, 2219-clad element E-626-E was placed in the J9 core position corresponding to 2.32% of the total core power and resulting in a calculated average burnup of 33%.

Since 2219 contains 6.3 wt% copper, chemical analyses were performed to determine the effect of 2219 alloy clad elements on the copper content of the ETR primary coolant water. In the absence of 2219 clad elements, the copper content of the primary water is 2.0 ± 0.4 parts per billion. During Cycle 97 the average of analyses taken on three separate days was 3.2 ± 0.3 ppb copper. Two analyses from Cycle 99 show an average of 1.9 ± 0.4 ppb copper. These results indicate that the effect of 2219 clad elements on the concentration of copper in the ETR primary coolant is not significant.

After removal from the reactor, the elements were examined in the ETR canal and found to be sound. The water channels were probed and found to be nearly unchanged from the preirradiation dimensions. No unusual surface conditions were detectable.

Elements E-623-E and E-626-E have been transferred to the hot cells. The side plates have been removed, and the individual fuel plates have been visually inspected, dimensioned, and photographed. Further examinations of the fuel plates, which are scheduled to be performed in the hot cells, include gamma scanning, corrosion thickness measurements, density and thickness determinations both before and after stripping the corrosion coating, blister testing, metallographic examination, and compression testing at room and elevated temperatures. The results of these examinations will be included in a topical report now in progress on the use of 2219 aluminum alloy as a fuel cladding material.

2. IRRADIATION TESTING

2.1 Sample Irradiation

2.11 PAED G-12 Irradiation Facility and Program (E. H. Porter, G. W. Gibson, M. Hatch). During FY-1969, the PAED-59 G-12 irradiation facility in the Engineering Test Reactor (ETR) was operated for three ETR Cycles (99, 100, and 102) by the Branch for the irradiation testing of reactor fuels and materials with the facility being shared with the Metals and Ceramics Division of Oak Ridge National Laboratory (ORNL). This organization provided about one-third of the samples.

The G-12 loop is a high flux pressurized water loop located near the SW corner (G-12 position) of the ETR core. During the year, the loop was operated in the "feed and bleed" mode of operation. In this method of operation, the bulk

coolant enters the loop from the ETR primary coolant stream, is pressurized, and pumped through the sample assembly. The coolant is heated by the sample fuel plates. After passing through the sample train, the coolant flow is split, with the major portion recirculated through the loop, and the balance returned to the ETR primary coolant return line. By varying the amount of bypass flow through a heat exchanger, the required bulk coolant temperature is achieved. The G-12 loop operating conditions for the three cycles are shown in Table II-9.

TABLE II-9

G-12 LOOP OPERATING CONDITIONS FOR CYCLES 99, 100, and 102

Inlet water temperature	71°C
Inlet pressure	760 psig
P (core)	64.8 psi
Main loop flow rate	96.5 gal/min
Pressurizing flow rate	15 ± 5 gal/min
pH	5.0 ± 0.2

The G-12 sample assembly contains space for 24 sample plates measuring 1.25 by 5.75 inches. These are situated in six tiers of four plates each. Each tier provides for a 0.150-inch-thick plate which may be fueled and instrumented with thermocouples to measure fuel plate center-line temperatures. In addition, each tier contains three 0.050-inch-thick samples. The plates are separated by 0.100-inch-wide flow channels.

Table II-10 gives information of the Idaho Nuclear samples which were irradiated in the loop during the year. It should be noted that the samples which are indicated in this table as having been exposed in ETR Cycles 99 and 100 were also tested for a short time in Cycle 102. The total exposure on the Cycles 99 and 100 sample train was 9995 MWd's. The 102 sample train was operated for 4331 MWd's.

2.12 Capsule Irradiations (M. J. Graber). Bulk fuel UAl_x capsule irradiations were continued during the year in the MTR. Nine capsules reached the required irradiation level before irradiations were discontinued. Two more capsules, which were removed from the MTR, will be inserted in the ETR to complete the required exposure. Ten additional capsules in various stages of fabrication will be irradiated next fiscal year as fabrication is completed.

2.2 Postirradiation Examination

2.21 G-12 Loop Samples (M. J. Graber). Postirradiation examination work on about 150 sample fuel plates was started during the latter part of the year. These samples had been irradiated during FY-1967 and -1968 but hot cell examinations had been postponed due to a shortage of funds in FY-1968.

Some of the G-12 sample fuel plate blister data from composition I-30 have been finalized. Composition I-30 is 26 wt% UAl_3 in stainless steel which was fabricated in our laboratory. Since the fuel volume fraction, 0.293, is

TABLE II-10

TEST OBJECTIVES FOR IDAHO NUCLEAR CORPORATION G-12 IRRADIATIONS IN CYCLES ETR 99, 100, AND 102

Experiment Number	ETR Cycle Number	Sample Number	Objective of Test
69-1	102 102 102	I-48-1438 I-48-1444 I-48-1451	The irradiation testing of uranium-silicon-aluminum alloys to high fission densities is being done in order to provide data that will allow the use of elements with this type fuel to be used to higher burnup than now permitted.
69-4	102 102 102	I-11-1848 I-11-1849 I-11-1850	The testing of fluidized-bed-produced UAl_x is being undertaken as there appears to be an economic incentive in the use of this material.
69-5	99,100 99,100 99,100	I-51-1522 I-51-1524 I-51-1526	The testing of boron glass tagged with Co-60 in plates fueled with UAl_x powder will be undertaken to demonstrate the feasibility of using this material for a controllable neutron absorber.
69-7	102 102 102	I-82-1844 I-82-1845 I-82-1846	This experiment is to study the use of $U(AlSi)_3$ fuel powders as it is believed there may be some advantage in the fabrication and irradiation stability in using this fuel compound.
69-8	102 102	I-74-1779 I-77-1790	The use of B_4C + Al and B glass + Al foils are being investigated for possible ATR application.
69-9	99,100 99,100 99,100 99,100 99,100 99,100	I-69-1579 I-69-1580 I-70-1583 I-70-1584 I-71-1593 I-71-1594	The irradiation performance of UAl_x powder will be studied to burnups of up to 2 x 10^{21} fissions/cc at three loadings: (1) 60 wt% UAl_x (2) 65 wt% UAl_x (3) 77 wt% UAl_x The grams of fuel per sample will be kept constant and the core thickness will vary.
69-10	99,100 99,100 99,100	I-23-1294 I-23-1296 0-56-957	The long-term irradiation effects will be studied on plates containing high wt% of UAl_x and U_3O_8.
69-12	102 102 102	I-1-1800[a] I-1-1811[a] I-1-1826[a]	The irradiation performance of UAl_x fuel powder with 10, 33, and 50% fines (-325 mesh) is being determined.
69-13	99,100 99,100 102 99,100 99,100	I-61-1714 I-61-1715 I-61-1717 I-61-1718 I-61-1719	The effect of surface defects on cladding corrosion will be studied on thick fuel plates (0.0150 inch). This will be done with view of relaxing the specifications for surface conditions on ATR plates 1 and 19. Both chemically cleaned and sanded surfaces are being used.
69-13	102	I-61-1717	The effect of surface defects on cladding corrosion is being studied on thick plates (0.150 inch).
69-14	102 102 102 102	P-2-741 I-1-1800[a] I-1-1811[a] I-1-1826[a]	The use of a chemical pretreatment of fuel plate surfaces is being investigated. It is believed that treatment which produces a Bayerite coating will reduce the oxide film formation rates on aluminum clad fuel plates.

[a] Dual experiment.

NOTE: The I-51 series samples for experiment 69-5 are clad with 2219 aluminum. All others are clad with 6061 aluminum.

very similar to the UO_2 stainless steel, 0.278, reported in ORNL-3709 [2] and the percent theoretical density of all the samples is 93 to 95, a direct performance comparison to UO_2 dispersions can be made. Both of these materials are producing plate blistering below the temperature of rapid gas release from the samples -- 900°C for UO_2 and 1250°C for UAl_3. The three remaining forces which could contribute to blistering are (a) the buildup of solid fission products, (b) recoil gas release as a function of fission rate (but not temperature), and (c) gas agglomeration in bubbles. It has previously been shown that UO_2, whether dispersed in stainless steel or in aluminum, develops numerous gas bubbles which grow with increased fission density. Such bubble agglomeration has not been observed in UAl_x-Al dispersions and only to a minor degree in UAl_3-SS dispersions.

The recoil zone surface area in these stainless steel dispersions would be similar, so the amount of recoil gas would be expected to be similar. As shown in IN-1131 [3], the solid-fission-product induced growth rates are similar. It is therefore deduced that the major performance difference between the UO_2 and the UAl_3 is the relative amounts of gas bubble agglomeration. Blister temperatures obtained on the two fuel systems are given in Table II-11.

TABLE II-11

BLISTER TEMPERATURES FOR UAl_3-SS AND UO_2-SS FUELS

Fissions/cc of Core x 10^{-20}	UAl_3-SS Blister Temperature (°C)	UO_2-SS Blister Temperature (°C)
7.0	930	730
10.3	820	650
12.6	870	570
13.7	820	550
18.6	760	470
20.5	760	470

It was originally believed that the good blister resistance of aluminum clad plates fueled with uranium aluminide was due to the formation of the stable compound UAl_4. These results show that even when no excess aluminum is present with which to form UAl_4, UAl_3 still has good blister resistance.

2.22 Limitations of Roll Bonding (M. J. Graber, G. O. Hayner, B. G. Carlson). It is possible through qualified procedures to produce metallurgical bonding (grain growth across the interface) by the conventional roll bonding picture-frame fabrication technique. The reliability of the fuel plates depends on the ability of the fabricator to repeat the qualified procedure consistently. If the fabricator's deviation from qualified procedures is severe enough to produce heterogeneous nonbonds, detection can be made by nondestructive means, blister testing for the nonbonds which contain entrapped gas and ultrasonic examination for those without gas. However, it is conceivable

that partially bonded or "semibonded" plates could be produced inadvertently by the fabricator which could pass the nondestructive tests, but would not have sufficient blister resistance for reactor use. By experimental rolling procedures, semibonded fuel plates of this type have been produced, examined destructively and nondestructively, irradiated, and evaluated. Those "semibonds" with marginal irradiation performance have been compared by destructive examination with ATR plates fabricated by commercial vendors, Figures II-8 and -9. Specifically, these bonds were compared by metallography and bend testing to test plates which achieved burnups of 9×10^{20} to 11×10^{20} fissions/cc before blister failure. These test plates had 6061 aluminum alloy claddings and were fueled with UAl_x to the nominal loading required in the ATR. The comparative destructive examination showed that both the vendors' plates had a greater degree of bonding than the marginal experimental plates and are therefore acceptable.

When a metal is worked above its strain recrystallization temperature, about 150°C minimum for aluminum, it will tend to recrystallize spontaneously as soon as it is deformed mechanically and the grains will grow to the equilibrium size for that temperature. The strain energy induced by the large reduction per pass during hot rolling in the standard rolling procedure would promote this recrystallization and grain growth. The 15% cold working followed by annealing used in the final stages of the standard G-12 procedure also promotes the growth of grains across the interfaces.

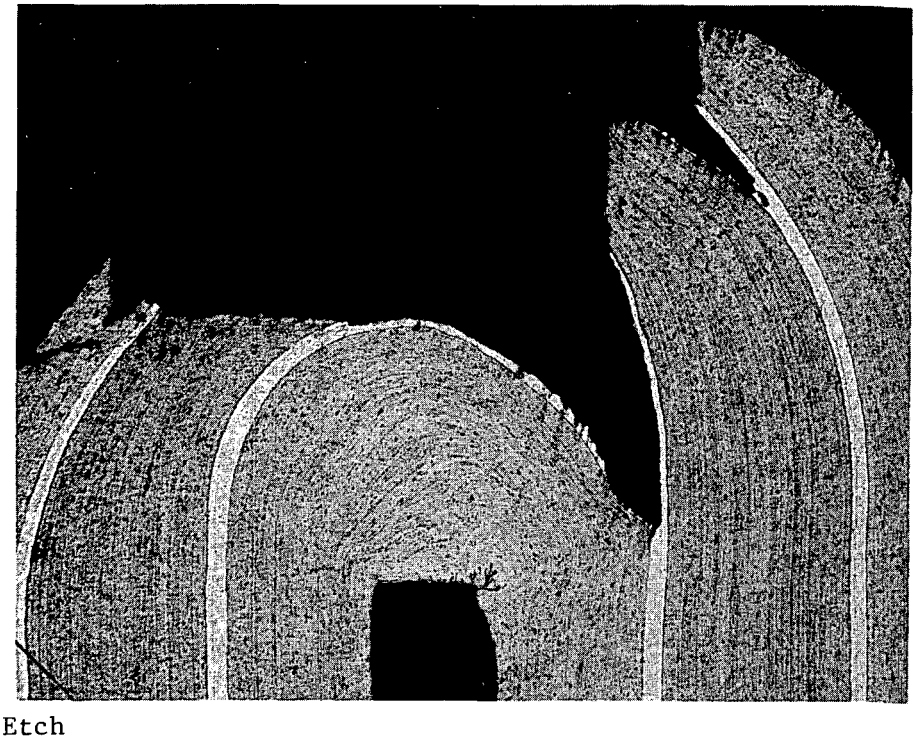

Etch

Fig. II-8 Photomicrograph of marginal plate after a 180-degree bend test was performed. Note the failure of the outside clad and the delamination of the bond interfaces.

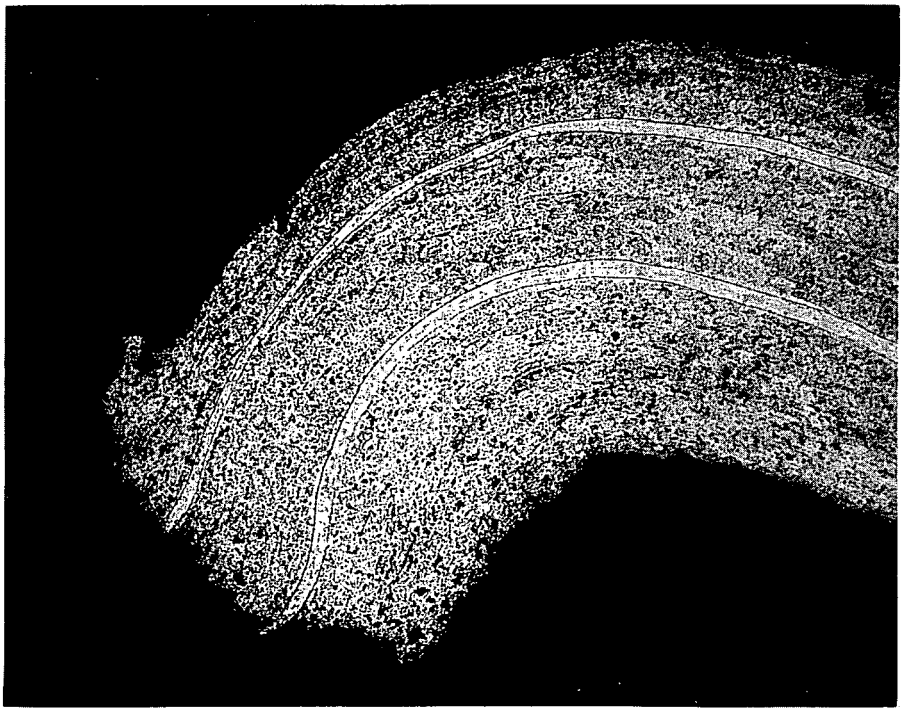

Etch

Fig. II-9 Photomicrograph of a typical vendor plate after 180- and 270-degree bend tests were performed. Note that delamination did not occur in this test.

The variables to consider in roll bonding are:

(1) Rolling temperature

(2) Atmosphere

(3) Diameter of the rolls

(4) Speed of the rolls

(5) Reduction per pass

(6) Total reduction

(7) Amount of cold reduction

(8) Surface preparation.

Since nondestructive testing, as presently used, does not reveal semibonds, it is necessary to qualify rolling schedules by destructive examination. The bend testing and metallography on these samples indicate the limits of acceptability to be about 180 degrees free bend without bond failure and 50% grain growth across the interface. The reliability of the fuel plate, with regard to semibonds, depends on the ability of the fabricator to repeat the qualified procedure consistently.

2.23 Blister Mechanisms in Dispersion Fuels (M. J. Graber, C. E. May). It has been known for some time that the blister resistance of a dispersion

fuel plate depends on what fuel material is dispersed. For instance, the latest reporting of blister resistance data [3] shows again that a UO_2 dispersion in aluminum, at a given irradiation level, blisters at a lower temperature than a UAl_x dispersion.

Metallographic examination of blister samples show that blister cracks initiate in the UO_2 fuel particles and progress to the matrix, Figure II-10.

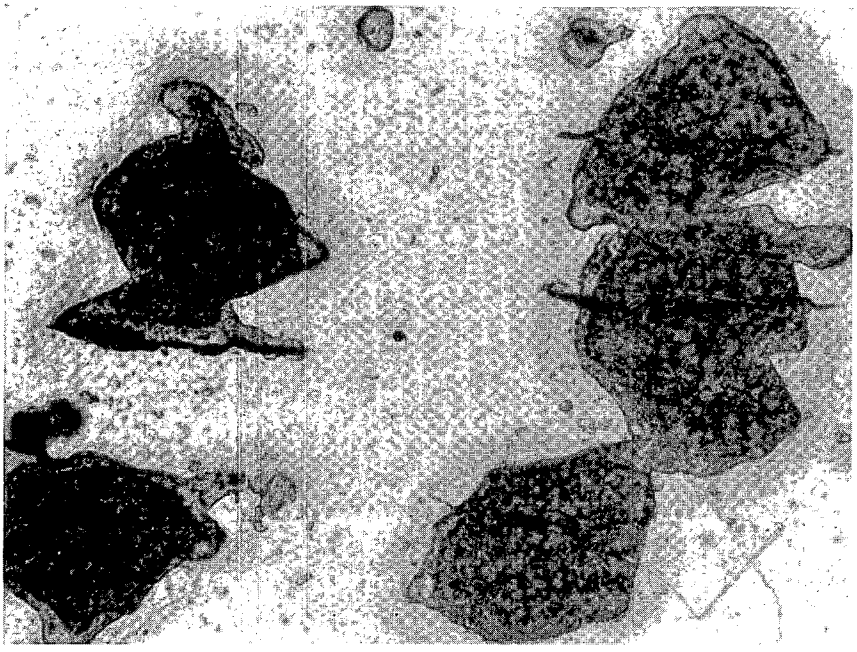

As-polished 25% burnup 500X

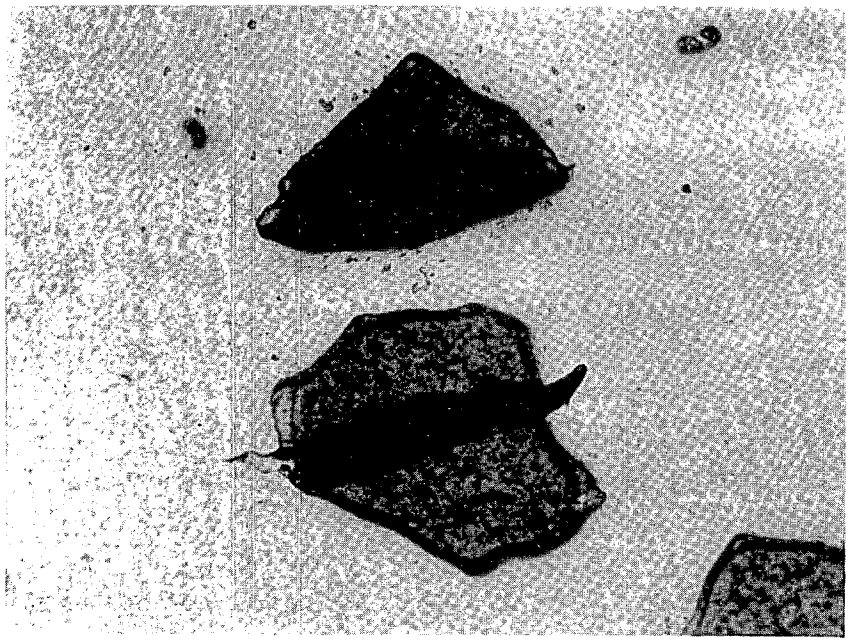

As-polished 35% burnup 500X

Fig. II-10 Irradiated UO_2 dispersed in aluminum. Cracks initiate in the fuel particles below 300°C.

This is understandable because, as was shown previously[2], gas bubbles agglomerate within the UO_2 particles. Gas bubble agglomeration of this type had not been found in the UAl_x fuel particles. Yet, if an irradiated UAl_x plate is heated to high enough temperatures, blistering does finally take place. As shown in Figure II-11, when these blisters do occur, they initiate by matrix cracking.

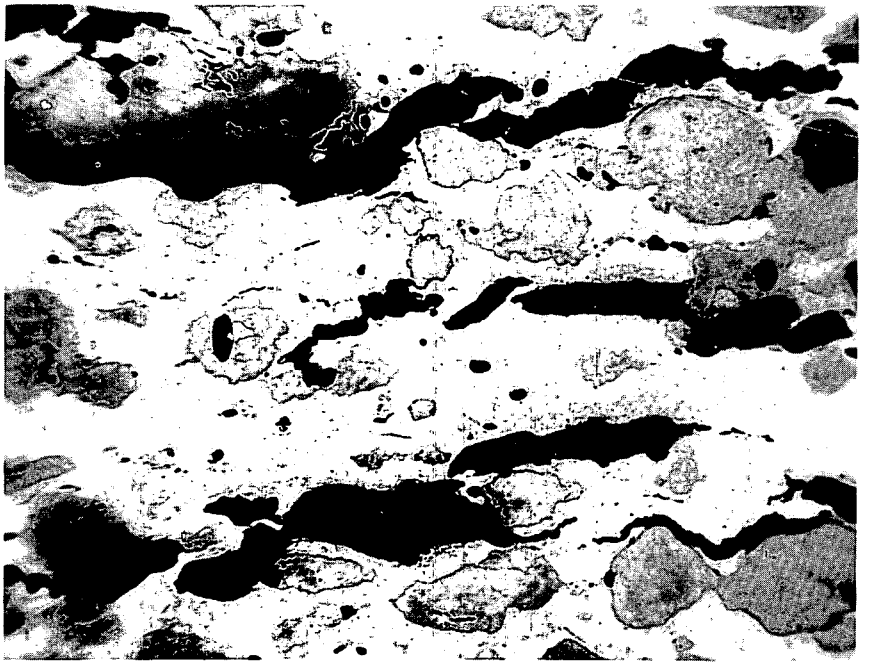

As-polished | 40% burnup (10.7 x 10^{20} fissions/cc) | 200X

Fig. II-11 Irradiated UAl_x dispersed in aluminum. Cracks initiate in the matrix at 480°C.

Because optical magnification to 1000X does not show the cause of matrix cracking, a series of samples were examined on the electron microscope. Even at 15000X, bubble agglomeration was not found in the fuel particles; however, it was possible to resolve bubbles in the aluminum matrix, Figure II-12. Since the bubble radius "r" is $\approx 2.8 \times 10^{-6}$ cm and the surface tension of aluminum γ is $\approx$914 dynes/cm, the pressure in the bubble "p", if filled with fission gas (in equilibrium with the surface tension), by $p = \frac{2\gamma}{r}$ is equal to 645 atmospheres. According to the Beattie-Bridgeman plot in Figure II-13, the gas at these conditions would occupy $\approx$2.5 times the volume occupied in the interstitial, substitutional, or solid form, indicating fission recoil gas could have produced kinetic growth in these bubbles at the recoil zone.

Figure II-14 shows another sample with fewer matrix bubbles and a lower irradiation level. Figure II-15, a sample with higher irradiation, also showed fewer bubbles after blister testing to 480°C. It is postulated that bubbles in the matrix tend to migrate to the crack surfaces at elevated temperature causing the blister to grow. Aluminum has a fairly large recoil zone. The volume percent of bubbles as observed in the recoil zone is quite large, and if projected over the entire matrix would not agree with the observed growth rates by a factor of $\approx$4. This could mean that the undisturbed bubbles might

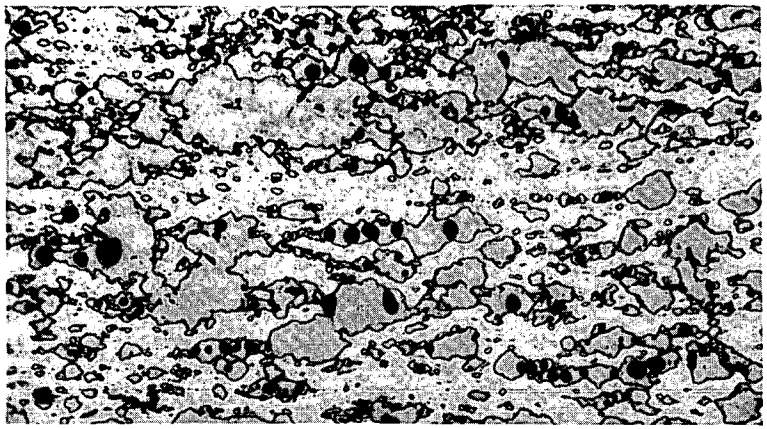

200X Optical

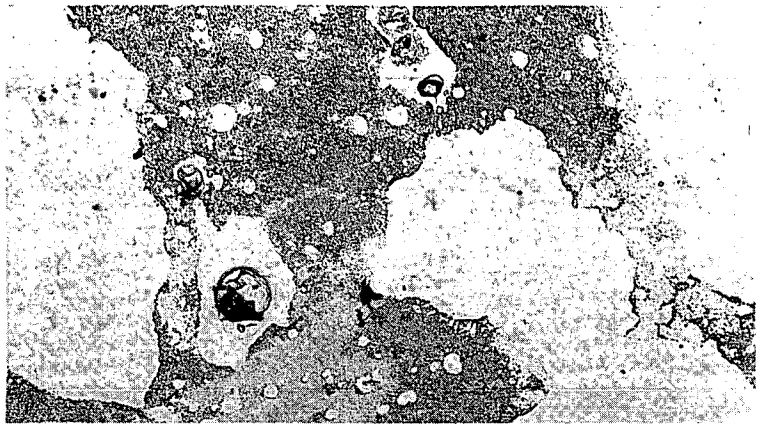

3200X Electron Microscope

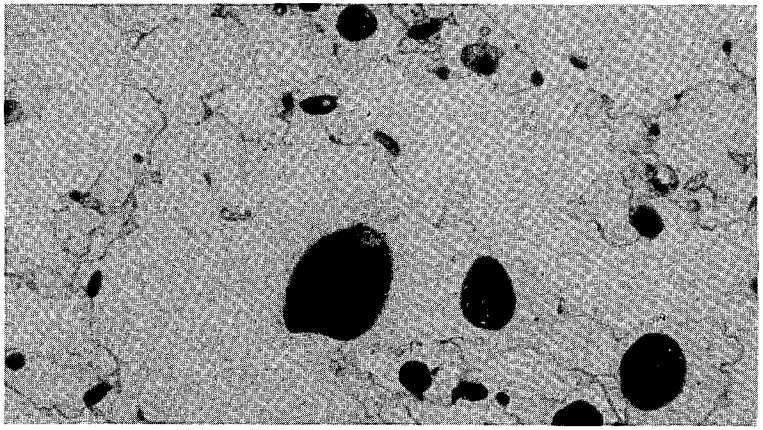

1000X Optical

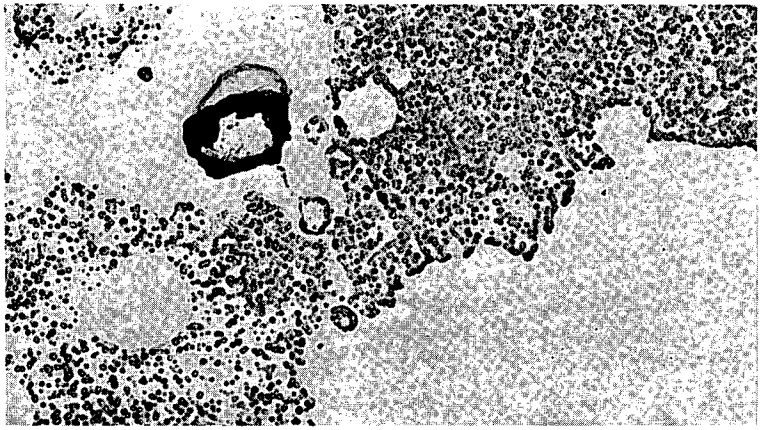

15000X Electron Microscope

Fig. II-12 As-irradiated UAl_x (4.6×10^{20} fissions/cc) dispersed in aluminum (plate P-1-720, MT 443) at various magnifications from 200 to 15000X, showing bubbles in the aluminum matrix.

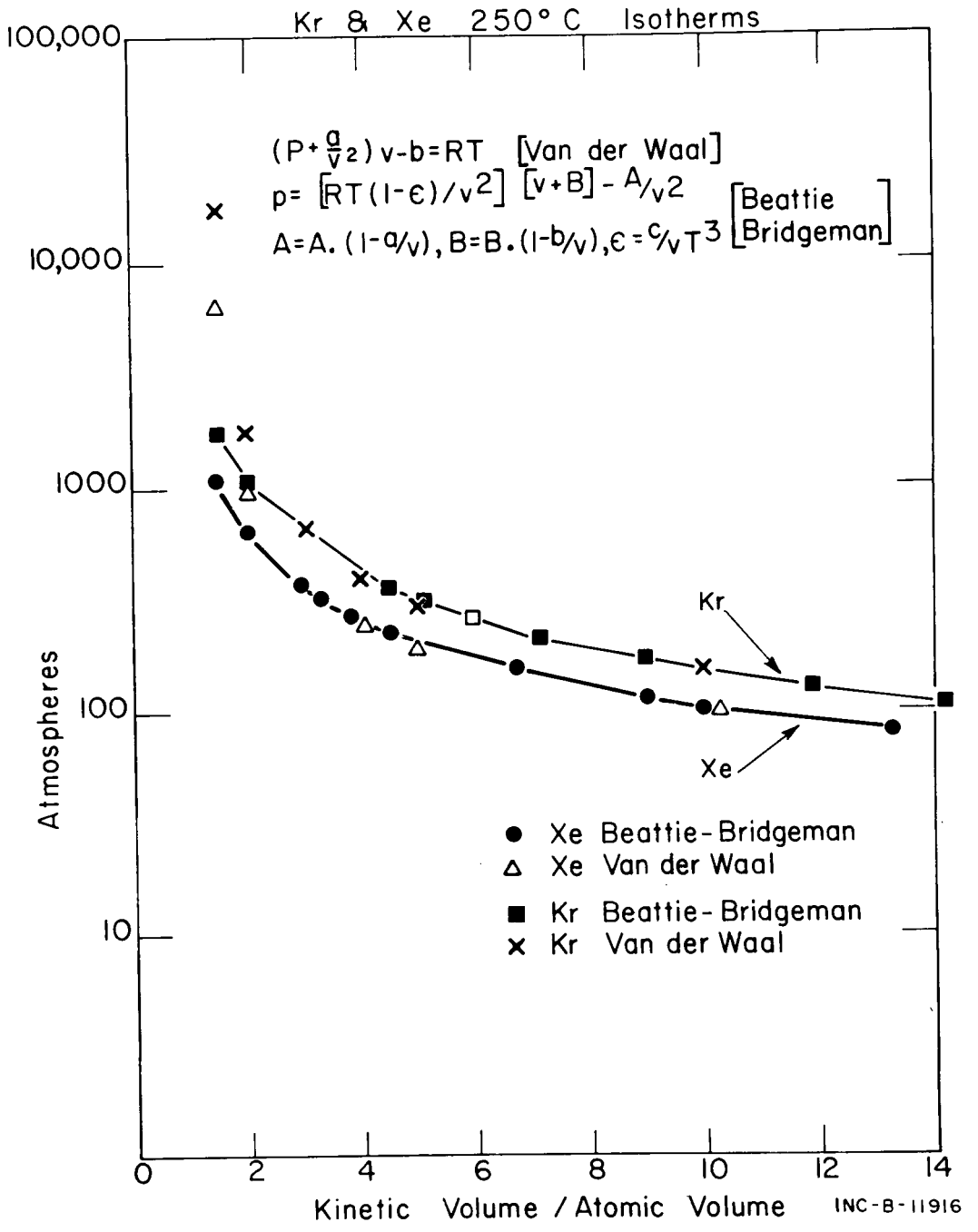

Fig. II-13 The 250°C pressure volume isotherm for krypton and xenon with the gas volume expressed as the number of times it exceeds its own atomic volume.

200X Optical

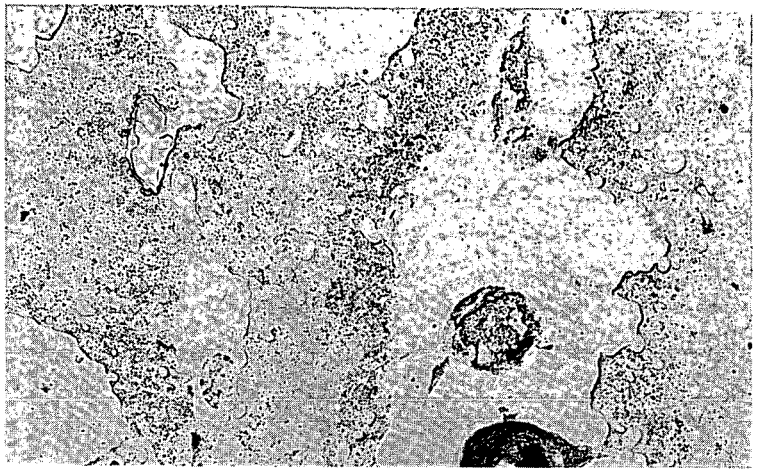

3200X Electron Microscope

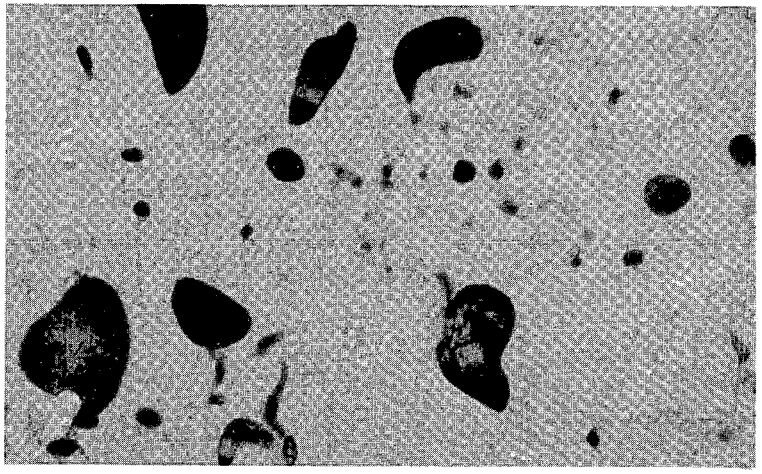

1000X Optical

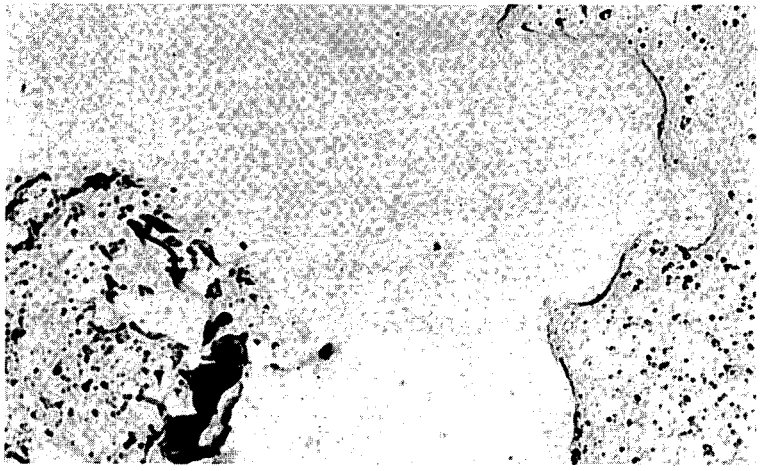

15000X Electron Microscope

Fig. II-14 As-irradiated UAl_3 (2.6×10^{20} fissions/cc) dispersed in aluminum (plate P-1-719, MT 446) at various magnifications from 200 to 15000X, showing the beginning of bubble formation in the aluminum matrix.

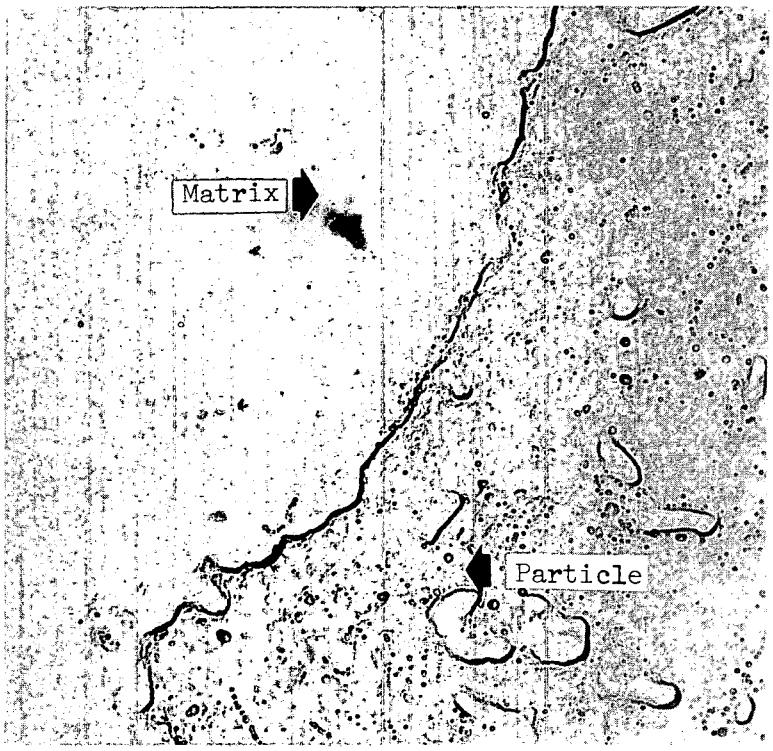

Fig. II-15 Particle and matrix at 15000X of UAl_x sample irradiated to 1.9×10^{20} fissions/cc and blister tested. Heating at blister temperature (480°C) causes the bubbles in the matrix to diminish.

actually be smaller, the gas pressure high, and the gas volume more nearly equal to its solid volume. Bubble enlargement may come at the time of polishing due to the high pressure.

It appears that blister failure of the UAl_x dispersions is caused by fission recoil gas rather than gas entrapped in the fuel particles. The gas retention potential of the fuel particles themselves appears not to have been exceeded. Further improvement in blister resistance would come from selecting a matrix material with a shorter recoil zone or a higher surface tension.

2.24 Bulk UAl_x Fuel Irradiations (M. J. Graber, G. W. Gibson). Previous fuel development work on the uranium-aluminum dispersion fuel system has consistently shown excellent resistance of the UAl_x compounds to fission gas agglomeration[4]. But the basic fuel stability parameters of the individual intermetallic compounds could not be studied in a dispersion system because an excess of aluminum tends to convert the higher uranium compounds to UAl_4, and the temperature of such studies is limited by the melting point of the UAl eutectic and of aluminum itself. Therefore a limited capsule program has been initiated to irradiate the UAl intermetallic compounds as bulk (powder and pellet) materials.

The intermetallic compounds were produced by reacting uranium-hydride and aluminum[5]. The finely divided uranium-aluminide powders approached theoretical density if hot-pressed at 4500 psi and at 80% of the melting point. Reductions in temperature and/or pressure have been used to decrease and

control the density. The dense UAl_3 material attained a 34,000 psi compression strength and was thermally stable as determined by X-ray diffraction before and after a 258-hour exposure at 1000°C.

The capsule irradiation program, which currently is in various stages of scheduling, fabrication, irradiation, examination, and evaluation, is designed to study the effects of temperature, burnup, fuel compound, density, and reaction rate with various possible container materials. The irradiation of 18 of these capsules has been completed and 13 have undergone partial postirradiation examination. These capsules were irradiated in the MTR and ETR in thermal neutron fluxes ranging from 1.5×10^{14} n/cm^2-sec to 3.3×10^{14} n/cm^2-sec and to ≈60% U-235 burnup. The postirradiation examination procedure includes weighing, dimensioning, gas collection, density, mechanical testing, burnup analysis, and metallography. Table II-12 lists the condensed capsule irradiation and observation data. The UAl_3 samples showed no structural change during irradiation and did not release a significant amount of fission gas as a function of irradiation. The UAl_4 compound which did reach an incipient fusion stage during irradiation also did not release appreciable amounts of fission gas.

TABLE II-12

FISSION GAS RELEASE IN BULK UAl_x COMPARED TO BULK UO_2

Capsule Number	Fuel Compound	Helium Gas Annulus Mils	Fissions Per Capsule Per Second x 10^{14}	Heat Generation kW/ft	% Krypton + Xenon Released	Sample Condition After Irradiation
2	UAl_3	1.5	2.1	23	0.003	No change
3	UAl_4	1.5	2.4	26	3.000	Center incipient fusion
4	UAl_3	2	2.0	24	0.08	No change
5	UAl_4	2	2.3	23	0.30	Center incipient fusion
14	UO_2	1	1.9	20	32.0	Central void Columnar Grain Growth
16	UO_2	2	2.0	21	50.0	Central void Columnar Grain Growth
18	UO_2	3	2.3	25	48.0	Central void Columnar Grain Growth

Since considerable testing has been done on UO_2 and much is known of its properties, UO_2 irradiations were performed in the same type capsules as the bulk UAl_x so that UO_2 fuel could be used as a standard for comparison.

This information also is shown in Table II-12 and compared to the aluminide data. It is seen that the UO_2 capsules release between 30 and 50% of the fission gas produced while UAl_3 releases 0.08% or less at similar heat generation rates.

In addition to melting point and gas release threshold temperatures, the heat dissipation ability of a fuel material depends on thermal conductivity. For instance, a material with a high thermal conductivity and relatively low melting point may actually have better heat dissipation ability than a material with a very high melting point but poor conductivity. The metallography of these materials (UAl_3 and UO_2), Figure II-16, shows the typical central hole and columnar grain growth in the UO_2 while the UAl_3 structure remains unaltered. The higher thermal conductivity of the UAl_3 apparently more than compensates for its lower melting point.

Postirradiation anneal tests to determine the release of noble gas and long-lived fission products (primarily Cs-137, Ru-106, and Sb-125) from bulk uranium-aluminide fuel specimens are being conducted by the Analytical Chemistry and Chemical Technology Branches. The releases are determined by heating the fuel specimen to progressively higher temperatures and collecting quantitatively the fission products released. To date, four tests have been completed -- two on UAl_4 and two on UAl_3 fuel specimens. Preliminary results indicate that the major noble gas and cesium releases occur near the uranium-aluminide peritectic reaction temperature (1350°C for UAl_3 and 730°C for UAl_4). Smaller releases occurred at temperatures slightly below and above the peritectic temperatures, both on heating and cooling the specimens. Releases of antimony and ruthenium occurred well below the peritectic temperatures. The magnitude of the noble gas and long-lived fission product releases has not yet been determined. Additional tests will be conducted on UAl_3, UAl_4, UAl alloy, and UO_2 fuel specimens.

2.25 Characterization of the Reactor Performance of Sample Fuel Plates with MTR, ETR, and ATR Conditions (M. F. Marchbanks, W. C. Francis, M. L. Griebenow). The history of the irradiation performance of sample fuel plates of MTR, ETR, and ATR compositions has been compiled and is summarized in the graphs shown in Figures II-17 and -18. The data from which the graphs were plotted are referenced on the graphs. Some blister data from actual fuel plates was used to make the failure-nonfailure lines.

Figure II-17 shows the irradiation swelling performance of MTR, ETR, and ATR compositions as determined by the plates examined to date. The plots of plates containing powdered fuel are considered qualitative in nature as the effect of difference in original void content has been averaged for each composition. The maximum nominal burnup for the various reactor loadings is indicated on the graph as a guide to acceptable performance for the plates. In all cases for each reactor application, the plots show swelling well below the critical swelling value of 7%.

Figure II-18 shows the blister resistance performance of MTR, ETR, and ATR plate compositions. The maximum nominal temperatures (the most probable maximums) at the maximum nominal burnup for each reactor are indicated on the plot. In addition, the hot spot - hot channel maximums are also

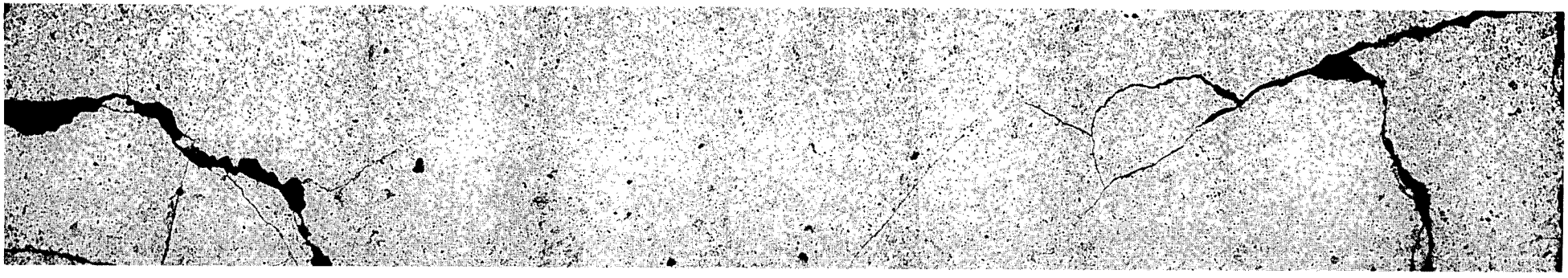

As-polished UAl_3 irradiated at 23 kW/ft 16X

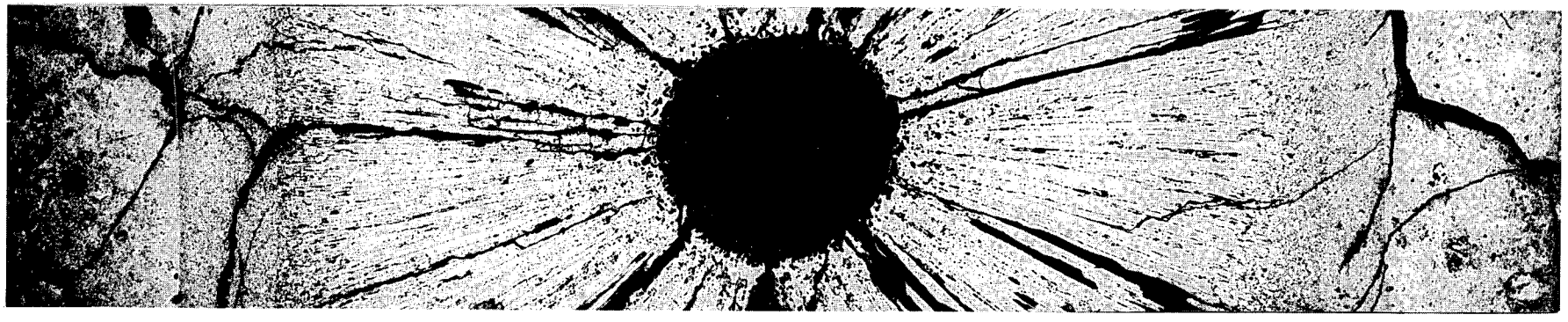

As-polished UO_2 irradiated at 21 kW/ft 16X

Fig. II-16 UAl_3 and UO_2 irradiated in similar capsule designs and at similar heat generation rates.

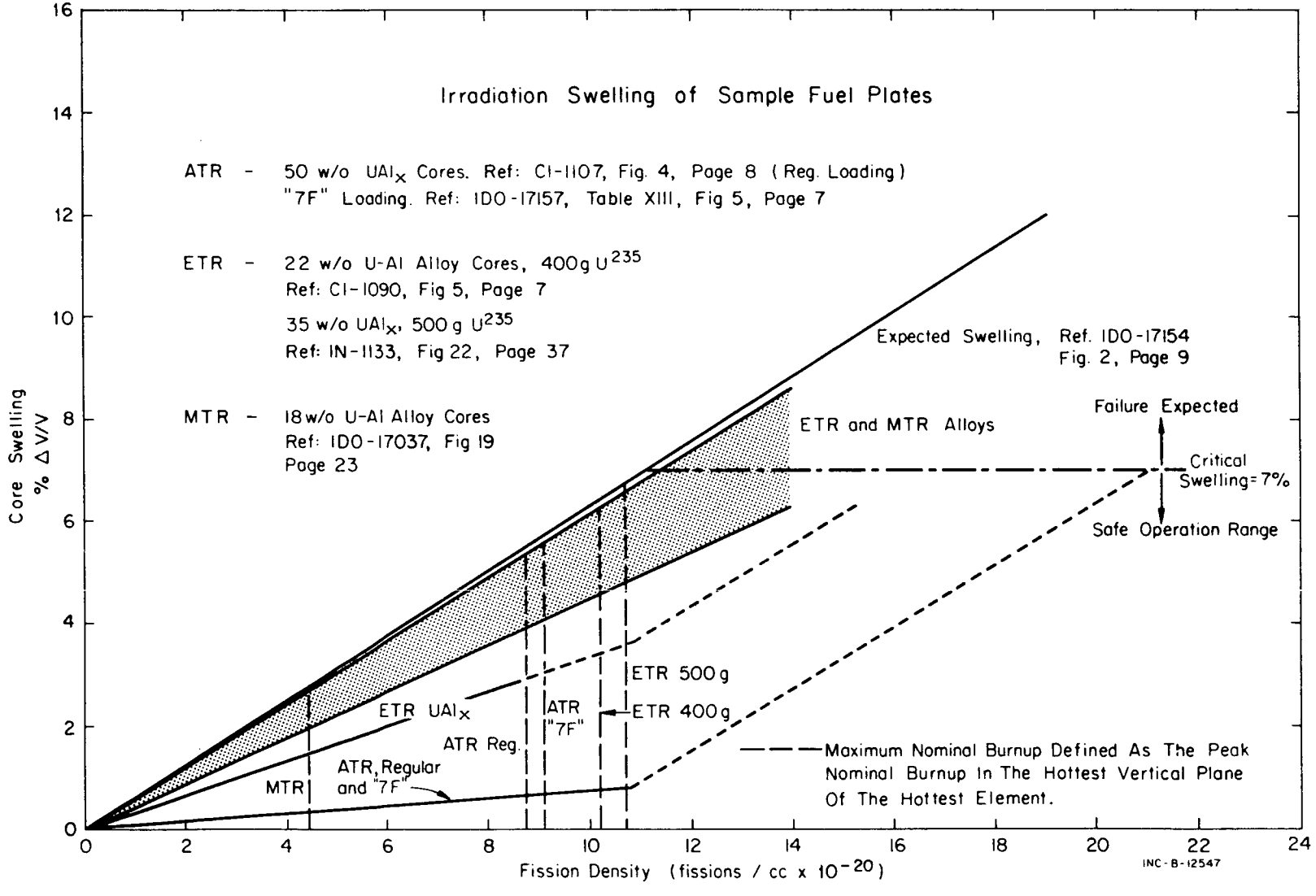

Fig. II-17 Irradiation swelling of sample fuel plates.

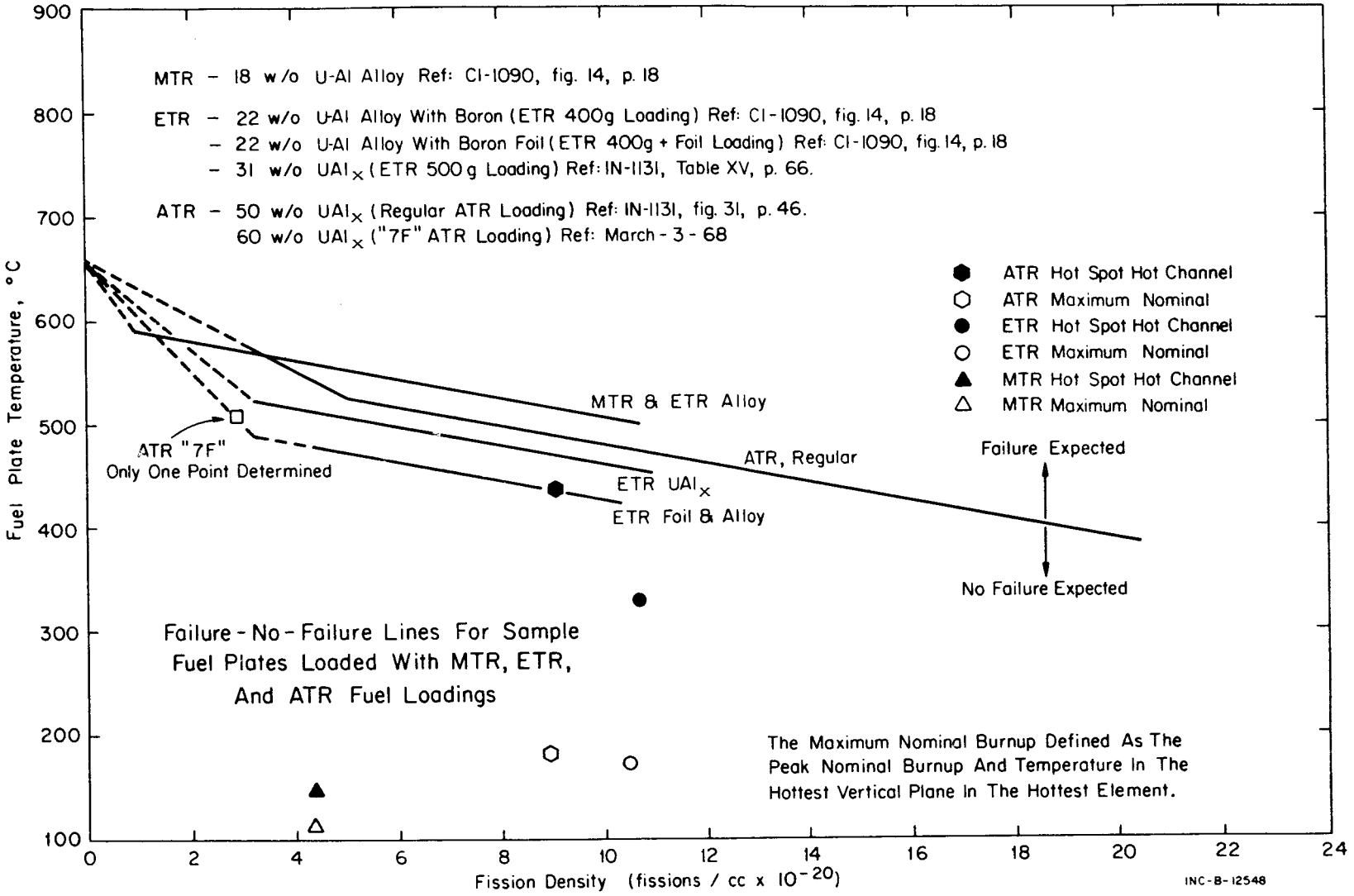

Fig. II-18 Failure-no-failure lines for sample fuel plates loaded with MTR, ETR, and ATR fuel loadings.

indicated. The plots show sufficient blister resistance for the most severe operating conditions (the hot spot channel maximums) for all reactor compositions.

3. METALLURGICAL DEVELOPMENT

3.1 Assay of Boron in Test Reactor Fuel Elements (G. W. Gibson, B. G. Carlson)

In the annual report for FY-1968, the use of Co-60 tagged boron for the assaying of boron in aluminum clad fuel plates was discussed [6].

To develop the scanning procedures, a series of prototype fuel plates were made in which the boron was added as Co-60 tagged boron glass. Ten plates were made measuring 25 x 3 x 0.050 inches. These plates were clad with 1100 aluminum alloy. Five of the plates were fueled with fully enriched UO_2 and five were made with fully enriched UAl_x powder. A heterogenous fuel dispersion was obtained in plates containing UO_2 while those containing UAl_x powder had a homogenous dispersion.

These plates were scanned by the Nuclear Technology Branch using gamma-ray spectrometry with both the boron and U-235 content being determined. The people doing the scanning were not told the amounts of U-235 or boron the plates contained (as determined by the chemistry and weights of the powders) until after the values from scanning had been established. The results of this test are given in Table II-13.

The estimated uncertainties on boron assay are about 10%. The estimated uncertainties on uranium assay are about 3%. The cause of the difficulties in plate Co-60-5-1 are unknown at present. It is believed that in spite of this one outlier these results demonstrate the reliability of the technique.

In making the sample and prototype plates, addition of a radioactive glass to the fuel mixture did not present any complications in fabrication, nor was there a large increase in activity from the finished plates which contained the cobalt versus control plates without cobalt. A small increase in activity in the more heavily loaded plates was detected but was not enough to interfere with a well run fuel fabrication shop.

To ensure that Co-60 was uniformly distributed with the boron in the boro-silicate glass, a refinement of the blending procedure has been made.

Formerly, the Co-60 was added after the glass had been made, necessitating remelting of the glass to obtain a homogenous mixture of the cobalt. Results from this method were acceptable but further assurance of a uniform Co-60 to boron ratio was desired.

In the newly developed technique, Co-60 in the form of an aqueous solution of $CoCl_2$ is added to the boric acid powder. This mixture is blended until random samples show that within the accuracy of the counting equipment the Co-60 activity is uniform.

TABLE II-13

COMPARISON OF BORON AND U-235 RESULTS OBTAINED BY TWO METHODS ON TEN PROTOTYPE FUEL PLATES

Plate Number	Boron Content (mg)		Uranium Content (g)	
	γScan Assay	Chemical Content	γScan Assay	Chemical Content
		UO_2 Fuel		
Co-60-1-1	62.4	61.4	14.3	14.21
Co-60-2-1	91.5	94.2	13.7	13.41
Co-60-3-1	131.9	130.9	18.8	18.96
Co-60-4-1	144.8	144.5	18.4	18.11
Co-60-5-1	86.9	78.3	13.7	13.78
		UAl_x Fuel		
Co-60-1-2	62.0	61.7	14.7	14.22
Co-60-2-2	91.8	94.2	13.6	13.41
Co-60-3-2	128.6	130.7	19.0	18.95
Co-60-4-2	139.1	144.6	18.3	18.15
Co-60-5-2	81.3	78.4	13.9	13.80

This material is dry blended with the other constituents and melted. Activity of this melt is counted and must be uniform within the capability of the counting instrument.

A variety of sizing methods has been tested for reducing the glass to a -200 + 325 mesh. Dry rod milling produced almost 100% fines (-325 mesh), as did the use of a Spex "Mixer-Mill". A more successful technique was to change the screen on the hammer mill, used for grinding fuel. It was possible to reduce 90% of the glass to the desired size (-200 + 325 mesh) with this method. The screen used in the hammer mill has 0.0625 inch openings spaced about 0.110 inch center to center.

As indicated in a previous section of this report, a number of samples containing the cobalt-boro-silicate glass were under test at the end of the fiscal year.

Negotiations were undertaken with the current vendor of ETR fuel elements to obtain 10 elements in which the B_4C powder would be replaced with Co-60 tagged boro-silicate glass. This vendor has indicated that the radioactive glass would present no major problem during the fabrication of the elements. However, he believes that the Co-60 activity could present a major problem in reprocessing the reject fuel plates.

3.2 Automatic Sample Fuel Plate Radiograph Densitometer (F. A. Meichle, R. L. Sumstine, E. G. Grafwallner, N. S. Graham, G. W. Gibson, M. F. Marchbanks)

A continuing problem in the inspection of the fuel elements for the test reactors, located at the NRTS, is the evaluation of fuel plate radiographs. The fuel plates are X-rayed and the radiograph inspected for fuel homogeneity and core location. Plates meeting the inspection requirements are fabricated into fuel elements. Fuel plates which exceed the inspection requirements may, after further examination, be used in fuel elements which are used in low power locations in the reactor core.

The evaluation consists of visual and densitometer inspection. Both are manual operations. As the number of fuel plate inspections increased, manpower availability and the possibility of errors, due to the physiological fatigue of the inspectors, indicated the need for development of a prototype densitometer to inspect the fuel plate radiographs. The prototype was designed to automatically scan a radiograph, sense the radiograph density and density location (X-Y coordinates), digitize the three signals, format and record the signals for data processing. To minimize developmental costs the prototype was designed to inspect G-12 type sample fuel plates (5.75 x 1.25 inches) radiographs and to use in-house components which were available.

The prototype densitometer evaluation will provide optical and density sensing techniques, fuel to film density correlation, data acquisition, and computer programs. A computer was not considered as part of the densitometer because of the possible number of calculations, storage requirements, and plotting graphic which can be performed on the data. The data processing facilitites are available in house.

3.21 Description. The prototype densitometer block diagram is shown in Figure II-19. The major components are the film transport, light source, light sensor, amplifier, multiplexer, controller, analog-to-digital converter (DVM), format generator, and paper tape punch.

The transport incorporates the film holder, drive motors, position transducers, and limit switches. Starting from a specified corner the transport moves the film between the light source and sensor. The film is scanned back and forth along the X-axis while incrementing along the Y-axis.

The light source beam is collimated and the light sensor positioned so that a circular area of 0.080 inch on the film is inspected. The light sensor is a SGD-100[a] photodiode chosen for its low leakage current, linearity, and stability.

The output of the photodiode is amplified and fed to the multiplexer. Two other signals (X- and Y-axis positions) are also fed to the multiplexer.

The multiplexer, driven by the controller, scans the three signals, feeding them sequentially to the digital voltmeter (DVM).

---

[a] EG and G, Electronics Products Division.

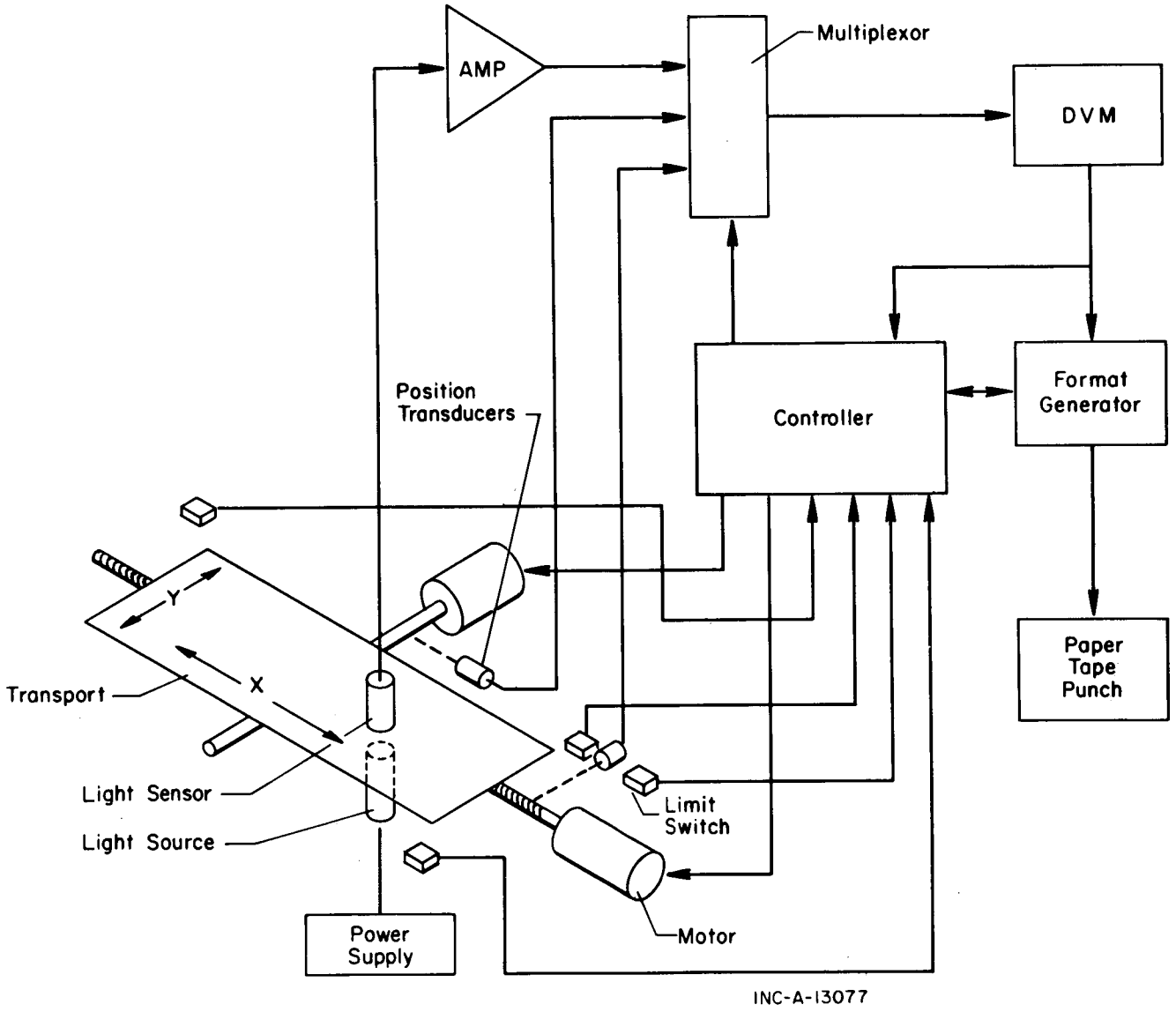

Fig. II-19 Automatic sample fuel plate densitometer.

The digital voltmeter, supplied with digital output, is used as the analog-to-digital converter. The information in the DVM is gated out in parallel to the format generator. The format generator provides the paper tape format, parallel to serial conversion, timing, and drive for the paper tape punch. Additional functions as paper tape leader and run identification are accomplished by the format generator.

The information is punched on the paper tape in the following form: X-axis position (three digits), space, Y-axis position (three digits), space, photodiode reading (three digits), double space, X-axis position, etc.

Readout intervals during a scan are accomplished by monitoring the X-axis position signal. The position signal is analog and derived from a potentiometer. Applying the X-axis position signal to the controller, the controller logic senses the number "eight" in the least significant digit. Whenever the "eight" is sensed the controller initiates a multiplexing operation. The Y-axis incrementing is accomplished in the same as the X-axis under controller control.

3.23 Production of Radiograph Standards. The production of radiograph standards was begun. A series of samples containing different fuel loadings will be made. A listing of the standards and their fuel loadings is given in Table II-14. These loadings are primarily for the purpose of proving the operation of the densitometer being developed. The basic fuel loading being used is the "nominal" loading of 401 mg U-235/in.^{2} of fuel plate core area. The other loadings are to be based on the tolerances set forth in the ATR Fuel Element Specification IN-F-3-ATR, Revision 1.

TABLE II-14

RADIOGRAPH STANDARDS

Standard Number	Purpose	Fuel Loading mg U-235/in.^{2}
0	Nominal loading	401
8	+ 8% for paragraph 3.1.2.2	433
15	+ 15% for paragraph 1.2.2	461
25	+ 25% for paragraph 3.1.2.2	501
40	+ 40% for paragraph 3.1.2.2	561
50	+ 50% for paragraph 3.1.2.1	602

3.23 Results. A computer program has been written to assemble the paper tape information into an X and Y map, plotting the densitometer readings. The program also computes the number of readings, sum, and average. The program was extended to map all values which exceed a selected percentage value above the average value. Percentage selection is under program control. Zeros replace all densitometer readings whose values are under the selected percentage.

The program is presently being extended to compute the areas and locations of the readings exceeding the selected percentages. The areas computed will then be compared with the fuel homogeneity specification for classification.

Future development will involve the following areas:

(1) X-ray exposure and developing process controls.

(2) Fuel concentration and density correlation.

(3) Decrease radiograph scanning time. Present scanning time, using one light sensor, is approximately an hour and one-half. The use of milti-light sensors and increased scanning speed can greatly reduce scanning time.

(4) Reduce the physical bulk of the recorded information. On a 1-1/4- x 5-3/4-inch sample fuel plate, the present readout contains 2280 densitometer readings. The use of magnetic tape readout can greatly reduce readout bulk.

3.3 The Development of 55 wt% UAl Alloy Powder for Use as a Nuclear Reactor Fuel Material (G. O. Hayner, K. C. Sumpter)

The objective of this study was to determine the range of uranium concentration in an aluminum clad UAl dispersion type fuel plate that will give adequate performance in the reactor and have good fabricability. The upper limit, about 72 wt% uranium, has been set to facilitate handling since the UAl alloys or intermetallic (UAl_2) are pyrophoric in this range. Currently, the ATR specifications call for 69 $\pm$ 3 wt% for the manufacture of uranium aluminide - aluminum dispersion type fuel plates used in this reactor. However, this range is based on past irradiation performance and is not the minimum uranium content as prescribed by reactor physics. This lower limit of uranium concentration is the unknown being examined with various test plates in a decreasing stepwise fashion. It is thought that some cost advantage might also be obtained through use of the lower weight percent.

It was decided that around 55 wt% uranium could be handled adequately with the laboratory equipment on hand for fabricating powder metallurgy cores. The alloy was prepared by induction melting, using a graphite crucible in a stagnant air atmosphere and quenched in argon. Table II-15 shows the recovery data.

The ingots were crushed and pulverized in a hammer mill to -100 U. S. standard mesh. After grinding, a sample was submitted for chemical, isotopic, and X-ray diffraction analysis. Typical results are shown in Table II-16.

After crushing, the UAl_x fuel powder from Heat 368 consisted of the following size distribution:

(1) 12.9% + 100 mesh (U. S. standard sieve)

(2) 60.2% -100 + 325 mesh

(3) 26.9% -325 mesh.

TABLE II-15

YIELDS OF VARIOUS UAl COMPOSITIONS AFTER INDUCTION MELTING

Heat Number	Weight Grams Uranium	Weight Grams Aluminum	Total Weight Grams	Recovery[a] %	Enrichment %
367	28.8	24.4	53.2	>100	Depleted
368	34.46	29.30	63.76	>100	92.25
369	32.8	30.1	62.9	>100	Depleted

[a] Some graphite pickup was observed on each ingot.

TABLE II-16

ANALYSIS OF HEAT 368 (ENRICHED SAMPLE)

Major crystalline constituents	UAl_4	Al
Estimated wt% of impurities	Cu	0.005
	Fe	0.04
	Mg	0.001
	Mn	0.004
	Ni	0.02
	Si	0.01
	Zr	<0.09
Isotopic Analysis	U-235	92.25
	U-234	0.63
	U-236	0.25
	U-238	6.87

Sample test plates were then fabricated from the above material for irradiation testing in the G-12 loop of the ETR. Two plates, however, were made with -325 mesh material and both were rejected on the basis of ultrasonic examination indicating insufficient bonding between the core and cladding.

Plate fabrication consisted of the standard picture frame technique employing alclad 6061 aluminum for both picture frame and cladding. The compact was 0.166 inch thick and the cladding 0.113 inch thick, such that with an 8.1 reduction the final thickness was 0.050 inch total. The plates were rolled at 500°C. Table II-17 gives the composition of each plate made from Heat 368. Figures II-20 and -21 show the typical core cross sections.

TABLE II-17

INSPECTION DATA OF THE TEST FUEL PLATES MADE FROM HEAT 368

Core: 64.685 wt% UAl (56.3 wt%, 92.25% enriched) -100 + 325 mesh +0.193 B_4C + X8001 aluminum -- 0.020 inch thick.

Cladding: 6061 aluminum alclad with 5% 1100 aluminum alclad on inside -- 0.015 inch thick.

Picture Frame: 6061 aluminum alclad with 5% 1100 aluminum.

Plate Number	Core Weight grams	Uranium Weight grams	U-235 Weight grams	B_4C Weight grams	Density g/cc	Gross Weight grams
I-47-1466	6.6795	2.4325	2.2440	0.0119	2.9562	17.4085
I-47-1467	6.6859	2.4349	2.2462	0.0129	2.9654	17.5092
I-47-1468	6.7001	2.4400	2.2509	0.0129	2.9301	17.2547
I-47-1469	6.7021	2.4408	2.2516	0.0219	2.9259	17.3066
I-47-1470	6.6577	2.4246	2.2367	0.0128	2.9397	17.4093
I-47-1471	6.6774	2.4318	2.2433	0.0129	2.9232	17.3701
I-47-1472	6.6818	2.4333	2.2447	0.0129	2.9078	17.4657
I-47-1473	6.6923	2.4372	2.2483	0.0129	2.9191	17.5552
I-47-1474	6.6901	2.4364	2.2476	0.0129	2.9101	17.4660
Totals	60.1669	21.9115	20.2133	0.1160		

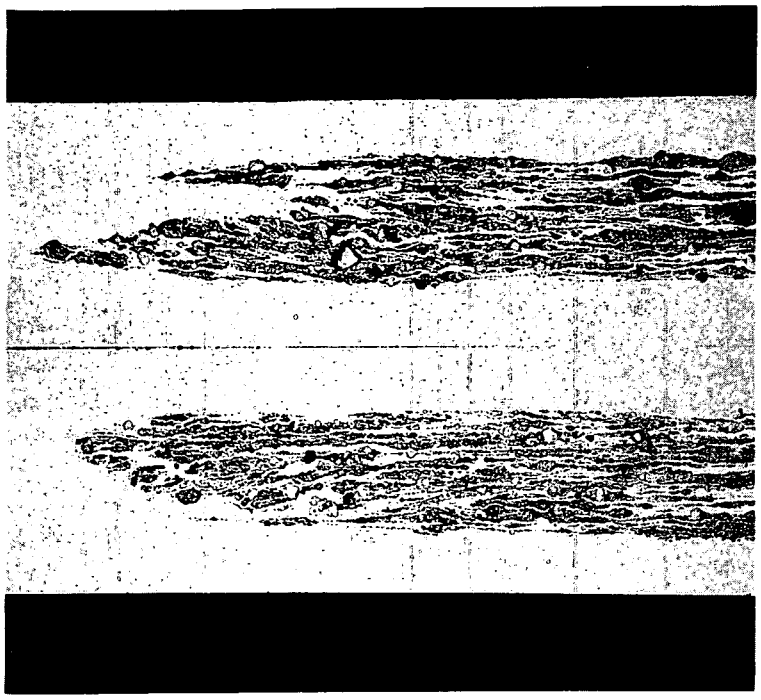

As-polished 25X

Fig. II-20 Sections of the "dogbone" ends of a typical test plate containing 55 wt% UAl powder.

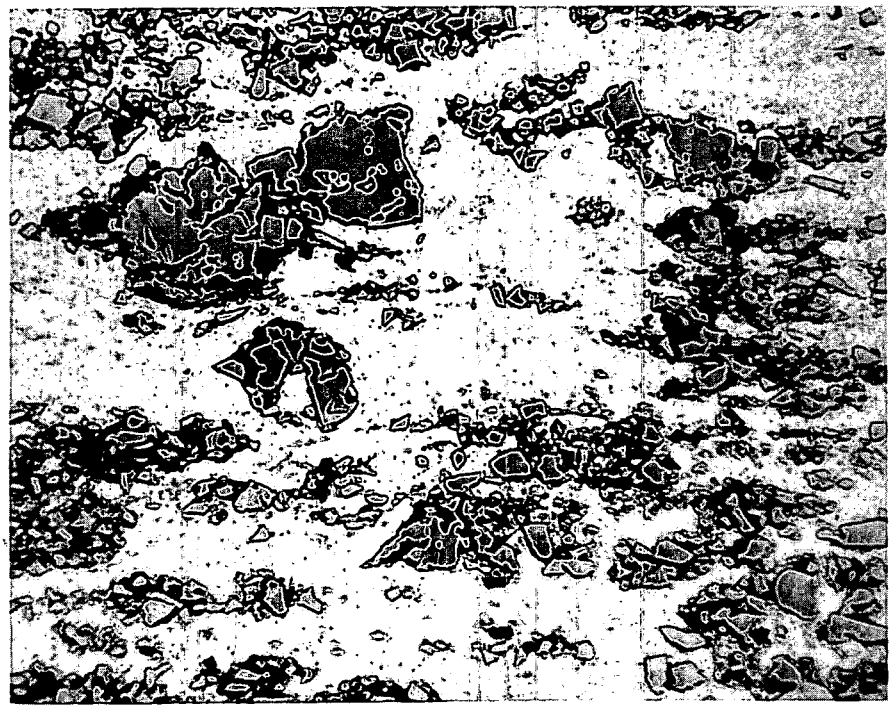

As-polished 500X

Fig. II-21 Longitudinal cross section of a typical test plate containing 55 wt% UAl powder.

After fabrication, each sample fuel plate was subjected to the following nondestructive tests:

(1) A blister test at 500°C before cold-rolling operations.

(2) A liquid nitrogen test for the determination of cladding integrity.

(3) An ultrasonic examination for the detection of macroscopic nonbonds.

(4) Radiography was used to determine the core configuration, extent of "dogboning", flaking, or gross segregation of any core constituent.

(5) The dimensions of the core and the total plate were checked against specifications. The specified core dimensions are 1.000 $\pm$ 0.015 inch x 5.500 +0.000 to -0.020 inch x 0.020 $\pm$ 0.002 inch. The total plate dimensions specified are 5.750 $\pm$ 0.005 inch x 1.250 $\pm$ 0.003 inch x 0.050 $\pm$ 0.003 inch.

Six of these test plates were then irradiated in the G-12 loop of the ETR during Cycles 93 through 96 to evaluate the irradiation stability of UAl alloy powder in making fuel plate cores. The G-12 loop parameters for these cycles also have been published previously[7]. A summary of data before and after irradiation is given in Table II-18.

Figure II-22 shows graphically how the 55 wt% UAl alloy sample fuel plates changed in volume with respect to burnup compared to previous data obtained with sample fuel plates containing UAl_3 + Al core dispersions. It can be seen that for relatively low burnups, a marked degree of shrinkage occurred; however, at some higher burnup the fission product gas accumulation offset the sintering effect and the plates began to swell.

The testing of the sample fuel plates was carried out in a tier arrangement[6]. The maximum nominal plate surface temperatures varied during testing from 130 to 180°C. The loop pressure was maintained at 760 psi. From other data obtained previously on specimens irradiated in the G-12 loop of the ETR and HB-2 loop of the MTR, it appears that observed sintering in sample fuel plates is related to at least four variables: (a) fuel plate temperature during irradiation, (b) the external pressure exerted on the plates during irradiation, (c) the as-fabricated porosity of the core of the sample plates prior to irradiation, and (d) the fuel material used[7, 8]. Because the pressure and temperature experienced by the composition 47 fuel plates was low compared with sample fuel plates (UAl_x + Al dispersions) irradiated in the HB-2 loop (1500 psi pressure and 260°C water temperature), the primary cause for the large volume change in the composition 47 plates appears to be the relatively low percent of theoretical density in the as-fabricated plates and the alloy powder used.

Figure II-23 shows the blister anneal temperatures of failure versus irradiation exposure (Table II-18 lists the blister failure temperatures) compared with sample fuel plates with UAl_x + B4C dispersed in aluminum. All of the

TABLE II-18

SUMMARY AND COMPARISON

OF PREIRRADIATION AND POSTIRRADIATION COMPOSITION

47 FUEL PLATE DATA

	Preirradiation			Postirradiation					
Plate Number	Density of Core (g/cc)	Volume of Core (% TD)	Volume of Core (cc)	Blister Anneal Failure Temperature (°F)	Blister Anneal Failure Temperature (°C)	Volume of Core (cc)	%ΔV/V	Burnup[a] (%)	Burnup fissions/cc x 10^{20}
I-47-1468	3.386	88.2	1.9870	1000	540	1.9779	-0.4607	63.7	15.7
I-47-1470	3.436	89.5	1.9469	1000	540	1.9282	-0.9626	52.1	13.0
I-47-1471	3.371	87.8	1.9895	1100	595	1.8814	-5.4312	8.5	2.1
I-47-1472	3.325	86.6	2.0195	1100	595	1.8787	-6.9730	15.5	3.7
I-47-1473	3.363	87.6	1.9981	900	480	1.9823	-0.7941	73.7	18.0
I-47-1474	3.328	86.7	2.0183	1100	595	1.8748	-7.1117	----	----

[a] This was determined by isotopic chemical analysis employing U-235/U-236 ratio method.

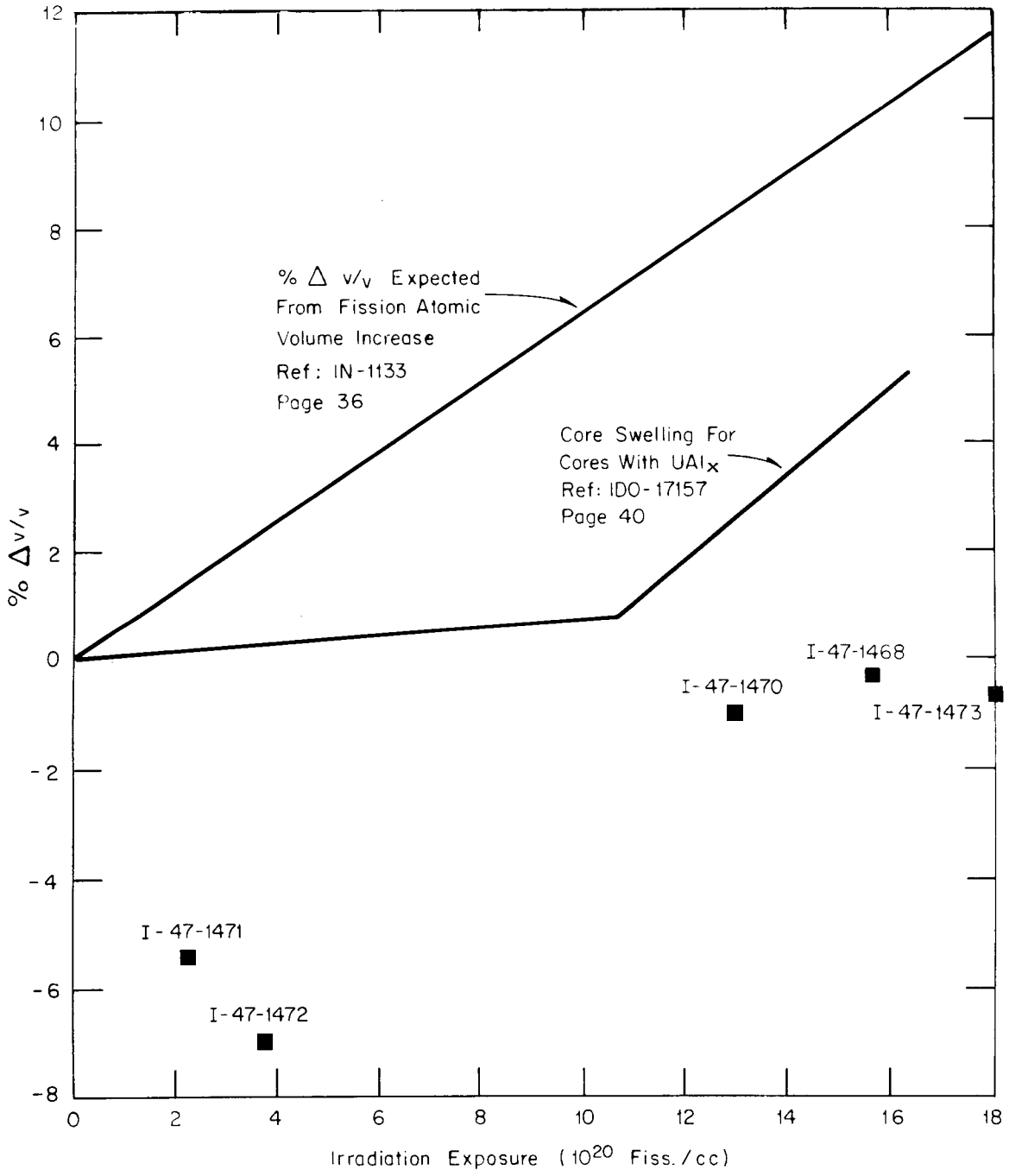

Fig. II-22 Core sintering behavior for the sample fuel plates tested compared to previously established swelling behavior of conventional cores.

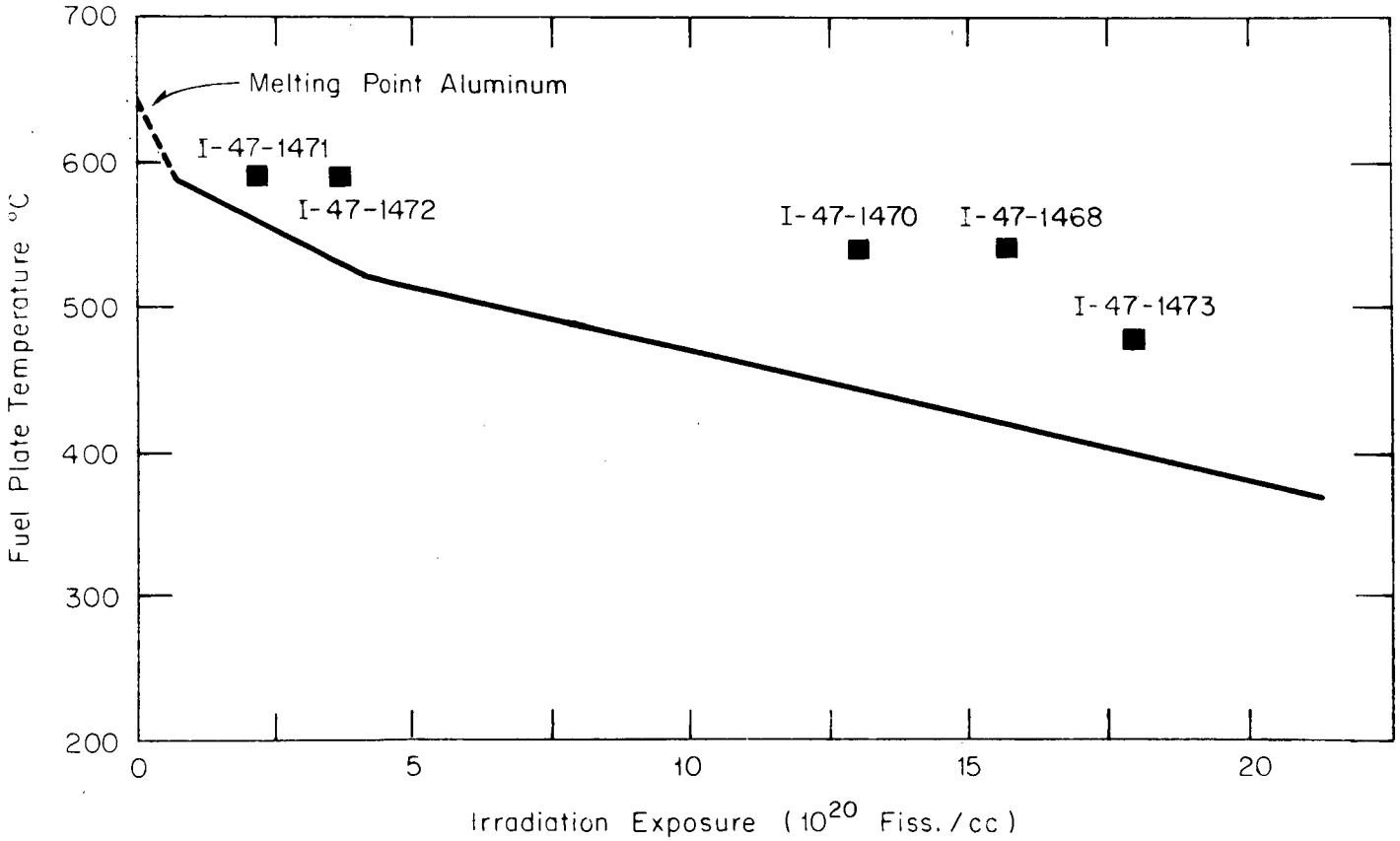

Fig. II-23 Blister temperatures of the 55 wt% UAl sample fuel plates compared with the established failure-no-failure line for sample fuel plates with $UAl_x + B_4C$ dispersed in aluminum.

plates examined were blister-tested to the point where the blisters formed would block the flow channels in a plate-type fuel element. It can be seen that the point of failure due to blistering for the sample plates examined was well above the established line at all burnup levels.

Figure II-24 shows that the points of initiation of blistering in this type of plate are near the periphery of the core as is common in most plate geometries. Figure II-25 shows a typical cross section of a blistered core at the final point of failure. Blisters of this type formed both within the core and adjacent to the cladding.

No sign of warping was found in the visual inspection of the plates after removal from the reactor. Some warpage, however, occurred at the highest annealing temperatures during blister testing.

Dimensioning of the plates showed a slight decrease in thickness due to irradiation; however, there was very little change in width or length measurements.

From the postirradiation examination of the sample fuel plates, the following would appear evident:

(1) Fifty-five wt% UAl alloy powder cores compare favorably with UAl_x + Al fuel dispersions from both a swelling and a blister standpoint

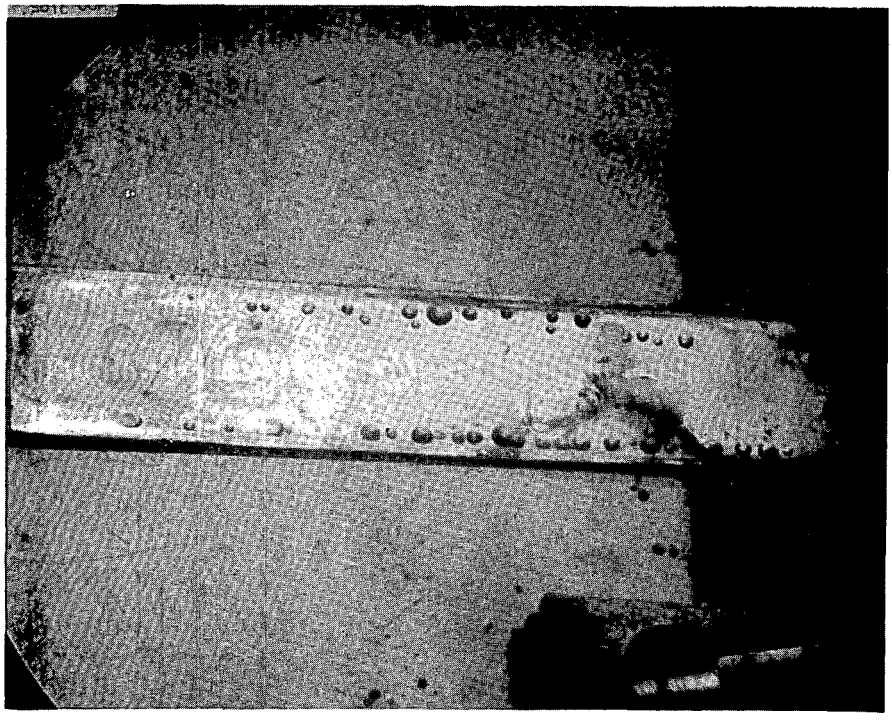

As-polished 50X

Fig. II-24 Distribution of blisters near the periphery of the core during the initial stages of blister testing.

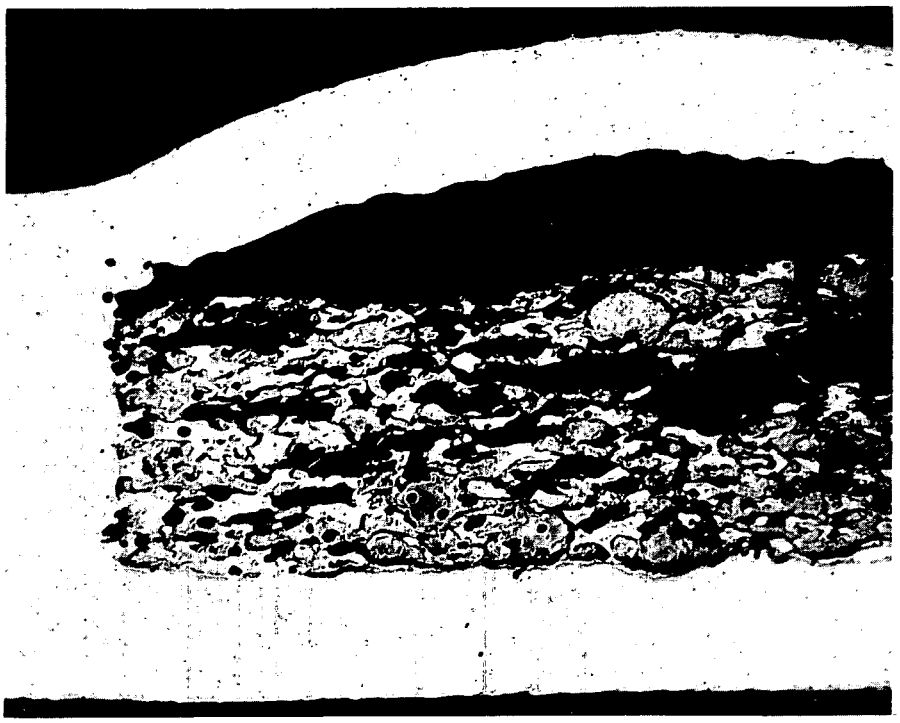

As-polished 50X

Fig. II-25 Typical core cross section of a sample fuel plate after failure has occurred by blistering.

(2) This material could warrant possible further testing in the areas of postirradiation mechanical properties determination and irradiation testing of full size fuel plates, if any economic incentive can be established.

3.4 Etch for UAl_3 (B. G. Carlson)

A successful etching procedure for unirradiated UAl_3 in bulk form has been developed which will allow before and after microstructural comparison of this fuel.

It has been possible to etch irradiated UAl_3 with an aqueous solution containing 10% Hf + 30% HNO_3 but this did not etch similar unirradiated material.

In the new procedure an exposure of 60 to 90 minutes at 600 to 630°C at a pressure of 0.01 to 0.1 μ Hg is the first step. This causes intergranular oxidation and leaves a thin oxide film covering the specimen surface. A very light polishing on a wheel charged with Linde A removes this oxide leaving the grains faintly visible. Further delineation of the grain boundaries takes place after swabbing with the Hf - HNO_3 etching solution. This step is followed by an electrolytic etch in a solution containing 25 g CrO_3, 240 ml acetic acid, and 30 ml H_2O with five volts passed through the sample for five minutes. The resulting structure is shown in Figure II-26. The second phase seen in this structure, as identified by microprobe, is UAl_2 which is darkened by this last step. Reheating the specimen at 600°C for 30 minutes under similar pressure reveals twins without a heavy oxide buildup as shown in Figure II-27.

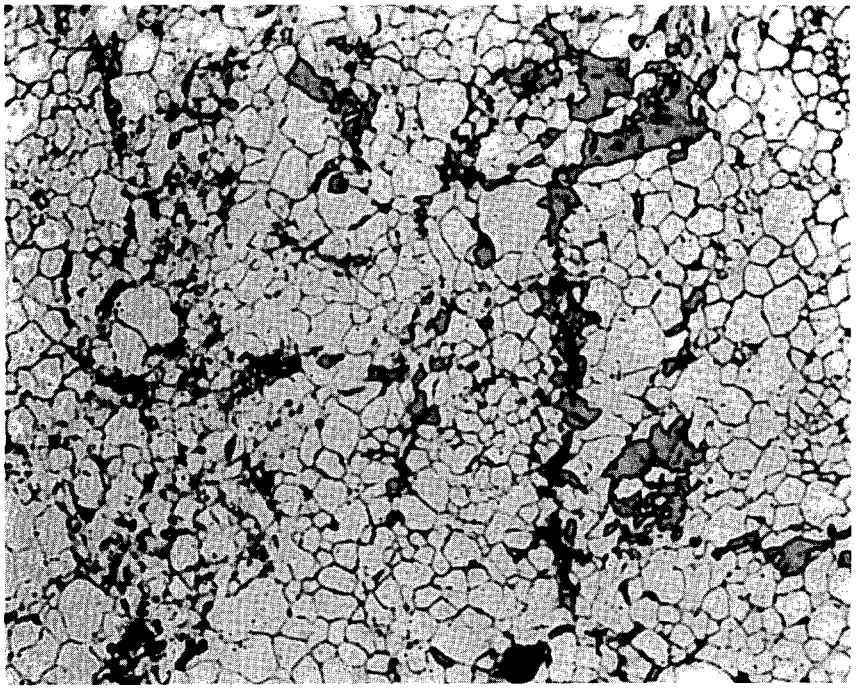

CrO_3 Acetic Etch 1000X

Fig. II-26 Microstructure of hot-pressed pellet of UAl_3. The darker material is UAl_2 in a matrix of UAl_3.

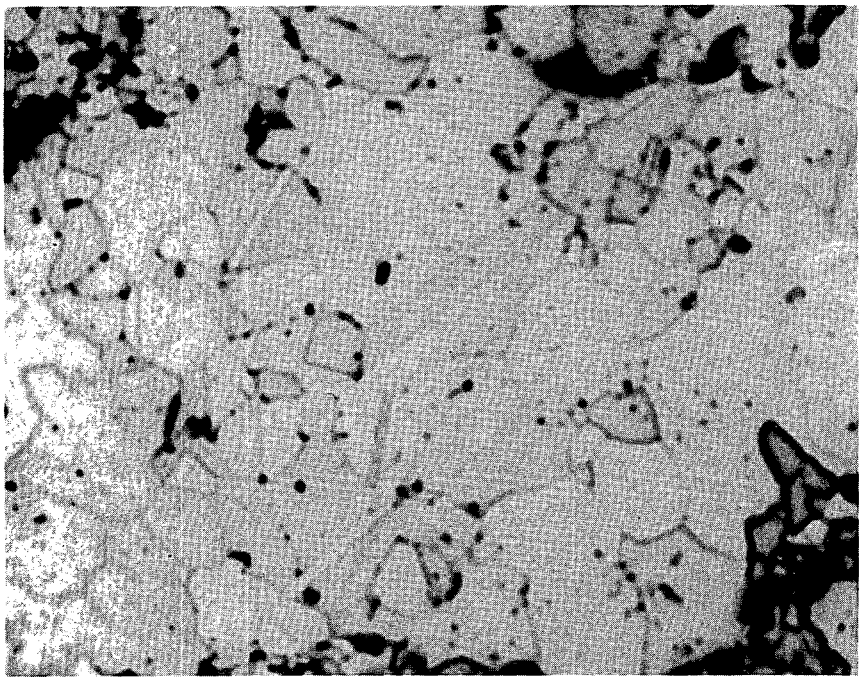

Heat Etch 1500X

Fig. II-27 Twinning in hot-pressed UAl_3 pellets as revealed after heat etching. Most of the field in this photo is from one UAl_3 particle.

A preferential oxidation at the grain boundaries allows preferential etching at the grain boundaries after heating. The oxide which has formed at the grain boundaries is not removed by the light polishing and is more sensitive to etching than a fresh surface.

3.5 A Comparison of the Compressive Yield Strengths of Irradiated and Unirradiated Standard ETR Fuel Plates at Various Temperatures (G. O. Hayner, J. O. Dittmer)

Since the first operation of the ETR (1957), the nuclear fuel loadings have increased from 255 to 500 g U-235 per assembly (or element). This has been done while stabilizing the neutron flux and extending the life of the core to 6000 MWd. Many fuel elements, because of the position variation in percent of core power, do not achieve the desirable nominal burnup of 30%. A considerable reduction in operating costs would be achieved if these elements were operated for a second cycle for additional burnup. Because of increased oxide buildup on the plate surfaces and, therefore, higher thermal stresses applied to the fuel plate, the mechanical properties of the plate must be determined.

Calculations of axial stresses indicate that during operation the fuel plates are almost completely in compression and the side plates that support the fuel plates are in tension[9]. Because of the very brittle behavior of the fuel plates after they have undergone irradiation[10] and the type of thermal stressing applied to the fuel plates, a determination of the compressive mechanical properties is indicated.

A testing program was, therefore, undertaken to determine the compressive yield strengths (0.2% offset method) of several standard irradiated and unirradiated ETR fuel plates. Sixty-one irradiated test specimens and 66 unirradiated test specimens were used for the primary portion of the study. These were tested at room temperature and from 150 to 370°C in increments of 40°C. The irradiated specimens were machined from five individual fuel plates from a standard 500 g U-235 ETR fuel element which operated in a high flux position (2.5% of core power) for an average burnup of 7.1×10^{20} fissions/cc. The unirradiated specimens were machined from three ETR fuel plates which were also obtained from a standard ETR fuel element. All of the fuel plates consisted of a 1100-H12 aluminum alloy cladding 0.015 inch thick and a fuel core 0.020 inch thick containing 35 wt% UAl_x and 0.1 wt% B_4C poison in a 1100 aluminum alloy matrix. All of the fuel plates had been fabricated by Atomics International.

A subpress assembly was employed during testing[11] which utilized grooved tungsten carbide blocks to provide specimen support and to prevent buckling during loading. The specimen mounted in the subpress was loaded in compression by an Instron Univeral Testing Machine. The subpress was surrounded by a split Marshall Furnace for all testing performed at elevated temperatures; an extensometer mounted externally recorded the strain directly during compression of the specimens. The specimens were maintained at test temperature for approximately 15 minutes before testing began. The equipment used was designed to meet ASTM Standard E-209-65.

Twenty-seven unirradiated 6061-T6 aluminum alloy control specimens were also tested in the same manner as the composite specimens above and

compared with tensile data from the literature[12] to provide assurance that the values obtained on the composite specimens were accurate. The final dimensions of the composite test specimens were 3.000 ± 0.005 inch x 0.750 ± 0.010 inch x 0.050 ± 0.002 inch. The final dimensions of the control test specimens were 3.00 ± 0.003 inch x 1.250 ± 0.005 inch x 0.100 ± 0.002 inch. Figure II-28 shows the results of testing the control specimens (yield strength versus temperature) and compares these results with data obtained from the literature on 6061-T6 aluminum in tension.

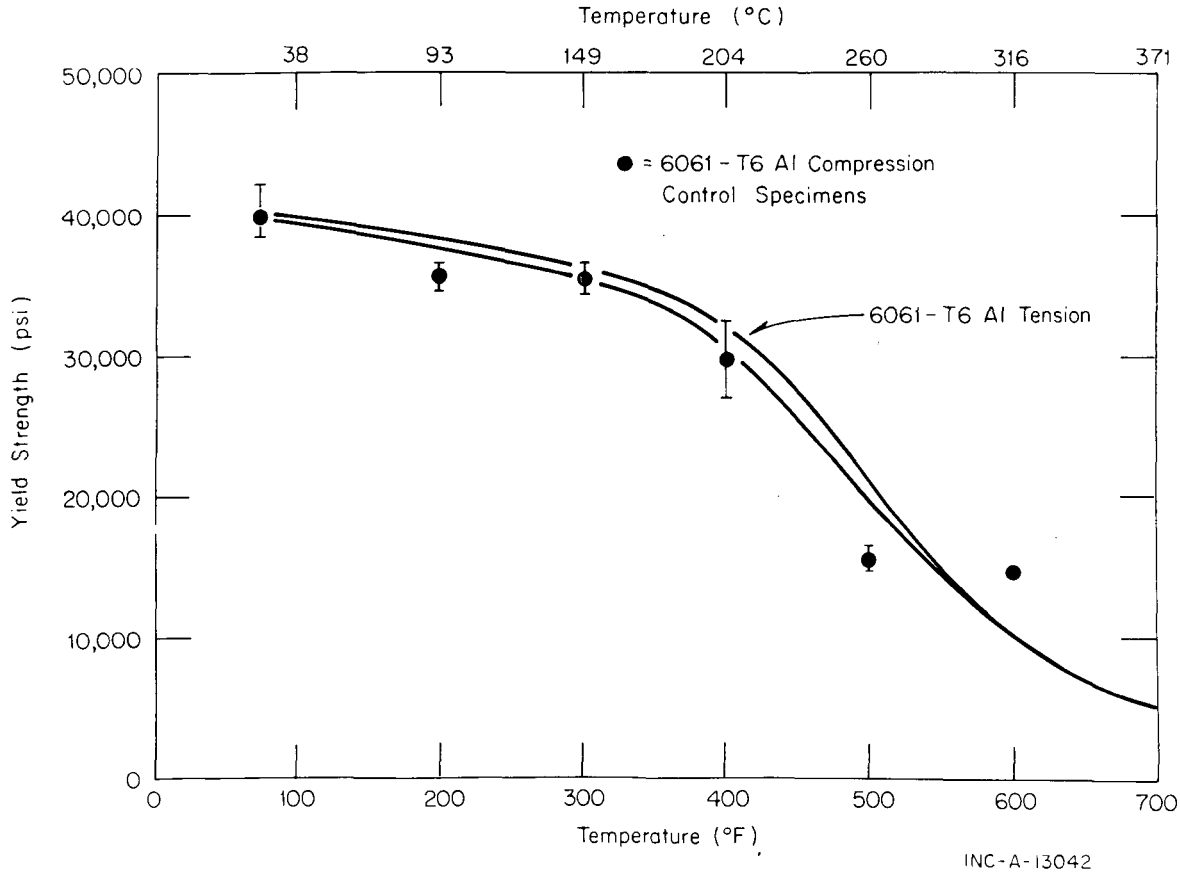

Fig. II-28 Summary of compression testing data of control specimens comparing test data with published values for 6061-T6 aluminum.

To simulate reactor conditions, the irradiated specimens were tested according to burnup, ie, those specimens with lower burnup were tested at lower temperatures and the specimens with higher burnups were tested at higher temperatures. The approximate range of burnups was from 2 to 14 x 10^{20} fissions/cc. Figure II-29 shows a comparison between the results obtained during testing on the irradiated and unirradiated composite specimens; these results are then compared with 1100 aluminum containing two degrees of cold work[13]. It can be seen that the unirradiated specimens show a much higher yield strength at room temperature than the irradiated test specimens and that this difference in strength decreases until a test temperature of approximately 300°C is reached. As expected, from this temperature to 370°C the yield strengths of the two materials are nearly the same.

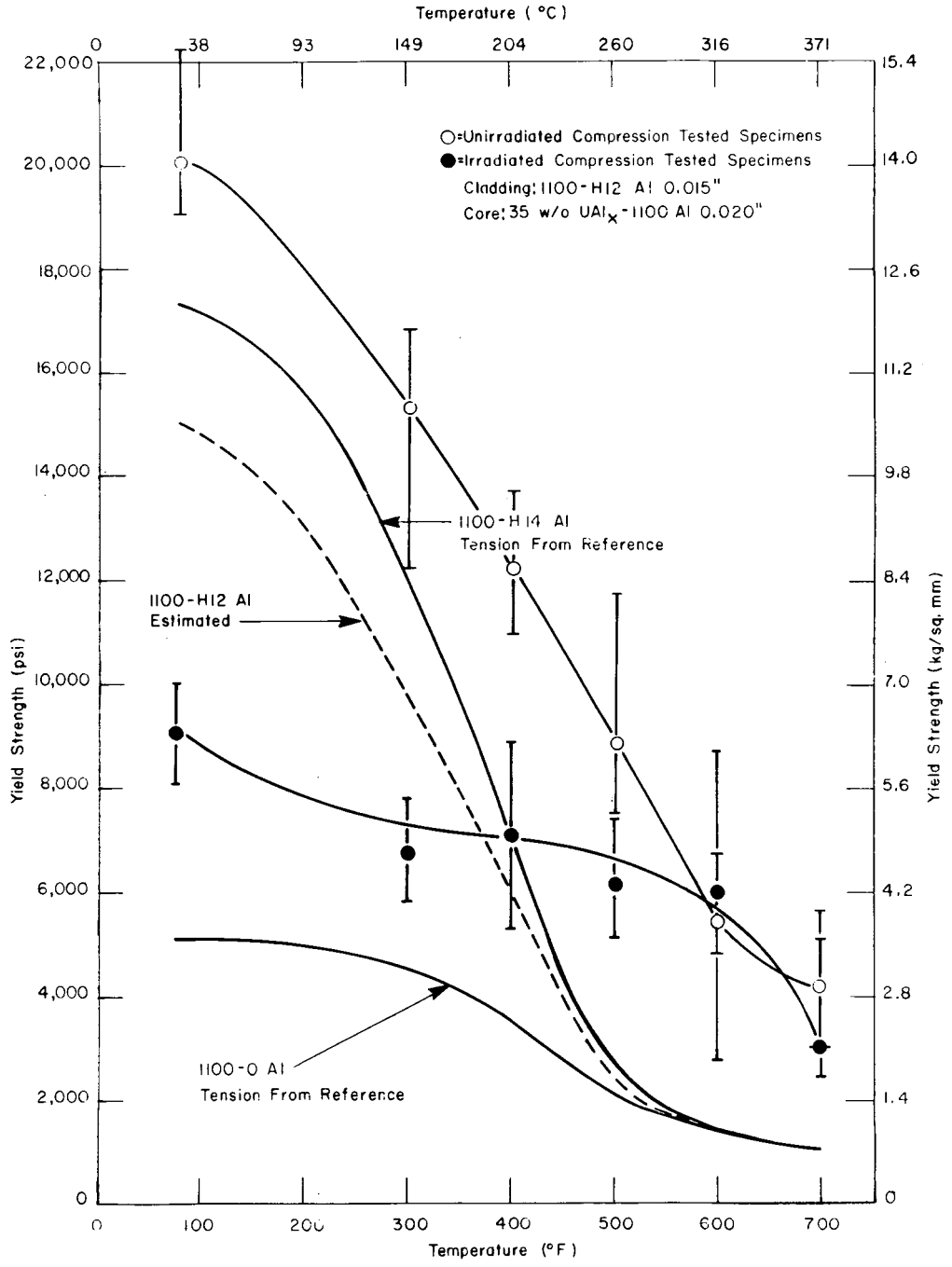

Fig. II-29 Summary of compression testing data of ETR composition specimens comparing test results with published values for 1100-H14 and 1100-0 aluminum and an estimated curve for 1100-H12 aluminum.

The following conclusions can be made from the preliminary study that was conducted:

(1) The unirradiated ETR fuel plates evaluated show an increase in compressive yield strength at all test temperatures over the cold-worked cladding material (1100-H12)

(2) The unirradiated ETR fuel plates tested have a higher compressive yield strength than the irradiated ETR fuel plates up to approximately 300°C

(3) The ETR composition fuel plates have a loss in strength at the end of a normal operating cycle.

4. TECHNICAL SUPPORT WORK

4.1 Metallurgical Evaluation of Zircaloy Exposed to Emergency-Core-Cooling Conditions (M. J. Graber, W. F. Zelenzy)

Scoping tests performed to determine the problem areas in nuclear reactor emergency-core-cooling have subjected Zircaloy, with a variety of prior histories, to a variety of time, temperature, and oxygen exposure conditions[14]. The samples were metallurgically evaluated to determine relationships between prior history, microstructure, properties, and performance. The starting material was Zircaloy-2 tubing ASTM grade B-353 with a specified ASTM grain size of less than seven. The sample pretreatments prior to cooling tests were (a) as-received, (b) a Hf + HNO_3 pickle to remove between 0.001 and 0.0015 inch of material from the surface, (c) steam corroding at 660°F for three days, and (d) pickling plus steam corroding.

During the emergency-core-cooling tests, some of the samples were heated in argon, held at temperature while being exposed to steam, and then cooled in argon. Other samples were exposed to steam or argon during the entire temperature cycle. The maximum temperatures in any one cycle varied from 925 to 1315°C.

The samples were examined visually, optically, and analyzed by the electron microprobe. They were also tested for mechanical property, weight, and electrical resistivity changes. Since some of the samples showed large losses in ductility, a "ring compression" test was developed which is adaptable to tubing samples and more sensitive than axial compression tests. A half-inch long section of the tubing was diametrically compressed until failure. Failure was indicated by a large load drop on autographically recorded load-deflection curves and is observed as a crack at the point of maximum deformation or by shattering of the specimen. The "ring compression percent" of the original tube diameter at the time of failure was used as a measure of ductility.

It was found, depending on the time-temperature cycle, that Zircaloy exposed to steam undergoes surface oxidation, oxygen absorption, grain growth, phase transformation, zirconium oxide precipitation, and embrittlement [15, 16]. Zirconium normally transforms from α to β at 862°C[17]. A very narrow two-phase region, $\alpha + \beta$, is greatly widened with increased oxygen content[18]. The length of time certain samples were held in or cooled through the two-phase region is plotted against the "ring compression percent" in Figure II-30. These particular samples were heated sufficiently to ensure α to β transformation (1150°C) and had essentially the same oxygen content (10 at.%). As shown, embrittlement (or loss of ductility) increased as a function of time spent in the two-phase region after oxygen absorption. The changes in microstructure from ductile

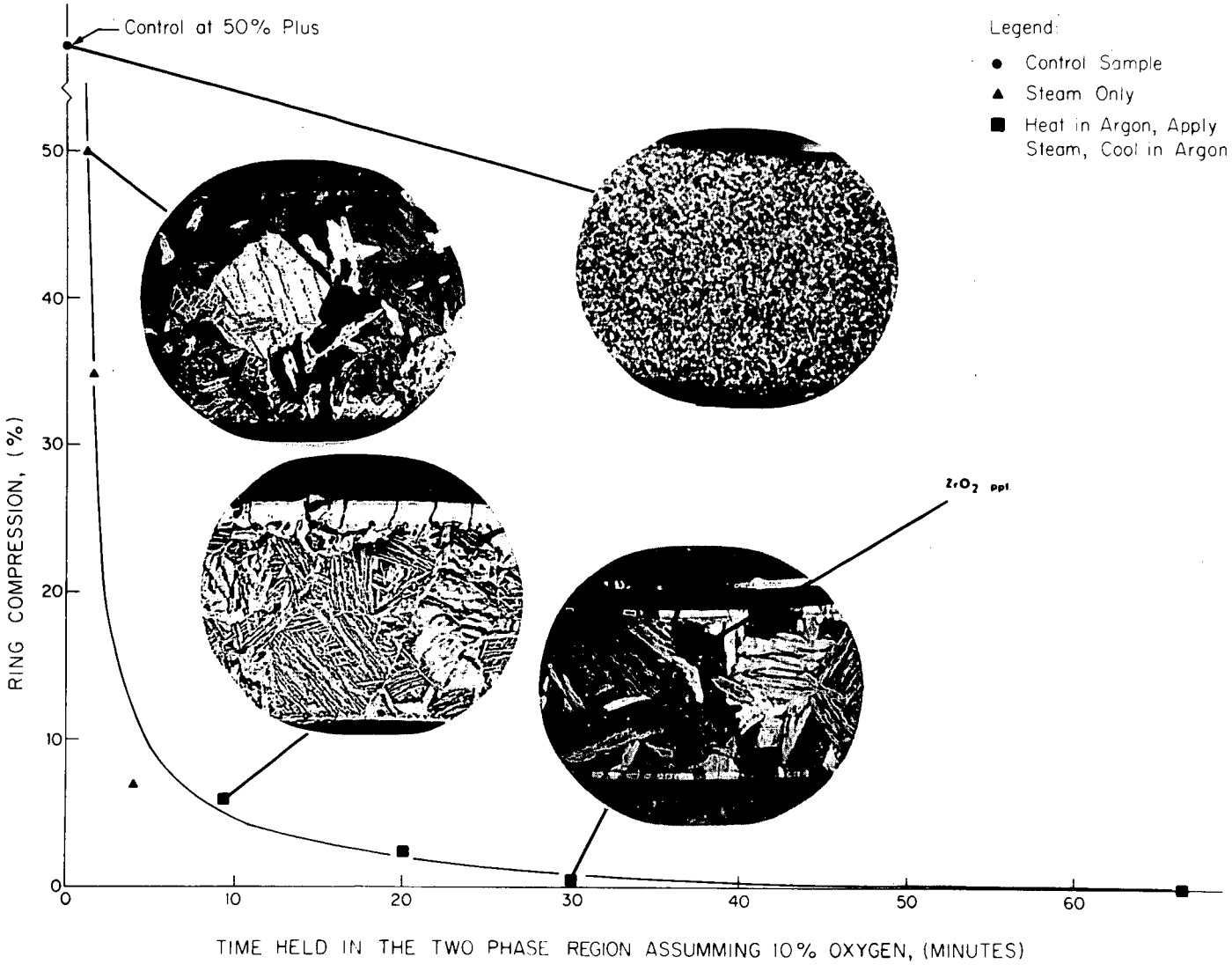

Fig. II-30 The effect of time in the oxygen-extended two-phase region, alpha plus beta, on Zircaloy-2.

to brittle also are shown. As determined by electron microprobe, platelets of zirconium oxide have precipitated adjacent to needle-like Zircaloy grains in the embrittled structure. This would indicate that embrittlement of Zircaloy in emergency core cooling could be minimized by staying below or cooling rapidly through the two-phase region.

Another series of samples in which heatup and cooling rates were held constant but the maximum temperatures attained were varied had time-temperature profiles similar to those predicted for the Browns Ferry BWR Reactor [19]. Here with more rapid cooling rates, the embrittlement mechanism changed in nature. It was then a function of the maximum temperature attained and the depth of an oxygen saturated α layer on the tube surface which developed intergranular oxidation. Table II-19 shows how various temperature profiles affect the mechanical properties as measured by the "ring compression" test for simulated BWR conditions. The data indicate that about 90% of the pins would retain ductile behavior.

TABLE II-19

MAXIMUM TEMPERATURE CONDITIONS AND PERCENT RING COMPRESSION

Sample Number	Temperature Profile[a]	Percent Ring Compression at Failure
1	6 min at 1740°F	Ductile, 50%
2	6 min at 1780°F	Ductile, 50%
3	6 min at 1880°F	Ductile, 50%
4	6 min at 1980°F	Ductile, 50%
5	1 min at 2050°F	Ductile, 50%
	2 min ramp to 1600°F	
	20 min ramp to 1500°F	
6	6 min at 2150°F	Brittle, 12%
7	1 min at 2460°F	Brittle, 0%
	6 min ramp to 1600°F	
	16 min ramp to 1200°F	

[a] Heatup rates for Samples 1, 2, 3, 4, and 6 were approximately 40 to 70°F per second. For Samples 5 and 7 the heatup rate was 80°F per second. Cooldown from indicated profile to ambient temperature was at a rate of approximately 20°F per second for all samples.

4.2 Failure Analysis

4.21 ATR Instrument Air Line (M. J. Graber, B. G. Carlson). A failure analysis was performed on the connection pipe between "PSV-1-1 and PJV-1-1A", an air line at the ATR. The specimen was examined to determine if a fatigue failure mechanism might have been active. In addition, the material was examined to determine if the apparent brittle behavior was a property

inherent in the material or came about as a result of the notch effect produced by the pipe threads. During this examination, the pipe material was found to be ductile and the fracture surface did not show evidence of fatigue.

The optical metallography, mechanical test work, and electron microscopy needed to arrive at the above stated conclusions are reported herein.

Macroscopic examination of the fracture surface did not reveal any evidence of fatigue. The fracture features were too small to interpret at low magnifications. To reveal the structure, three electron microscope fractographs were taken from two fractured surface areas shown on Figure II-31.

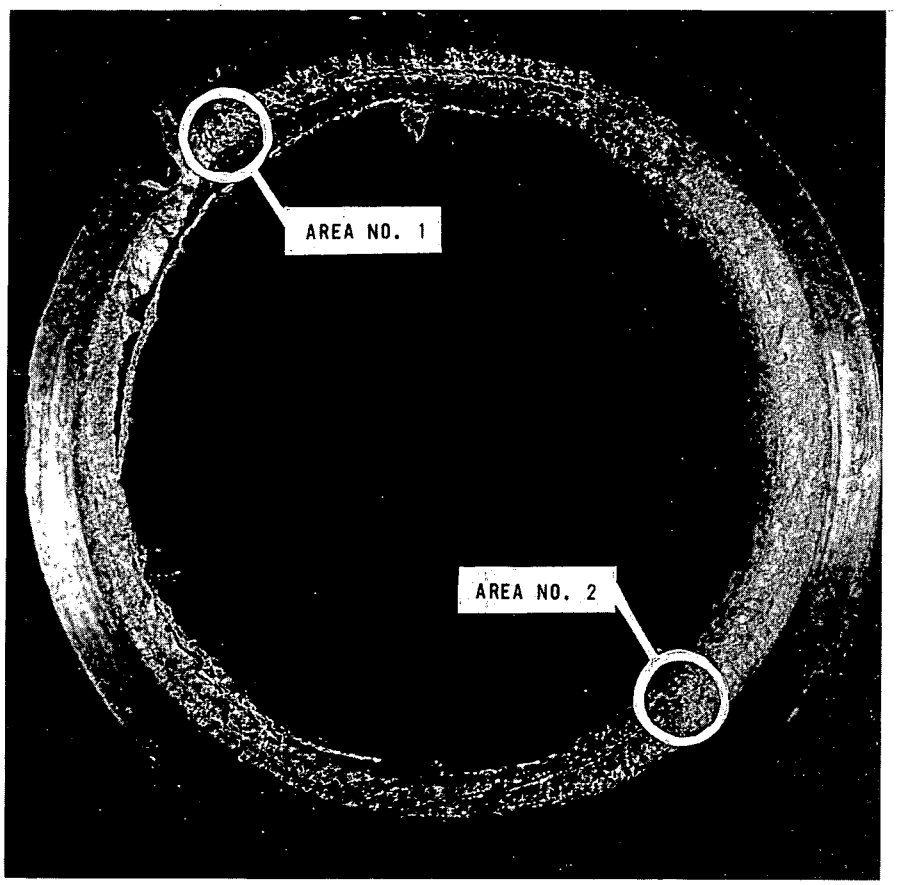

Fig. II-31 Macrophotograph of fractured air line showing areas from which fractographs were made. Area No. 1 is in the breakover region; No. 2 is directly across from the breakover.

Figure II-32 and -33 show the two fractographs taken from area No. 1. A ductile structure (dimpling) is shown in Figure II-32 while that of Figure II-33 shows brittlements (quasi-cleavage) as well as ductility. The fractograph from area No. 2 (see Figure II-34) also exhibited a brittle structure (river).

Many other locations on the fractographs, other than the typical examples shown herein, were examined. There was no evidence of fatigue.

To show that this brittle behavior was caused by the notch effect of the threads, a section from this pipe approximately 1/2-inch wide was crushed in a vise as a ductility test. Completely flattening the section did not cause cracking; this would indicate that the material was ductile. The hardness was

6200X

Fig. II-32 Ductile structure of fractured air line showing dimpling.

6200X

Fig. II-33 Electron micrograph of fractured air line showing indications of some brittleness -- quasi-cleavage.

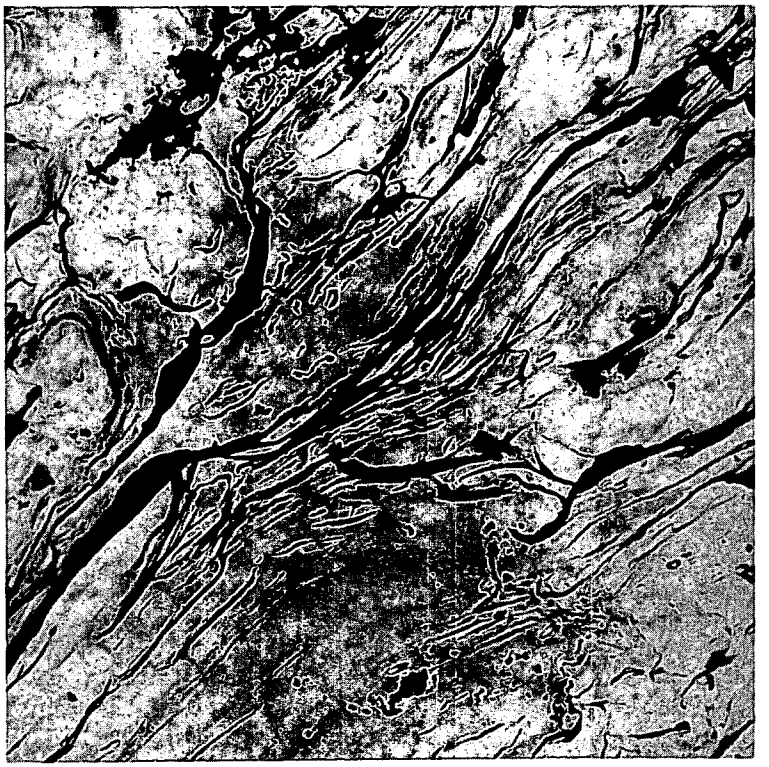

6200X

Fig. II-34 "River" structure from fractured air line indicating brittle behavior and a running crack. This is from opposite the breakover point area.

in the Rockwell B.70 range which would also indicate a ductile material. A typical microstructure of this material, shown in Figure II-35, is largely ferrite, as would be expected of a low carbon pipe, and is typically ductile.

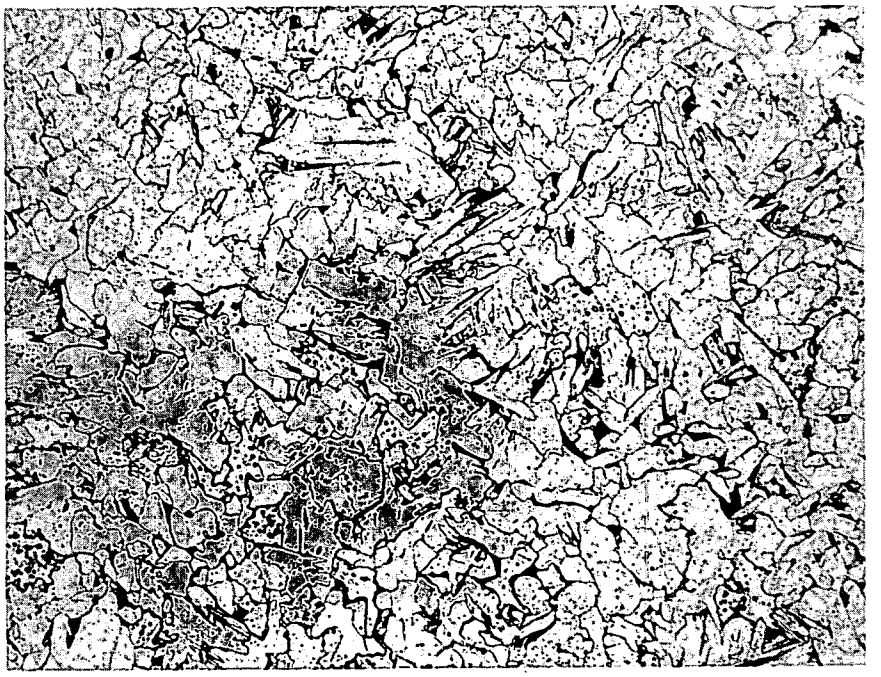

Nital Etch 100X

Fig. II-35 Typical pipe area showing an almost completely ferrite structure.

4.22 ATR Primary Water Pump (M. J. Graber). The welds used to fasten the ATR primary cooling system motor shroud were examined for cause of failure. Several of these welds had separated causing portions of the shroud to be drawn into the pump motor resulting in some damage to both motor and shroud. Failure of these welds was due to a poor welding technique.

As delivered to the Metallurgy Laboratory, there were only two weldments in the entire shroud assembly still intact. One of these weldments had a visible crack which ran about one-third of the total length, Figure II-36. When this weld was parted during handling, it was found that the fractured surfaces were discolored in the areas of the original crack and that the shading was comparable to that of the red paint used on the shroud.

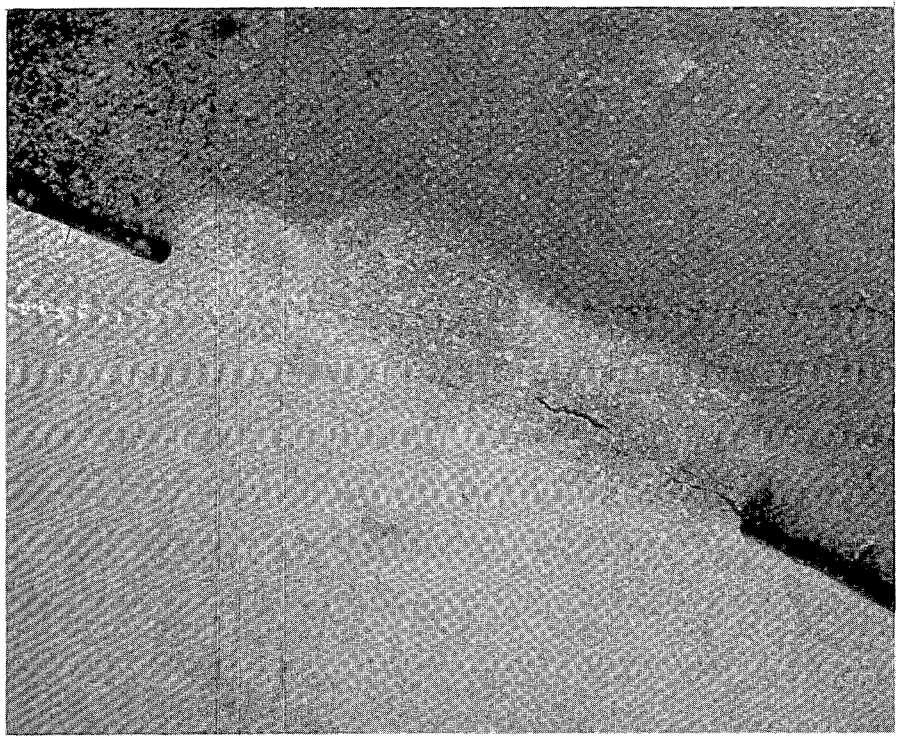

≈2X

Fig. II-36 One of two remaining weldments on the ATR primary cooling system motor shroud showing a typical longitudinal crack.

This discoloration was not analyzed but (whether rust or paint) indicates an older portion of the fracture. Another typical defect more readily distinguishable is the crater crack shown in Figure II-37 which was found in lock weldments used on the nuts of the shroud fastening bolts.

The microstructure of the weldments, Figure II-38, showed a single weld bead, good fusion with the base metal, and low porosity. The base metal hardness was R_b 67 and the weld metal R_b 82.

≈2X

Fig. II-37 Crater crack on lock weldment holding the nuts of the shroud fastening bolts secure.

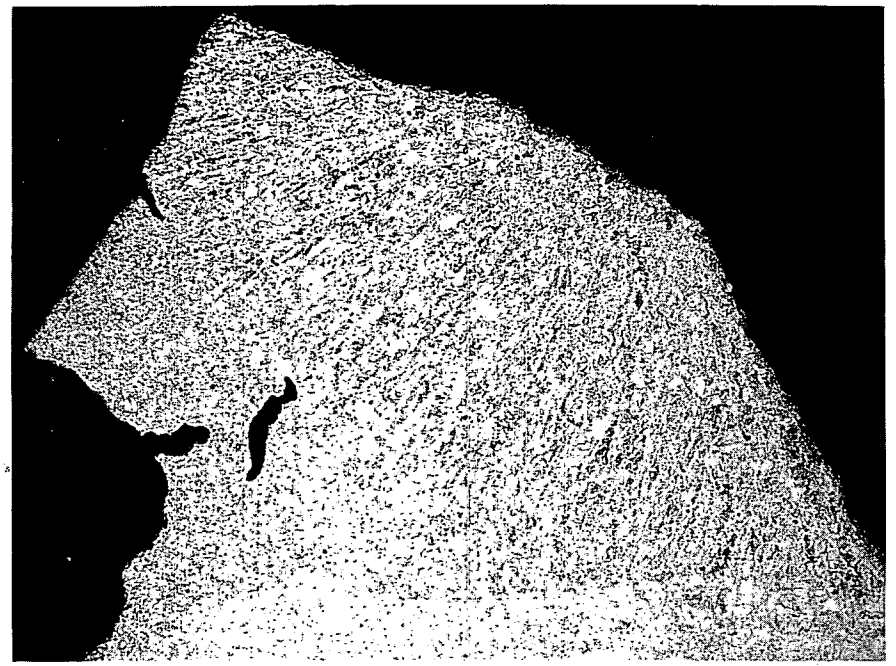

Nital Etch 20X

Fig. II-38 Weld cross section showing good fusion with base metal. Cracks shown here probably were formed when the weld separated.

An X-ray diffraction analysis of the materials showed the following percentage of elements:

	Base Metal	Weld Metal
Manganese	0.40	0.53
Copper	0.24	0.30
Molybdenum	0.01	0.09
Chromium	0.04	0.20
Nickel	0.09	0.17
Silicon	0.03	0.35

Cracking of the weld metal can result from a number of causes:

(1) High joint rigidity or lack of preheat

(2) Diffusion of alloy elements from base metal to weld metal causing a composition which has poor properties

(3) Faulty electrodes which contain moisture, hydrogen, or poor geometry at the striking end

(4) Poor joint fit up such as excessive gap

(5) Too small initial weld bend

(6) High sulfur in base metal or weld metal

(7) Distortion due to improper location of weldments or sequence of application

(8) Lack of soundness (excessive porosity)

(9) Crater cracks

(10) Hot shortness due to excessive copper content. It is normally recommended that copper content remain below 0.10% if hot shortness is a problem; however, hot short cracks (intergranular) were not detected during the examination.

Crater cracks are caused by pulling the welding rod out of the puddle before it is filled.

5. REFERENCES

1. G. W. Gibson, M. J. Graber, and M. F. Marchbanks, "The Development of Boron-Aluminum Foils as Controllable Neutron Absorbers in Aluminum-Clad Nuclear Fuel Elements", in E. D. Covington (ed.), Reactor Engineering Branch Annual Report -- FY-1968, IN-1228 (February 1969) pp 20-23.

2. W. C. Thurber et al, Irradiation Testing of Fuel for Core B of Enrico Fermi Fast Breeder Reactor, ORNL-3709 (November 1964).

3. G. W. Gibson and M. J. Graber, Annual Progress Report on Reactor Fuels and Materials Development for FY-1967, IN-1311 (February 1968).

4. V. A. Walker, M. J. Graber, and G. W. Gibson, ATR Fuel Materials Development Irradiation Results -- Part II, IDO-17157 (June 1966).

5. H. J. Eding and E. M. Carr, High Purity Uranium Compounds -- Final Report, ANL-6339 (1961).

6. E. D. Covington (ed.), Reactor Engineering Branch Annual Report -- FY-1968, IN-1228 (February 1969).

7. G. W. Gibson, The Development of Powdered Uranium-Aluminide Compounds for Use as Nuclear Reactor Fuels, IN-1133 (December 1967).

8. W. C. Francis and R. A. Moen (eds.), Annual Progress Report on Reactor Fuels and Materials Development for FY-1966, IDO-17218 (November 1966) pp. 44-50.

9. C. A. Moore, Phillips Petroleum Company, unpublished data.

10. G. W. Gibson and W. C. Francis, Annual Progress Report on Fuel Element Development for FY-1962, IDO-16799 (August 1962).

11. K. C. Sumpter, A Primary Study on the Compressive Properties of Composite Nuclear Fuel Plates, IN-1179 (April 1968).

12. W. R. Martin and J. R. Weir, Mechanical Properties of X8001 and 6061 Aluminum Alloys and Aluminum-Base Fuel Dispersion at Elevated Temperatures, ORNL-3557 (February 1964).

13. "Typical Tensile Properties at Various Temperatures", in Aluminum Company of America, Alcoa Aluminum Handbook, Pittsburgh: Aluminum Company of America, 1962.

14. R. Herzel and R. H. Meservey, "The Brittle Behavior of Zircaloy Under Emergency-Core-Cooling Conditions", ANS Trans., 12 n 1 (June 1969) pp. 355-356.

15. L. Baker, Jr. and L. C. Just, Studies of Metal-Water Reactions at High Temperatures III. Experimental and Theoretical Studies of the Zirconium-Water Reaction, ANL-6548 (May 1962).

16. J. P. Pemsler, "Studies on the Oxygen Gradients in Oxidizing Metals. V. The Oxidation of Oxygen-Saturated Zirconium", J. Electrochem. Soc., 113 (December 1966) pp. 1241-1244.

17. P. L. Rittenhouse and M. L. Picklesimer, Metallurgy of Zircaloy-2 -- Part I. The Effects of Fabrication Variables on the Anisotrophy of Mechanical Properties, ORNL-2944 (November 1960).

18. M. Hansen and K. Anderko, Constitution of Binary Alloys, 2nd ed., New York: McGraw-Hill Book Company, Inc., 1958.

19. F. A. Schroub and J. E. Leonard, Core Spray and Core Flooding Heat Transfer Effectiveness in a Full-Scale Boiling Water Reactor Bundle, APED-5529 (June 1968).

III. ENGINEERING EXPERIMENTS

1. ATR THERMAL-HYDRAULICS

(M. L. Griebenow, G. N. Fillmore, J. A. Hendricks, F. O. Haroldsen, and E. H. Porter)

1.1 Core I Thermal-Hydraulics

An extensive thermal-hydraulic test series was conducted during the ATR Core I Startup Program to determine the limiting heat transfer in natural convection and in the emergency and operational coolant flow regimes. The tests utilized three experimental fuel elements, each of which had either one or two double core fuel plates. The double core fuel plates each had two standard fuel cores (to double the heat transfer rates) separated by a layer of aluminum containing a series of thermocouples. The experimental fuel elements used for the forced flow tests also had pitot tubes at the lower end of the coolant channels to measure existing flow rates. One of these experimental fuel elements is shown in Figures III-1 through -4.

Initial conclusions drawn from the test series are:

(1) Natural Convection Series

(a) The onset of boiling does not cause a divergent flow oscillation. No thermal-hydraulic limitation was observed because the tests were limited by reactivity feedback oscillations.

(b) Depressurized natural convection (at 26.7°C bulk coolant) can accommodate decay heat one-half hour after terminating 250 MW, 40-50-60 unbalanced operation.

(c) Pressurized natural convection (at 51.5°C bulk coolant) can accommodate decay heat approximately 36 seconds after terminating 250 MW, 40-50-60 unbalanced operation.

(2) Flow Reversal

The transition from normal full power operating pressure and flow (downward through the fuel elements) to fully developed natural convection (upward flow through the fuel elements) can be achieved at any power level (either decay or fission heat) that can be accommodated by the natural convection process. There is no transient overshoot of the fuel plate temperatures during the transition.

(3) Emergency Cooling Series

The following emergency cooling flow rates, system pressures, and inlet coolant temperatures operated stably,

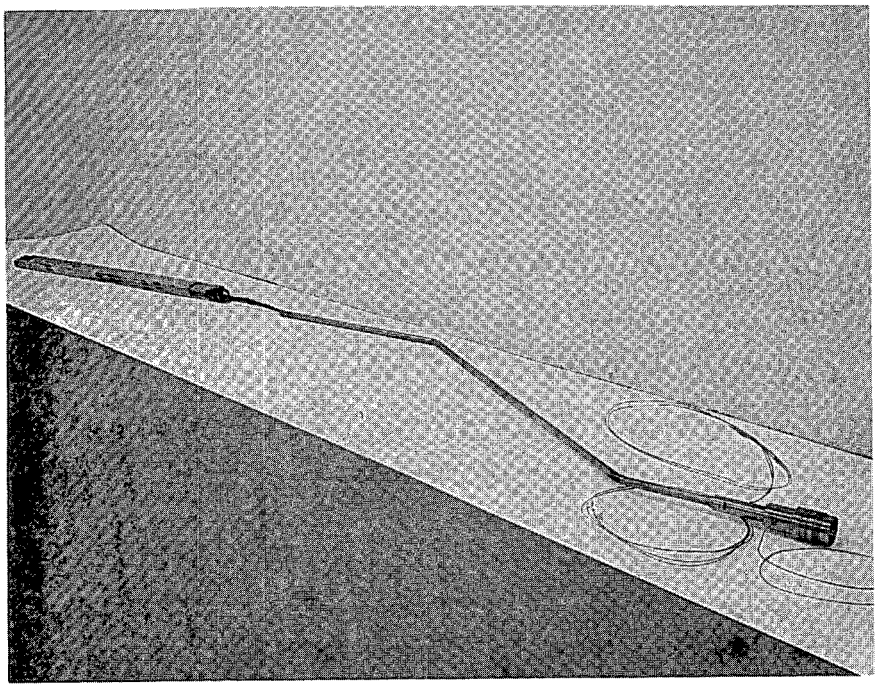

Fig. III-1 Experimental fuel element and associated leads used in ATR Core I tests.

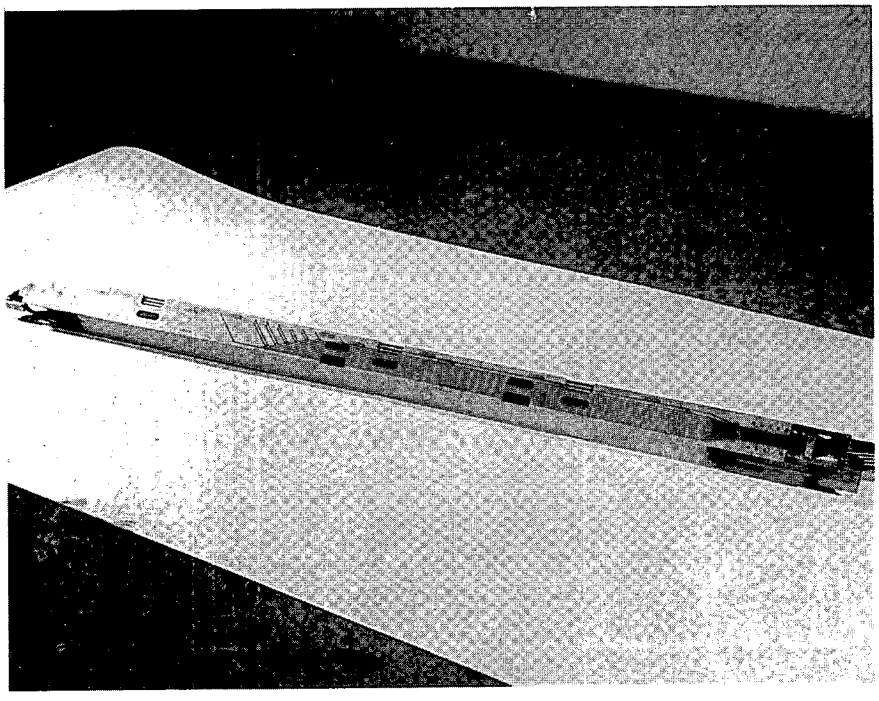

Fig. III-2 Experimental fuel element showing thermocouple penetrations.

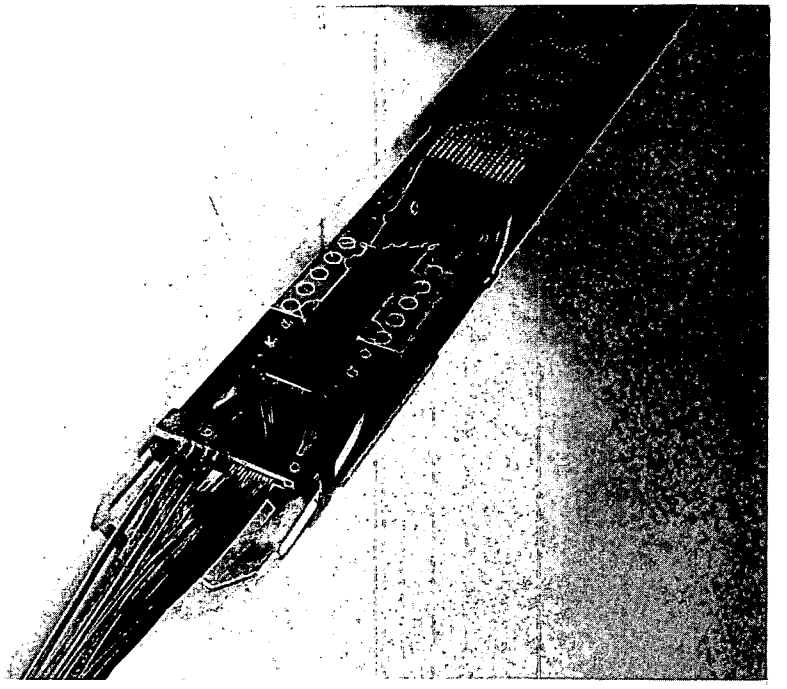

Fig. III-3 Experimental fuel element showing lead attachment details.

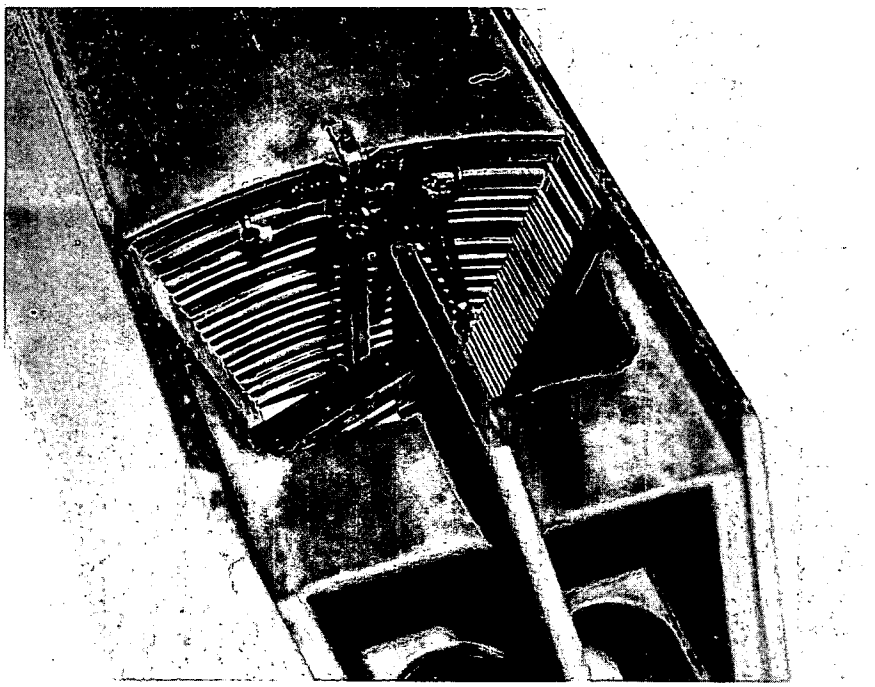

Fig. III-4 Experimental fuel element showing double core plates and pitot tube installation.

with the experimental fuel element in the hot core position up to the stated power levels in the 40-50-60 power unbalanced configuration:

(a) 4500 gpm, atmospheric pressure, 26.7°C coolant, 20 MW

(b) 4700 gpm, atmospheric pressure, 51.5°C coolant, 19 MW

(c) 4300 gpm, 260 psig, 51.5°C coolant, 46 MW

(d) 2500 gpm, 260 psig, 51.5°C coolant, 28 MW

(e) 3600 gpm, 260 psig, 51.5°C coolant, 34 MW.

Application of these test results to normal operating conditions, with standard and/or zone-loaded fuel elements, is incomplete. The results, however, will be higher than the indicated power levels.

The emergency cooling tests were terminated [with exception of (a)] by a flow instability that was associated with bulk boiling at the outlet from the hot coolant channel. The flow instability was accompanied by a thermal transient that was much slower (and of smaller amplitude) than expected.

(4) Full Flow and Pressure Series

During this test the reactor was cooled with the normal full operating coolant flow (100 psi across the core, resulting in about 46,000 gpm) at 51.5°C. The system was pressurized to the normal operating level (374 psig at the inlet), and the power was increased in steps to 170 MW in the 40-50-60 unbalanced configuration. The fuel plate temperature rise at 170 MW was within ± 7% (at all monitored points) of the values predicted by the MACABRE computer code[1]. This is well within the deviation attributable to the variation in local fuel content indicating that the systematic bias and random variation assigned to the film heat transfer coefficient prediction are not required.

(5) High Power Flow Instability Test

This test attempted to determine the power level and mechanism associated with the burnout phenomena at a high Reynolds' Number. With the special fuel element in the reactor core, the flow was reduced to the value obtained at 21.5 psi core differential (about 20,000 gpm). With 276 psig inlet pressure, the power was increased in steps to 170 MW with resulting stable operation. The test was terminated with no observed flow instability.

(6) Cladding Corrosion Test

With the experimental fuel element in the hottest reactor core position, F-12, the reactor was operated for 186 hours at the equivalent of 170 MW (33 and 40 MW in the center and southeast lobes, respectively). Initial temperatures agreed with the predicted differentials to within +5 to -9.5%. The time-dependent increase in temperature, however, did not agree with the value predicted from the Griess[2]correlation. The measured temperature increase was much smaller (one-half or less) than the predicted increase. Recovery from a scram at the termination of the test produced temperatures indicating that the oxide film was stable and did not slough as a result of the thermal shock.

Posttest data analysis, including disassembly and measurement of oxide films, is incomplete. Preliminary analysis of samples of the corrosion product, however, indicate that boehmite [$\alpha Al_2O(OH)_3$] was the only hydrated Al_2O_3 species present. A topical report, covering the experimental results in depth, will be issued as soon as analysis is complete.

1.2 ATR Production Element Testing (M. L. Griebenow, J. A. Hendricks)

To fulfill operational needs for Cores II and III and the initial ATR reactor operating cycles, 149 enriched fuel elements were proof-tested to 120% nominal flow at 177°C. Forty-four of these were zone-loaded elements of the 7-F prescription required for the power demonstration cores (Cores II and III). In addition, the qualification and initial production elements, fabricated by National Lead Corporation, were proof-tested, and two dummy (depleted uranium) elements, fabricated by this vendor, were subjected to a deliberate destruction test. In the destruction test, the test conditions in the two dummy fuel elements were incrementally increased to the design limit of the hydraulic loop (260°C and 1300 gpm). At these conditions, one element exhibited catastrophic failure and one was unaffected.

1.3 ATR Development Element Testing (M. L. Griebenow, J. A. Hendricks)

A series of tests were conducted to modify the side plate venting arrangement for both improved flow rates in Channel 20 and reduced lateral pressure gradients (across the fuel plates). As a result of these tests, 300 to 400 fuel elements will be supplied from National Lead Corporation with one less set of side plate vents.

Additional hydraulic tests were conducted to determine the cause of the observed flow reduction in Channel 20[3]. Several possible contributions, including the end castings, have been eliminated. Tests, now underway, indicate that the flow rate in Channel 20 behaves differently when the channel is in direct communication with the channels between the side plates and with Channel 1 than it does when it is isolated from these channels. When Channel 20 is not isolated by the side plate rails contacting either the beryllium or the neck shim housing, it appears to behave as a portion of an eccentric annulus; in this case, when Channel 20 is thicker than the channel separating the

side plates, the coolant flow rate through Channel 20 is less than the value calculated for its dimensions alone. This phenomenon has been observed and reported in the literature for eccentric annuli. When Channel 20 is isolated, however, all available data indicate that it behaves as a normal rectangular channel -- provided the two bounding surfaces are parallel. When the radius of curvature of plate 19 and the beryllium (or neck shim housing) differ, there may be sizable azimuthal velocity variation within Channel 20. The velocity variation does not develop above the top set of side plate vents; in this region, the fluid acceleration terms are dominant. Below the axial center line (in the hot region), however, the frictional energy loss components dominate and large velocity variations have been measured. These tests are continuing in an effort to justify neglecting the reported Channel 20 flow bias [1] in an analysis based on a minimum (isolated) Channel 20, and to demonstrate that the coolant velocity increases monotonically as the channel is enlarged and begins to communicate directly with the side plate channels (ie, to show that there is no minimum flow as the configuration changes from an isolated channel to a section of an eccentric annulus).

1.4 ATR Operational Analysis (G. N. Fillmore, M. L. Griebenow)

The safety system setpoint, fuel burnup, and thermal stress analysis required by the ATR Full Power Operating Limits has been performed for Core II (balanced power demonstration), and 250 MW operation has been approved. The analysis indicates that the core may be safely operated to 8750 MWd, and approvals have been requested for this extended cycle operation.

The required analysis for Core III (40-50-60 MW unbalanced operation) is in progress as is the analysis of the limiting power for balanced operation with a full core loading of standard fuel elements (MK IV-VI).

2. ETR SURVEILLANCE

(G. N. Fillmore, J. A. Hendricks)

Postcycle coolant channel measurements were taken in the four hottest ETR fuel elements out of each high power ETR cycle. These measurements have indicated that there has been no significant plate deformations occurring in cycles lasting up to 6000 MWd.

3. MTR PHOENIX CORE

(M. L. Griebenow)

Section personnel performed the initial thermal-hydraulic operational and safety system analysis for the Phoenix core (reported in IN-1209) and scheduled the required power distribution measurements for the MTR Phoenix critical run. As soon as the critical measurements are available, the analysis will be repeated using the correct three-dimensional power distributions to establish the core operating power.

Because the Phoenix cycle will last much longer than any previous cycle, no corrosion data from the MTR primary system is available from which to accurately predict fuel plate operating temperatures and resulting thermal stresses. Therefore, it is planned to measure the retained corrosion product and to verify the lack of fuel plate distortion at discrete time intervals throughout the cycle.

4. REFERENCES

1. M. L. Griebenow and K. D. Richert, MACABRE II, IN-1107 (September 1967).

2. J. C. Griess, H. C. Savage, J. L. English, Effect of Heat Flux on the Corrosion of Aluminum by Water. Part IV. Tests Relative to the Advanced Test Reactor and Correlation with Previous Results, ORNL-3541 (February 1964).

3. M. L. Griebenow, Isothermal Hydraulic Measurements in Fuel Elements in ATR Core, IN-1158 (September 1968).

4. R. S. Marsden, R. L. Curtis, D. W. Knight, Safety Analysis Report for the MTR Phoenix Fuel Experiment, IN-1209 (March 1969).

IV. CRITICAL FACILITIES

1. COUPLED FAST REACTIVITY MEASUREMENT FACILITY

(D. W. Knight)

The Coupled Fast Reactivity Measurement Facility (CFRMF) has been installed in the Advanced Reactivity Measurement Facility-II [1] (ARMF-II). The CFRMF was designed to be used with ARMF-II to measure fast neutron integral cross sections. These integral cross sections for many fuels and structural materials are important to fast reactor programs.

A cutaway view of the CFRMF positioned in ARMF-II is shown in Figure IV-1. The central core of the CFRMF is a 5.7-inch-square, 24-inch-long

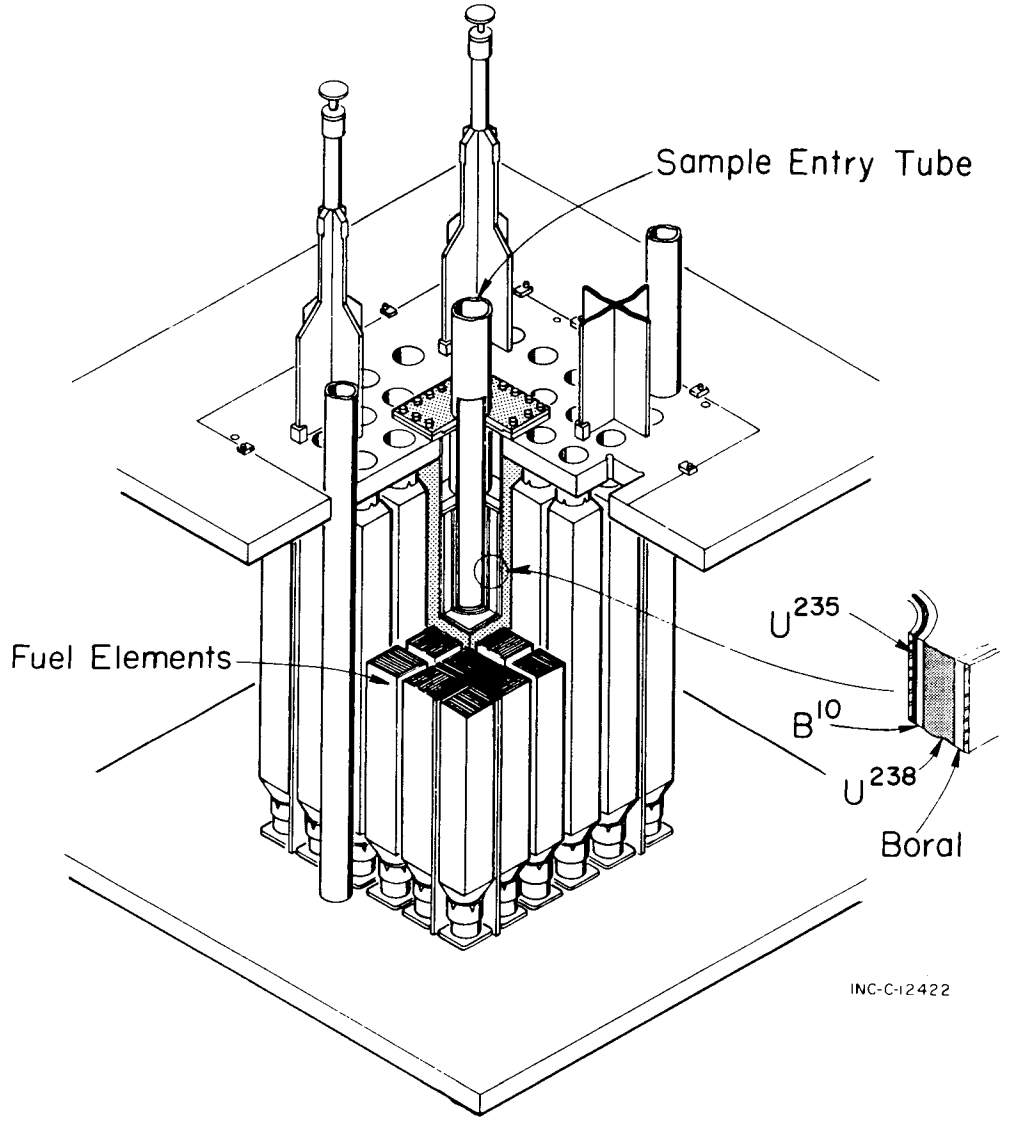

Fig. IV-1 Cutaway view of the Coupled Fast Reactivity Measurement Facility.

block of depleted uranium (0.3% U-235). Passing vertically through the center of the uranium block is a 2.1-inch-diameter hole. The hole is used to position experimental samples and U-235 and B-10 filters. These filters are used to adjust the real and adjoint neutron flux in the experimental region. The outside of the uranium block is surrounded by boral plate. The entire unit is sealed in a type 304 stainless steel container. Completely assembled, the CFRMF weighs approximately 600 pounds.

As shown in Figure IV-1, the CFRMF is positioned in the center region of ARMF-II. Regular ARMF-II fuel elements are positioned around the unit forming a critical assembly with a thermally driven fast-zone core (the CFRMF). When an experimental sample is placed in the experiment region, only the reactivity response to fast neutrons is measured, since the thermal and near-thermal neutrons have been largely eliminated from the CFRMF. The neutron flux per unit lethargy, based on measurements taken using proton recoil techniques, peaks at 325 keV. Reactivity measurements are made in the usual manner using existing ARMF-II electronics [1].

Experimental programs using the CFRMF are under the direction of the Reactor Experiments Section of the Nuclear Technology Branch.

2. REACTOR PHYSICS RESULTS FROM LOW POWER MEASUREMENTS IN THE ADVANCED TEST REACTOR[2]

(N. C. Kaufman, J. L. Durney, J. C. Tappendorf, J. B. Willis)

Power distribution and outer shim calibration data show that the outer shim modifications following the initial Advanced Test Reactor (ATR) startup did not change the previously demonstrated ATR-ATRC (ATR Critical Facility) nuclear correspondence. The outer shim calibration data also indicate that the small difference in excess reactivity, ≈0.3$, between ATR and ATRC is the same as observed previously.

Increasing the reactor coolant temperature caused only slight changes (≈2%) in safety rod and shim worths. Increasing the loop coolant temperatures caused a 9% decrease in the No. 1 neck shim set worth, a 12% increase in outer shim S34 worth, and only slight changes in regulating rod and safety rod worths.

Fast (>1 MeV) neturon flux and gamma heating measurements produced data with the expected axial cosine distributions. Comparison of these data with ATRC data indicates that ATR fast neutron flux and gamma heating (for positions near the fuel) can be predicted from low power ATRC measurements with 5 and 20% uncertainties, respectively.

Noise measurements produced a value of 25.2 $\pm$0.3 Hz for β/Λ, as expected. The power spectral density from zero-power measurements shows prominent resonances resulting from vibration of the in-pile experiment tubes.

3. UNPERTURBED FLUX-TRAP FISSION RATE AS A FUNCTION OF LOBE POWER IN ATRC

(J. C. Tappendorf)

Fission rate data obtained at core midplane for the nine ATRC flux traps show that the unperturbed[a] fission rate per watt of lobe power[b] is not noticeably affected by differences in power division, shims used to obtain the power division, or composition of the adjacent flux traps. Thus, the relative fission rate in an ATR flux trap containing an experiment can be reasonably estimated during operation from lobe power indications.

Table IV-1 shows the average fission rate per watt of power and the percent standard deviation of the data for each flux trap. These data were

TABLE IV-1

AVERAGE FISSION RATE PER WATT OF LOBE POWER AT CORE MIDPLANE IN THE FLUX TRAPS FOR SEVERAL FLUX RUNS

Interior Flux Trap	Fissions/Watt g-sec	% Standard Deviation of Data (1σ)	Exterior Flux Trap	Fissions/Watt g-sec	% Standard Deviation of Data (1σ)
NW	0.247×10^8	2.8	N	0.0839×10^8	2.5
NE	0.392×10^8	2.0	S	0.0833×10^8	2.6
C	0.243×10^8	1.5	W	0.127×10^8	3.1
SW	0.251×10^8	3.6	E	0.133×10^8	4.5
SE	0.247×10^8	2.4			

obtained from several flux runs which were diverse in power distribution, shim positions, and experiment loading. The percent standard deviations of the data in the nine flux traps are not much different than expected from the precision in these measurements ($1\sigma \approx 3\%$). Thus the fission rate per watt of lobe power for each flux trap appears to be nearly independent of changes in power divisions, shim position, and adjacent experiment loading. Additional experimental results have shown that the fission rate per watt of lobe power is also nearly independent of the addition of a safety rod filler.

Table IV-1 also shows that physically alike flux traps have nearly the same fission rate per watt of lobe power. This is illustrated by comparing

[a] Fission rate measured near the radial center in the water-filled experiment region of a flux trap.

[b] For an interior (eg, NW) flux trap the fission rate at core midplane is divided by its respective lobe power. For an exterior (eg, N) flux trap the fission rate at core midplane is divided by the total of the three adjacent lobe powers.

the results in Table IV-1 for the flux traps in each of three groups of physically alike flux traps: (a) NW, SW, and SE; (b) N and S; and (c) W and E. The C flux trap, which is situated differently in the core than the three groups of flux traps mentioned above, has nearly the same fission rate per watt of lobe power as an interior flux trap with a safety rod. The NE flux trap, which contained a dummy flux trap filler and dummy pressure tube for these flux runs, has a significantly higher fission rate per watt of lobe power than the other interior flux traps. However, in a flux run wherein a standard pressure tube mock-up replaced the dummy pressure tube mock-up, the measured fission rate per watt of lobe power was 0.248×10^8. This value is nearly the same as obtained for the other three interior flux traps, as expected.

4. NEW WEIGHTING FACTORS FOR ATRC POWER COMPUTATIONS

(F. O. German)

A new set of weighting factors has been developed for use in conjunction with fission rate data to compute the power generated in ATR fuel elements. These factors have resulted in a reduction in the complexity of ATRC power calculations.

Power computational methods now available at ATRC include[3]:

(1) Method 1 -- Fission rate profiles are hand integrated to determine the average fission rate of a fuel plate. The average fission rate per plate is converted to the average power generated by each plate. The total power generated by a fuel element is then determined by summing the plate-averaged powers. This method is considered to be superior to other methods, but is highly time consuming.

(2) Method 2 -- A predetermined set of weighting factors is used to adjust measured point fission rate values to the average value in fuel regions about each of 17 UAl fission rate monitor wires placed at the horizontal midplane of a fuel element.

Method 2 is most commonly used because of its adaptability to digital computer techniques and because only 17 monitor wires are required, as opposed to 23 for Method 1.

New weighting factors for use in Method 2 were developed from data obtained in a special flux run. The flux run was made in the ATRC with a nominally 40-50-60 power division to obtain typical flux gradients within the fuel elements. Each new weighting factor was constructed from components which adjusted the fission rate value at a monitor position for the radial and azimuthal flux gradients and the fuel content within an assigned area about the monitor position. These new weighting factors were further constrained to be symmetrical about the radial bisector of the fuel element. This constraint was used because the areas assigned in constructing the factors are mirror images of one another about the bisector. This constraint reduces the previous

set of weighting factors (10 subsets corresponding to 10 fuel element positions, each composed of 17 weighting factors) to a single set of 17 weighting factors. This single set can be used to compute the power generated in a fuel element independent of fuel element position or reactor power division.

Fuel element powers calculated using the new Method 2 weighting factors are within ±2% of the values calculated by Method 1. Furthermore, the total power generated by 10 fuel elements, as computed with the new weighting factors, showed an average deviation of only +0.07% from that calculated using the Method 1 procedure. The new weighting factors are shown in Figure IV-2.

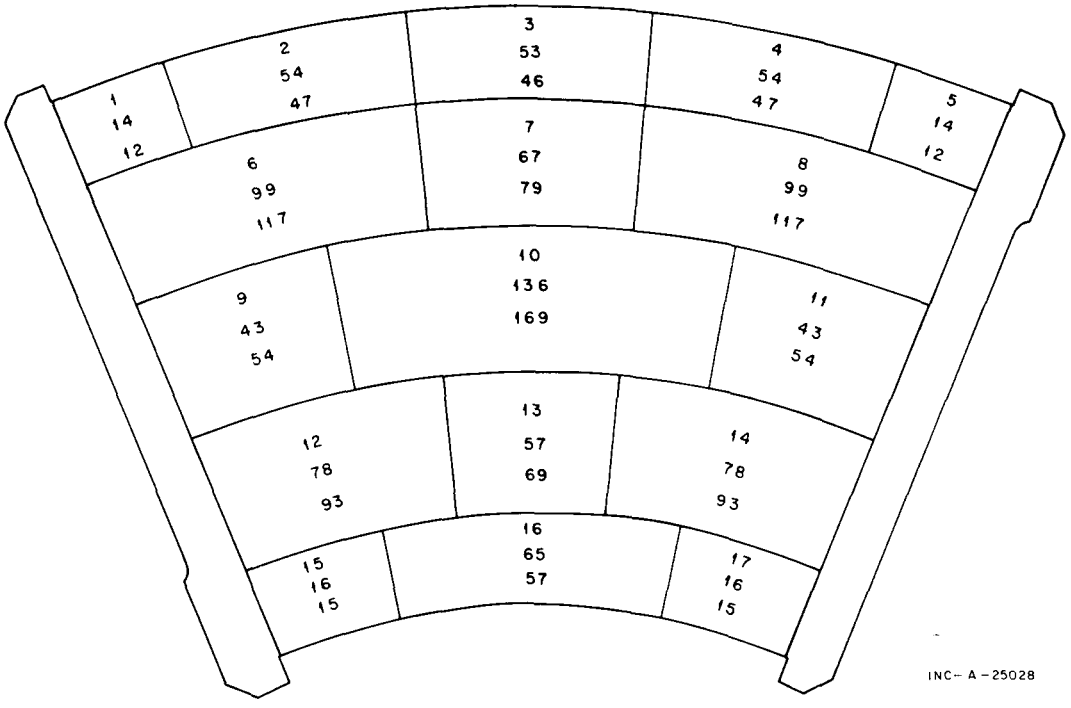

Fig. IV-2 New Method 2 weighting factors. The top number represents the monitoring area, the middle and bottom numbers the factors for the 975- and 1075-g fuel elements, respectively.

A second set of weighting factors was constructed for use with 1075-g, zone-loaded ATR fuel elements (designated "7F"). These factors are also shown in Figure IV-2 in their respective flux monitor areas.

5. ETR FLUX STABILIZATION PROGRAM

(R. A. Jensen, J. E. Brasier, A. L. Bowman)

The Engineering Testing Reactor (ETR) is operated for the purpose of irradiating material samples at a high neutron flux. To attain this high flux, some samples must be located within the reactor core rather than in the reflector. These in-core samples are subject to considerable flux variations

due to (a) the movement of other experiments, (b) the movement of control rods, (c) fuel and boron burnup, and (d) variations in the power level.

The ETR Flux Stabilization Program was started in 1965 to stabilize the neutron flux distribution in the ETR. This program is divided into two main categories: inter- and intracycle. The intercycle flux stabilization program is directed at maintaining the initial power distributions of all cycles within certain limits, whereas the intracycle program is directed at maintaining a constant neturon flux distribution throughout each cycle.

5.1 Intercycle Flux Stabilization

5.11 Cycle Mock-Ups. The primary vehicle for intercycle flux stabilization is the cycle mock-up which is carried out in the ETR Critical Facility (ETRC) preceding each ETR cycle. Cycle mock-ups are conducted to arrange the ETR fuel and experiment loadings such that the neutron flux distribution is as close as possible to predetermined power distribution goals without sacrificing reactor safety. Parameters to be reconciled during the mock-ups include peak power densities, reactivity worths of control rods, control rod positions, shutdown reactivity, and the amount of burnable poison in the core. Cycle mock-up data are obtained at five vertical levels in every fuel element in the core. The experiment neutron source (ENS) number is a measure of the neutrons available to each experiment facility. The ENS number has been defined [4] in terms of the power generated in the surrounding fuel elements.

Beginning with Cycle 79 and continuing through Cycle 90, the objective of the Flux Stabilization Program was to match the power distribution of each cycle to a standard power distribution (SPD-2/66 or SPD-2/66A) [5, 6, 7]. However, the nominal fuel loading of each ETR fuel element was changed beginning with Cycle 91, from 400 to 500 g U-235. It then became necessary to change the core configuration and establish a new SPD.

For ETR Cycles 91 through 106, the cycle mock-up goals are to provide a flux distribution where all ENS numbers are within $\pm 10\%$ of their counterpart numbers for the standard power distribution (SPD-7/67A) and for the average of the two previous cycle mock-ups. In each mock-up, flux data are obtained at core midplane, ± 7 and 14 inches for each of the 51 fuel elements. From these, 135 ENS numbers are calculated in 27 experimental positions. Comparison of the mock-up data to the previous cycle average guards against large short-term changes in the neutron flux distribution, while comparison to the SPD-7/67A goal guards against long-term shifting trends in the flux distribution.

The fraction of ENS values differing by more than $\pm 10\%$ from SPD-7/67A and the average percent change of the ENS numbers relative to the previous two-cycle average for Cycles 91 to 103 are shown in Figure IV-3. Although reducing the latter value was not a specific mock-up goal, it provides a good measure of the continuity of the flux distribution.

At the time SPD-7/67A was established, the position of the ETR regulating rod was mocked up at its upper limit (36 inches withdrawn) in ETRC, but beginning with Cycle 94, the ETRC mock-up duplicated the ETR regulating rod position in its normal operating range (about 30 inches withdrawn). This

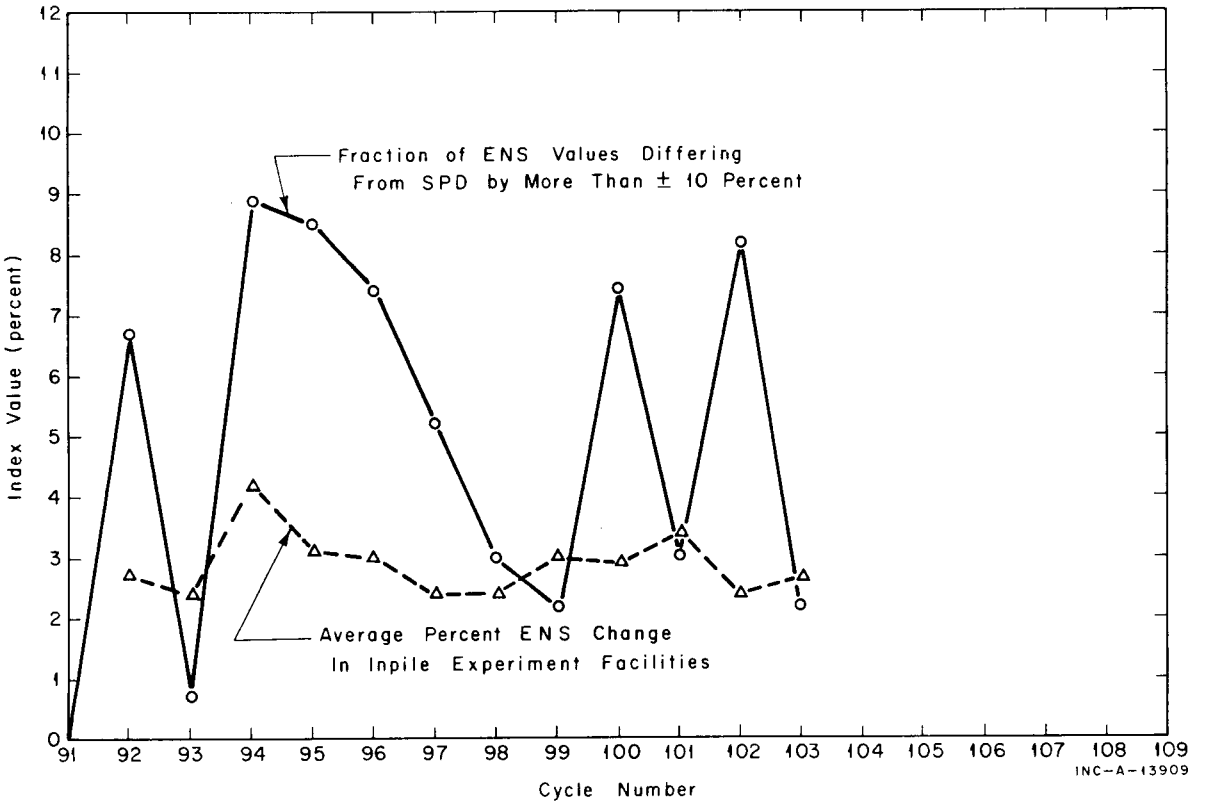

Fig. IV-3 ETR intercycle flux variation indices.

change represents an improvement in the accuracy of the mock-up rather than an actual change in the power distribution of the ETR. However, correct positioning of the regulating rod beginning in Cycle 94 caused some numbers at the ±14 inch level to be greater than ±10% relative to the mock-up goals.

A breakdown on ENS numbers differing by more than ±10% from mock-up goals for Cycles 94 to 103 is presented in Table IV-2. It is significant that since Cycle 95 no ENS numbers have differed by more than ±10% from both SPD-7/67A and the two-cycle average.

5.12 Fuel Loadings for the ETR. Prior to every new core loading at the Engineering Test Reactor, the experiments as well as the fuel arrangement are mocked up in the ETR Critical Facility. Therefore, the selection of ETR Mark V fuel assemblies for each ETRC mock-up core loading is an important factor in determining reactor physics characteristics.

Computer (360/75) programs SØRT and CØRLØD are used in the process of selecting ETR cores. Program SØRT is used to maintain an up-to-date inventory of all ETR reactor fuel released by the Fuel Inspection Group. The program sorts the fuel inventory according to serial number, boron content, U-235 content, and fabricator, in addition to indicating any restrictions that may be applied to the fuel assembly. From this inventory and the known ETRC reactivity, fission rate distribution, and power density data for the

TABLE IV-2

NUMBER OF ENS VALUES >10% FROM GOALS

Cycle Number	ENS Values >10% From SPD-7/67A Due to Regulating Rod Original ETRC Mock-up Data	ENS Values >10% From Previous Two-Cycle Average Due to Regulating Rod	ENS Values >10% From SPD-7/67A Not Caused by Regulating Rod	ENS Values >10% From Previous Two-Cycle Average Not Caused by Regulating Rod
94	1	1	11	6
95A	3	3	9	4
95B	3	2	8	3
96	3	1	7	0
97	4	0	3	0
98	4	0	0	0
99	3	0	0	5
100	1	0	9	0
101	4	0	0	1
102	4	0	7	0
103	1	0	2	0

previous cycle mock-up, fuel elements and sections are selected for the forthcoming ETRC mock-up core loading which will most nearly duplicate the reactor physics characteristics of the previous ETRC cycle mock-up. Program CØRLØD is then used to print out the selected fuel element or serial number, U-235 content, and boron content in a standard core map form. In addition, CØRLØD calculates (a) the total grams of U-235 and boron in the present core loading, (b) the U-235 and boron differences from the previous core loading, and (c) the total grams of U-235 and boron for different types of fuel assemblies in the core loading. These numbers are used to predict the net change in reactivity and critical rod positions between core loadings.

Considerable attention is given to adjusting thermal neutron flux distributions within a core by changing the boron distribution. The data shown in Figure IV-4 illustrate the effect of moving 1.73 g boron from core position E13 to position F5 during the ETRC mock-up of ETR Cycle 100 at xenon equilibrium conditions. In this case, the percent core power in position E13 changed by 15%, with a general increase of flux in the southwest quadrant of the core and a decrease of flux in the northwest quadrant. The effectiveness of using boron to control the thermal neturon flux distribution is readily apparent in this example.

Since it is obvious that fuel-element boron content is an important part of the ETR flux stabilization program, it is likewise obvious that boron content in each fuel element must be carefully controlled. Each new ETR fuel element is nondestructively boron assayed at the ETRC to determine whether the fabricator has met Idaho Nuclear boron content specifications. Boron contents are determined by establishing a boron content versus reactivity curve using fuel assemblies with known boron contents as standards and comparing the fuel elements with unknown boron contents against that curve. A 360/J75 computer program designated as NLLS (Non-Linear-Least Squares-Fitting) is used to plot and calculate parameters from the linear boron calibration curve. Another 360/J75 program called BØRØN uses the NLLS parameters in a cubic equation to compute the effective boron of any fuel element from an input of critical ship-rod positions.

The measured effective boron contents of several hundred ETR 500-g UAl_x and boron foil type fuel elements are shown in Figure IV-5 for different fuel fabricators. As indicated, ETR fuel elements fabricated using the UAl_x powder metallurgy technique show the best fabricator control. ETR fuel elements fabricated using the UAl alloy/B_4C-Al foil technique indicate fair control by the fabricator over the built-in natural boron, except for one subcontract (S-294).

Boron assaying techniques are continually being improved to provide the best possible measured effective boron values, thus enhancing the ETR flux stabilization programs.

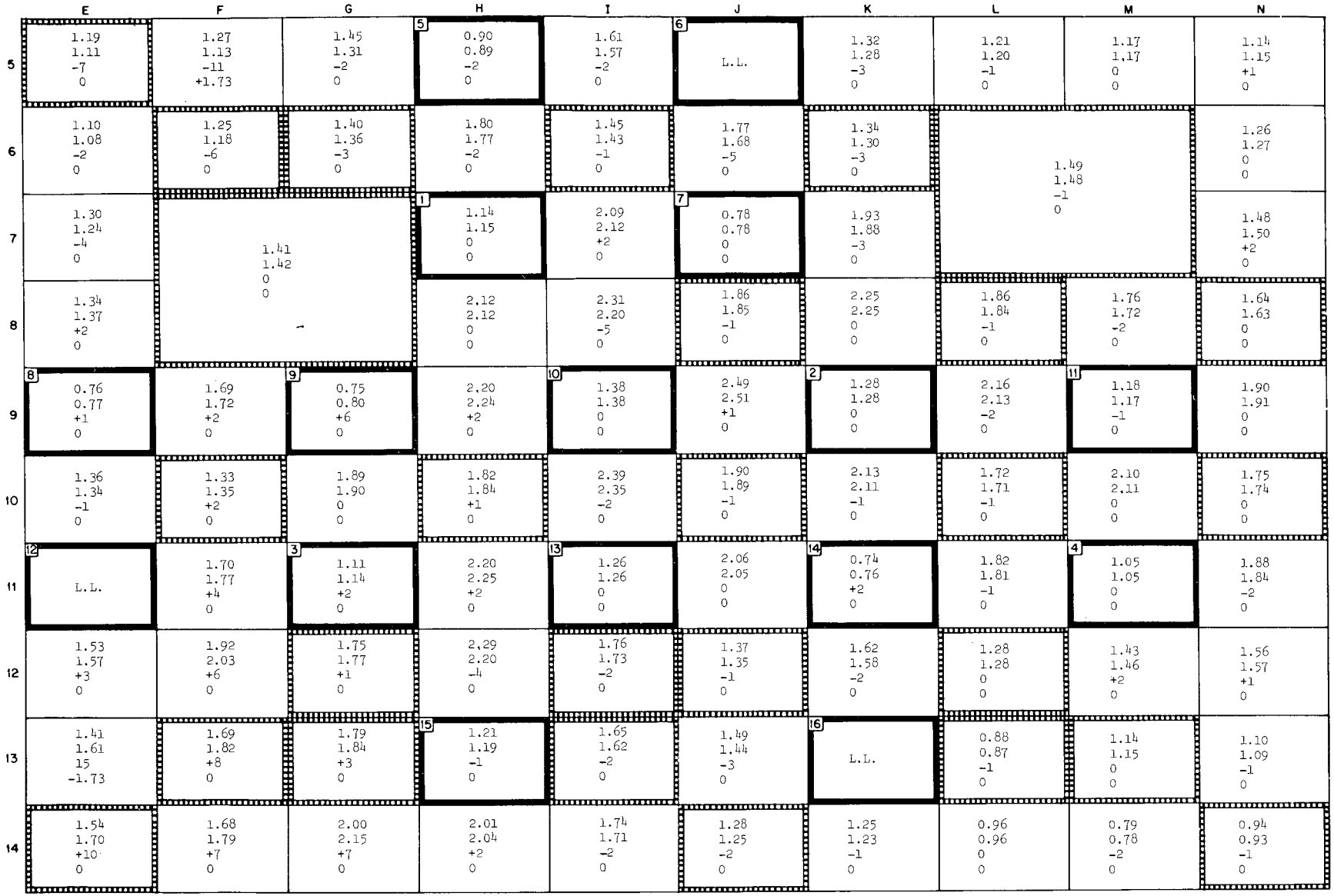

Fig. IV-4 Effects of moving 1.73 g boron from core position E13 to position F5. The first and second numbers represent the percent core power or average experiment neutron source value in Cycle 100-3 and 100-4, respectively. The third number represents the percent change of the second number from the first, while the fourth number represents the change in boron (grams) from Cycle 100-3 to 100-4.

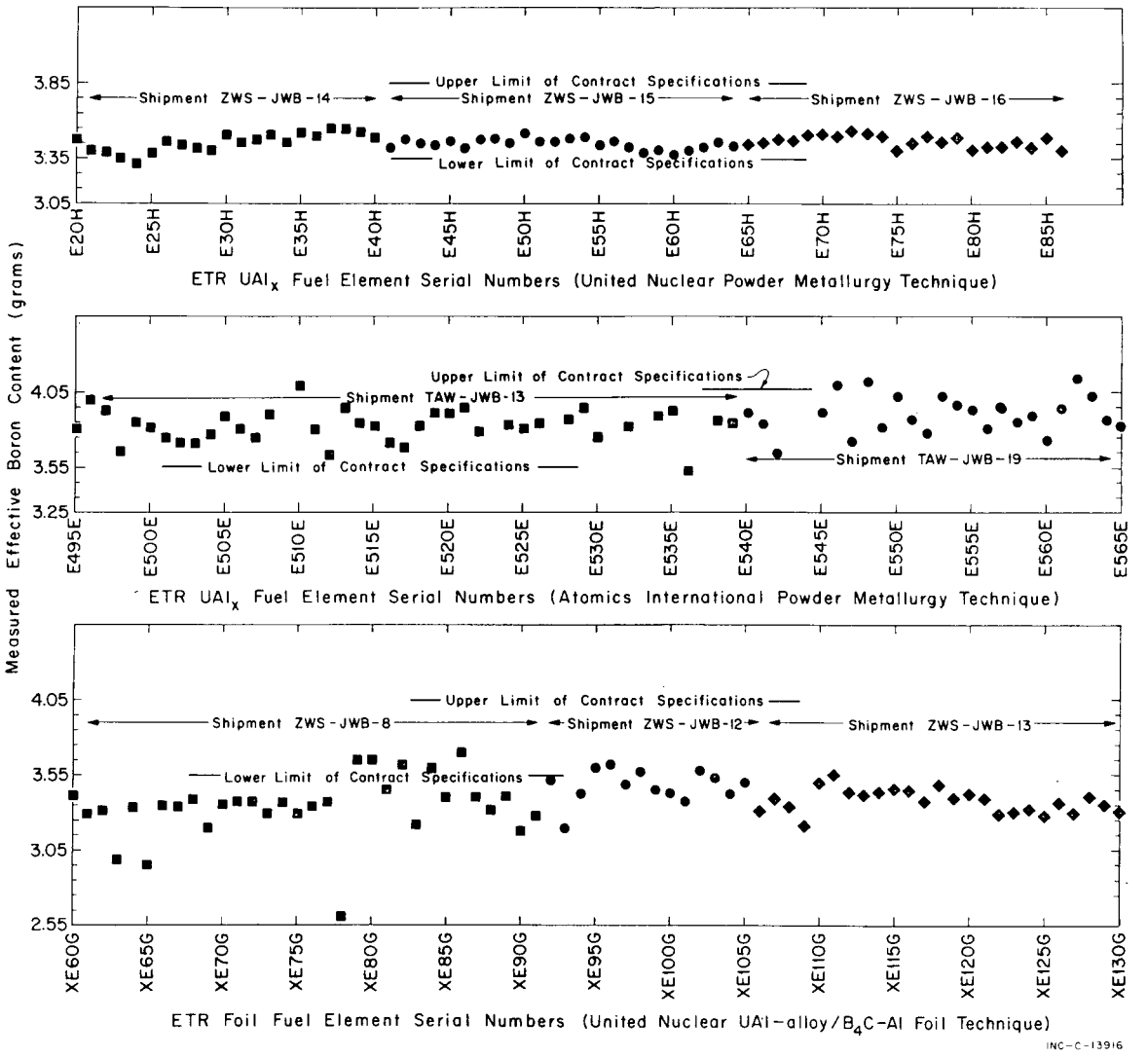

Fig. IV-5 Measured effective boron contents of ETR UAl_x and boron foil type fuel elements.

5.2 Intracycle Flux Stabilization

Intracycle flux stabilization in ETR has become increasingly important as core life has been extended. To evaluate the degree of stabilization, a flux monitoring system using self-powered neutron detectors (SPNDs) has been installed in the ETR core and reflector. The first SPND detector became operational in Cycle 77; there are now 42 operable SPND detectors in and around the ETR core. The bulk of these did not begin operating until Cycle 96.

These detectors show that intracycle flux variations are generally $\pm 10\%$ during the first 4000 MWd of core operation. After this time, variations may increase rapidly, depending partly upon the proximity of the shim rods to the SPNDs. In Cycle 91, the transition from 400- to 500-g fuel elements greatly impoved flux stability [8]. Optimum positioning of control rods at the beginning of the cycle, for minimum rod movement during the course of the cycle, has further reduced intracycle flux variations. Recent data also show that a carefully selected rod program or possibly redesigning of control rods can contribute signficantly to the decrease in variations.

6. REFERENCES

1. E. E. Burdick, E. Fast, and D. W. Knight, The Advanced Reactivity Measurement Facilities -- A Description and Performance Evaluation, IDO-17005 (October 1964).

2. N. C. Kaufman, J. L. Durney, J. C. Tappendorf, and J. B. Willis, Reactor Physics Results from Low-Power Measurements in the Advanced Test Reactor, IN-1260 (February 1969).

3. J. L. Durney and N. C. Kaufman, Calculating Reactor Power from Activation Techniques as Applied to an Unusual Fuel Geometry (ATRC), IN-1047 (January 1967).

4. E. H. Smith et al, ETR Operations Branch Progress Report for Cycle No. 91 -- July 24, 1967 - October 1, 1967, IN-1140 (November 1967).

5. E. H. Smith et al, ETR Operations Branch Progress Report for Cycle No. 78 -- January 16, 1966 - February 27, 1966, IDO-17171 (April 1966).

6. E. H. Smith et al, ETR Operations Branch Progress Report for Cycle No. 81 -- May 22, 1966 - July 4, 1966, IDO-17201 (August 1966).

7. E. D. Covington (ed.), Reactor Engineering Branch Annual Report -- FY-1968, IN-1228 (February 1969).

8. D. R. deBoisblanc, W. C. Francis, and R. G. Fluharty, Nuclear Technology Branches Quarterly Report, IN-1117 (September 1967).

V. REACTOR TRAINING

1. REACTOR SIMULATORS

(G. E. Morris, G. Ostheller)

The on-site training of reactor engineers is accomplished in a 10-week training session of lectures, problems, examinations, laboratories, and tours conducted by the Reactor Training School. The lectures include physics, reactor statics and kinetics, reactor control, reactor safety, metallurgy, instrumentation, reactor engineering, and health and safety. The tours and laboratory work are designed to give the operator an opportunity to become familiar with the variety of equipment related to the test reactors. Training in abnormal operating conditions is not permitted on the test reactors because of possible hazards to the reactor, experiments, and personnel. To handle unusual and abnormal operating conditions safely and efficiently reactor engineers are now being trained on reactor simulators. Design of the ATR simulator console and electronics began in July 1967, the assembly started in January 1968, and was completed in April 1968.

The ATR simulator console duplicates the appearance and relay logic of the ATR console with the exceptions of the digital computer inputs and safety redundancies. The control rods are simulated with a motor-driven potentiometer of special manufacture to generate the rod reactivity function. The neck shims and outer cylinder drives have digital counters geared with the potentiometer to generate the digital readout displays. The safety rods and servo regulating rods drive the dials direct. The motor-operated-rheostat system consists of two ganged potentiometers driven by a slo-syn pulse motor. One potentiometer is a two-decade logarithmic function, and the second is a linear potentiometer for the meter readout.

The computer used in the reactor simulation is a partially expanded hybrid computer. At present, there is no digital capability, and the analog section has 85% of full capacity. The computer has a removable patchboard and servoset potentiometers thus enabling a complete change of program in less than five minutes if there is no changing of diode function generators.

The computer program used for the simulation can be divided into five separate subgroups: (a) reactor kinetics using logarithmic model, three delayed neutron groups, (b) reactivity summation and power shift computation, (c) xenon-iodine poisoning, (d) heat transfer using open-loop constant-input temperature equations, and (e) outputs to instrumentation and instructor's console.

In August 1968, the new simulator laboratory building was completed and construction begun on ETR and MTR simulators. Training continued on the ATR simulator until December, at which time it was disassembled, moved to the new building, and reassembled. As of July 1, 1969, the ETR simulator was 90% completed and the MTR 75% completed.

VI. FUEL PROJECT ENGINEERING OFFICE

(K. C. Sumpter, J. O. Dittmer)

During FY-1969, a new group, the Fuel Project Engineering Office, was added to the Reactor Engineering Branch. The function of this office is to provide technical assistance in the administration of fuel procurement for the test reactors operated by Idaho Nuclear. This function is accomplished by providing the office with broad flexibility within Idaho Nuclear, by having frequent contact with suppliers (vendors) of nuclear fuel, by full awareness of the processes and current problems of the vendors, and by membership on the Fuel Engineering Review Board and the Fuel Design Review Board of Idaho Nuclear.

The functional Procurement Organization within Idaho Nuclear is depicted in Figure VI-1.

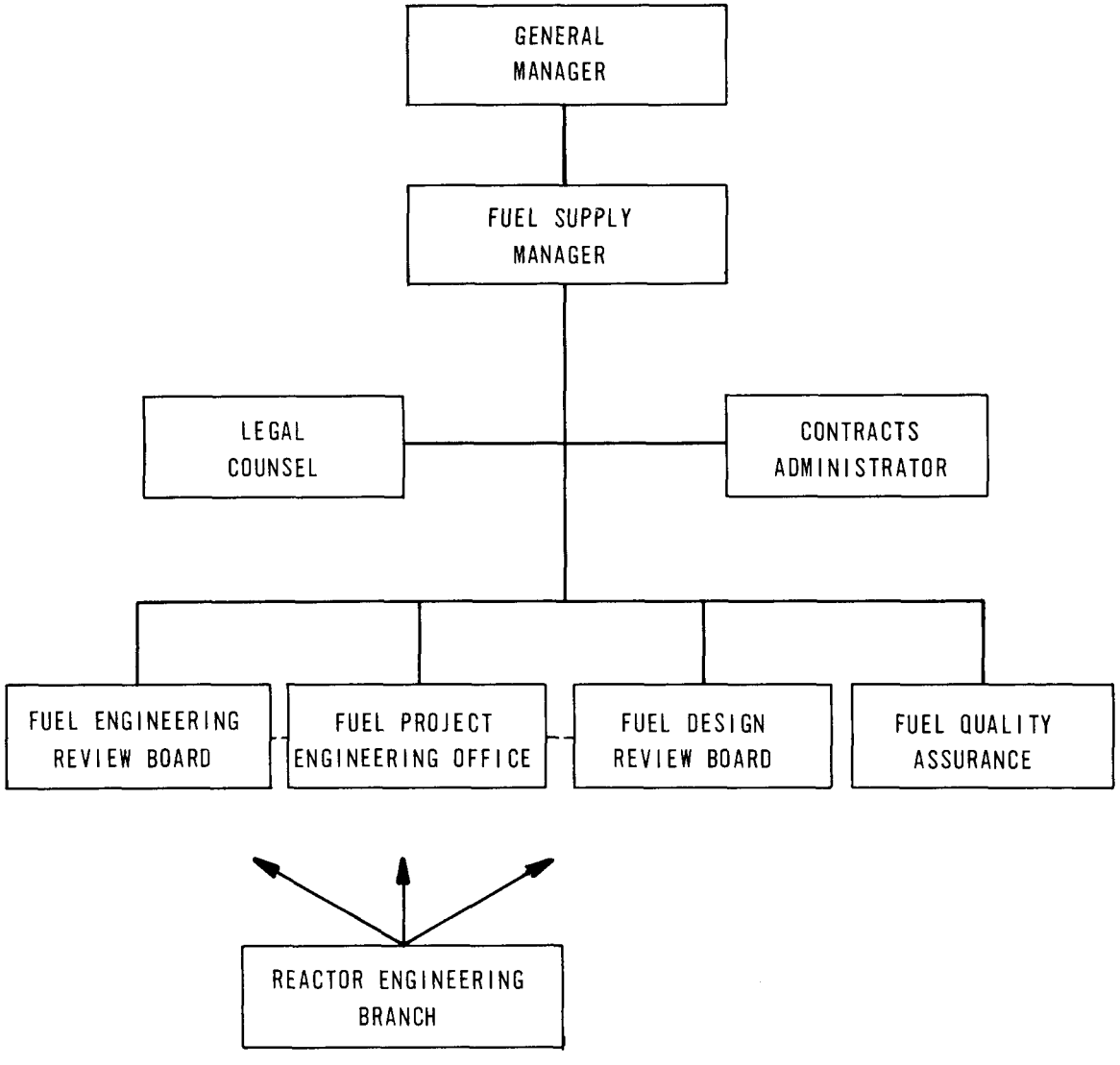

Fig. VI-1 Functional fuel procurement organization within Idaho Nuclear Corporation.

1. VENDOR STATUS

In FY-1969, fuel elements for the three test reactors (ATR, ETR, and MTR) were being fabricated by three vendors. Atomics International (subcontract S-296 for 100 zone-loaded ATR elements) is in the process of completing its contract. The entire contract has gone smoothly; fuel element deliveries have been ahead of schedule. United Nuclear Corporation (subcontract S-287 for 500 standard ETR elements, subcontract S-294 for 200 boron foil ETR elements, and subcontract S-295 for 150 standard MTR elements) has progressed well on all three contracts and fuel element deliveries are ahead of schedule. National Lead Company (subcontract S-297 for 40 standard MTR elements, subcontract C-285 for 700 standard ATR elements, and 50 7-F ATR elements) has completed the MTR contract but is just beginning production on the ATR contracts.

A special plutonium fuel core (designated Phoenix) for the MTR has been fabricated by Pacific Northwest Laboratories. The fuel elements and shim rods were being inspected at the end of the fiscal year.

ORGANIZATION CHART

IDAHO NUCLEAR CORPORATION

IDAHO FALLS, IDAHO

REACTOR ENGINEERING BRANCH

June 30, 1969

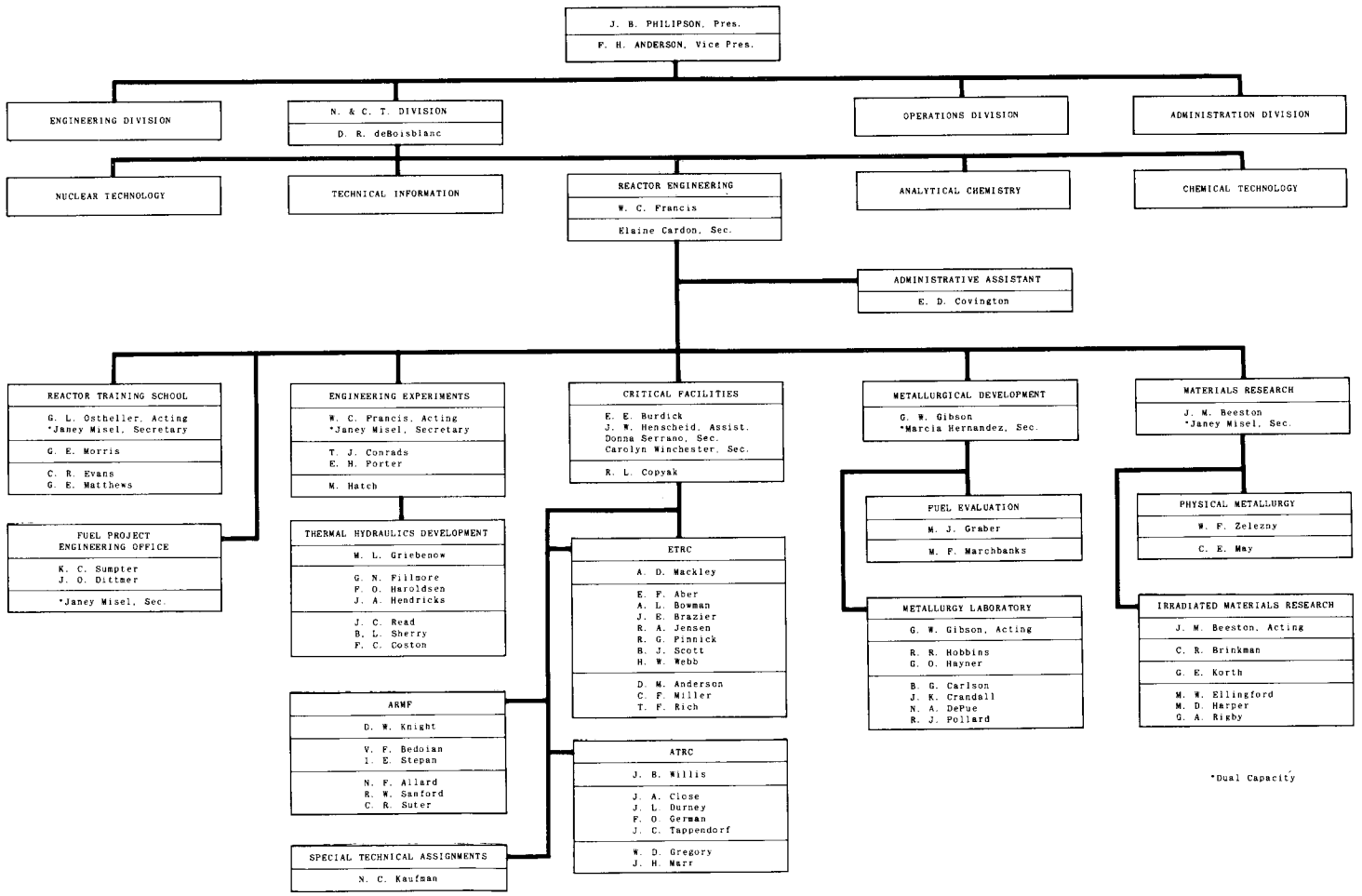

*Dual Capacity